

DIGITAL ACCESS TO SCHOLARSHIP AT HARVARD
DASH.HARVARD.EDU

HARVARD LIBRARY


Electronic and Nanophotonic Integration of a Quantum Network Node in Diamond

Citation

Machielse, Bartholomeus Johannes. 2021. Electronic and Nanophotonic Integration of a Quantum Network Node in Diamond. Doctoral dissertation, Harvard University Graduate School of Arts and Sciences.

Link

https://nrs.harvard.edu/URN-3:HUL.INSTREPOS:37368318

Terms of use

This article was downloaded from Harvard University's DASH repository, and is made available under the terms and conditions applicable to Other Posted Material (LAA), as set forth at
https://harvardwiki.atlassian.net/wiki/external/NGY5NDE4ZjgzNTc5NDQzMGIzZWZhMGFlOWI2M2EwYTg

Accessibility

https://accessibility.huit.harvard.edu/digital-accessibility-policy

Share Your Story

The Harvard community has made this article openly available.
Please share how this access benefits you. Submit a story

HARVARD UNIVERSITY
Graduate School of Arts and Sciences



DISSERTATION ACCEPTANCE CERTIFICATE

The undersigned, appointed by the

Department of Physics

have examined a dissertation entitled

Electronic and Nanophotonic Integration of a Quantum Network Node in Diamond

presented by Bartholomeus J. Machielse

candidate for the degree of Doctor of Philosophy and hereby certify that it is worthy of acceptance.

Signature _____

Typed name: Professor Mikhail Lukin, Chair

Signature _____

Typed name: Professor Marko Lončar

Signature _____

Typed name: Professor Amir Yacoby

Date: March 25, 2021

Electronic and Nanophotonic Integration of a Quantum Network Node in Diamond

A DISSERTATION PRESENTED
BY
BARTHOLOMEUS J. MACHIELSE
TO
THE DEPARTMENT OF PHYSICS

IN PARTIAL FULFILLMENT OF THE REQUIREMENTS
FOR THE DEGREE OF
DOCTOR OF PHILOSOPHY
IN THE SUBJECT OF
PHYSICS

HARVARD UNIVERSITY
CAMBRIDGE, MASSACHUSETTS
MARCH 2021

©2021 – Bartholomeus J. Machielse
all rights reserved.

Dissertation advisor: Professor Mikhail Lukin Bartholomeus J. Machielse

Electronic and Nanophotonic Integration of a Quantum Network Node in Diamond

Abstract

Developing technologies for distributing entanglement over long distances, and employing this technology to create quantum communication networks, has been a standing goal of the quantum optics community for almost two decades. Such networks could be used for secure communication enabled by quantum key distribution (QKD), enhancement of quantum sensors, and even the creation of networked quantum computers. We present a platform, based on the negatively charged Silicon Vacancy (SiV) in diamond, capable of correcting for the photon loss that currently limits the size of such networks. Furthermore, we lay the groundwork for its use for scalable implementation of the full quantum repeater protocol, the missing ingredient for the deployment of large quantum networks. First, we demonstrate improved diamond nanofabrication techniques that enable the creation of an integrated, cooperativity 100 spin-photon interface. We further discuss the techniques used to integrate this platform with microwave coplanar waveguides (CPWs) that enable coherent control of the SiV spin state. Next, we demonstrate the integration of diamond nanophotonic technology with nanomechanical strain control, enabling the reduction of variations between, and fluctuations of, diamond color center optical and spin properties. These techniques are used to enable quantum interference between two initially distinguishable quantum emitters. To further demonstrate the utility

of this platform, we employ coherent spin control and our platform's high cooperativity spin-photon interface to create an integrated quantum network node capable of high fidelity, coherent photon storage and the formation of multiqubit quantum registers. We discuss the engineering and physics principles relevant to the implementation of such a system, and provide a framework for future improvements to the underlying technology. Finally, we employ the developed techniques to perform Bell state measurements between asynchronously arriving photons. By utilizing this technique we demonstrate enhancement of the quantum communication rate between two parties, thus implementing the key functionality of a single quantum repeater node. This demonstration, combined with the other technical advances presented here, positions the diamond photonics-SiV platform as a leading candidate for the implementation quantum networking technology and provides a path towards large scale deployment of such systems.

Contents

Title . . . i
Copyright . . . ii
Abstract . . . iii
Table of Contents . . . v
Dedication Page . . . vii
Acknowledgments . . . ix

1 Introduction 1
1.1 Quantum Networks . . . 1
1.2 Overview . . . 6

2 Diamond Nanofabrication for Quantum Networks 8
2.1 Diamond as a Host for Quantum Defects . . . 9
2.2 Photonic Crystal Cavities . . . 19
2.3 Diamond Nanofabrication . . . 27
2.4 Practical Considerations for Diamond Fabrication . . . 33
2.5 Nanophotonic Technology Integration . . . 44

3 Quantum Interference of Strain Controlled SiV Color Centers 50
3.1 Introduction . . . 52
3.2 Waveguides With Strain Control . . . 54
3.3 Mitigation of Spectral Diffusion . . . 57
3.4 Observation of Quantum Interference . . . 59
3.5 Strain Tuning in Cavities . . . 63
3.6 Discussion . . . 64
3.7 Device Fabrication . . . 65
3.8 Setup . . . 67
3.9 Feedback Scheme . . . 71
3.10 Emitter model and simulation . . . 72
3.11 Bright State Fidelity Analysis . . . 75
3.12 Conclusion and Next Steps . . . 78

4 Quantum network nodes based on diamond qubits 81
4.1 Introduction . . . 84
4.2 Spin Readout . . . 86

4.3 Microwave Control . . . 88
4.4 Spin-photon Interface . . . 90
4.5 SiV Electron to Nuclear Spin Interface . . . 91
4.6 CNOT gates and Bell State Formation . . . 94
4.7 Limitations of the SiV - ^{13}C Gate . . . 95
4.8 SiV-^{29}Si Gates . . . 95
4.9 Conclusion and Outlook . . . 98

5 An Integrated Nanophotonic Quantum Register in Diamond 99
5.1 Introduction . . . 101
5.2 Nanophotonic device fabrication . . . 103
5.3 Experimental Setup . . . 108
5.4 Optimal strain regimes for SiV spin-photon experiments . . . 111
5.5 Regimes of cavity-QED for SiV spin-photon interfaces . . . 118
5.6 Microwave spin control . . . 123
5.7 Investigating the noise bath of SiVs in nanostructures . . . 127
5.8 Spin-photon entanglement . . . 130
5.9 Control of SiV-^{13}C register . . . 135
5.10 Nanophotonic cavity design . . . 141
5.11 Strain-induced frequency fluctuations . . . 145
5.12 Mitigating spectral diffusion . . . 147
5.13 Model for SiV decoherence . . . 148
5.14 Concurrence and Fidelity calculations . . . 151
5.15 Nuclear initialization and readout . . . 155
5.16 Conclusion . . . 157

6 Experimental Demonstration of Memory Enhanced Quantum Communication 159
6.1 Introduction . . . 161
6.2 Fundamental limit of direct transmission . . . 162
6.3 Efficient nanophotonic quantum node . . . 164
6.4 Asynchronous Bell-state measurements . . . 167
6.5 Benchmarking quantum memory advantage . . . 169
6.6 Outlook . . . 172

7 Conclusion 174

Appendix A Supporting Information for Chapter 6 177
A.1 Characterization of the nanophotonic quantum memory. . . . 178
A.2 Microwave control . . . 178
A.3 Fiber network. . . . 182

A.4 Experimental details of quantum communication experiment. 185
A.5 Optimal parameters for asynchronous Bell state measurements. 187
A.6 Performance of memory-assisted quantum communication. 191

References 211

For Abby.

Acknowledgments

First I thank my thesis advisors, Misha Lukin and Marko Loncar. Having the opportunity to work in not one, but two labs filled with exceptional people doing great science has been a fantastic experience that would not have been possible without their help. Misha's talent and creativity when it comes to proposing new experiments and understanding where things have gone wrong is unmatched. Meanwhile Marko's insight into not only the finer details of photonics and nanofabrication, but also what makes the people in his lab tick have helped me grow as a scientist and a person. I am exceptionally grateful to have been able to work with both of them. Finally, I thank Professor Yacoby for offering his perspective and technical assistance at various points throughout my PhD.

All of the work in this PhD was conducted using devices made in the Center for Nanoscale Systems, and my good fortune to have colleagues working there who are exceptionally knowledgeable, hard working, and friendly has been key to my success. In particular I want to thank JD, Mac Hathaway, Ed Macomber, Yuan Lu, Steve Paolini, and Dave Lafleur, whose technical assistance and interesting conversation were key to the realization of many of the devices presented in this thesis.

Of course, this work was in very large part the result of the exceptional work done by my colleagues in both the Lukin and Loncar groups. From my very first days at Harvard I had the benefit of having great coworkers who were willing to take the time to guide me and teach me critical personal, professional, and scientific skills. First among these are Mike Burek, Young-Ik Sohn, and Haig Atikian, who

taught me many of the foundational skills in nanofabrication that have served me so well over the years. Their sense of humor and fun even in the face of the often frustrating aspects of fabrication taught me to enjoy my work, while their exceptional standards made sure that I learned to do it well. The fab culture still existent in the diamond effort today is a direct result of their strong characters. I also benefited from the deep understanding of physics shared by Ruffin Evans, Alp Sipahigail, Christian Nguyen, Denis Sukachev, and Srujan Meesala. Each of them was the master of a wide range of physics, ranging from the finest details of the workings of the SIV to the most esoteric elements of our measurement setups. Furthermore, the mentorship and guidance I received from Ruffin and Srujan played a key part in getting me through my PhD and allowing me to contribute to this amazing project. Last, but by no means least, I had the immense pleasure of working with Stefan Bogdanovic, one of the most creative and resilient scientists I have ever met. Stefan was my partner in crime working through the difficult final stretch of the strain tuning experiment, and without his continued good humor and hard work it's very possible the experiment would never have seen the light of day. Even though many of these people have left Harvard, I have been fortunate enough to stay in touch with many of them and look forward to our continued friendship.

The current generation of students have taken up the mantel of their more senior peers and I feel very lucky to have been able to work with them. First among these is Cleaven Chia, who has for long periods been my primary (and often only!) collaborator when it came to developing new diamond nanofabrication techniques. Cleaven's genuinely incredible work ethic, overwhelming attention to detail, and willingness to push through exceptional bad luck are inspiring. Without his talents and efforts our understanding of what is possible in diamond would be drastically reduced and many of the

devices presented here would have been inferior. On the Lukin side of the collaboration, I have had the immense fortune of working with Mihir Bhaskar, whose expertise in quantum optics in general and the SiV in particular is amazing. Ralf Riedinger, who joined this project more recently as a post-doc but has emerged as one of its most important members, is a bottomless well of ideas and insights into physics and people. Both Ralf and Mihir are unique in their continued desire not only to learn more about their work, but also to share this knowledge with others. There are few people I could imagine better suited to exploring the frontiers of quantum technology. Meanwhile, David Levonian has stepped into this project and quickly applied his immensely wide skillset to mastering and improving our measurements. I learned a huge amount from him working on projects and managing the lab together during COVID. Amirhassan Shams-Ansari is one of the friendliest, most insightful, and hardest working individuals I have ever met. Amir constantly goes above and beyond when helping people personally and professionally, in a way that is especially uncommon in high pressure environments like Harvard, for which he has earned my deepest respect. My collaborations with Neil Sinclair, Smarak Maity, Linbo Shao, and Jeffrey Holzgrafe have also taught me a great deal, especially with regards to new measurement and fabrication techniques. I look forward to staying in touch with each of these individuals, and am excited to see where they go next!

Of course, my generation of students is being succeeded by an equally talented group who I am sure will lead the SIV effort to a great future. Within the Lukin group, Erik Knall has stepped up to take over the photonic design and fabrication efforts that I was responsible for over the last few years. Erik matches his exceptional scientific talents with a self effacing good humor and curiosity that few at Harvard manage to display. Meanwhile, Can Knaut, Rivka Bekenstein, Yan Qi, Peter Jan, and Po

Samutpraphoot have already formed a core group of physicists whose skills will ensure that both of our labs remain productive for many years to come. In the Loncar group I've had the deep pleasure of working with Ben Pingault, Graham Joe, Daniel Asumpcao, Michelle Chalupnik, Sophie Ding, and Eliza Cornell. Ben and Graham have taken charge of the basement lab and together form a team that will certainly produce many fantastic results over the coming years. Daniel has stepped into my shoes as the individual responsible for navigating the interface between the two research groups, a skill for which he is already showing great capacity. Michelle has been doing an impressive job of building out collaborations across and outside of Harvard, helping bring new ideas and techniques to the Loncar group. Finally, Sophie and Eliza represent the next generation of diamond fabbers and are already producing amazing devices that will undoubtedly enable exciting new physics and technology. With this talented group and the guidance of our PIs the future for the SIV-nanophotonics effort is bright.

But most importantly, I am thankful for the incredible support of my family. My ability to contribute to this effort is largely in thanks to the continued support of my parents and sister, who played a huge part in making me a scientist in the first place and an even bigger part in motivating and encouraging me when roadblocks inevitably emerged. Most important of all is my wife Abby, who has been my constant companion over the last 5 years, supporting me throughout and helping me navigate this incredibly challenging process. It is impossible to overstate my gratitude for her support. This thesis is dedicated to her.

1

Introduction

1.1 Quantum Networks

The past decade has seem dramatic growth in the availability and sophistication of quantum information processing technology. The emergence of sophisticated techniques for quantum enhanced sensing[1] has provided early demonstration of the possibility of using fundamentally quantum phenomenon such as superposition and entanglement for technological purposes. On the other hand,

the utilization of superconducting qubit technologies for early demonstrations of so called "quantum supremacy" in boson and psuedo random circuit sampling[2] have shown that, in principle, information can be extracted from quantum computations that can not be feasibly obtained using other techniques. Over the next decade, the goal of quantum technologies will be to transition from the regime of "quantum supremacy" to "quantum advantage", or in other words progressing from demonstrating that a singular problem can be solved more efficiently using quantum information processing to demonstration that a useful problem can be addressed using these techniques.

For quantum sensing a route to quantum advantage may already be on the horizon, as applications of high sensitivity detectors for strain and magnetic fields can be easily conceived[3]. Furthermore, implementation of quantum sensing techniques can be accomplished using relatively simple quantum systems whose properties can be carefully controlled. As a result, short term commercialization of quantum sensing is already in progress and likely to occur in the coming years. It is in the realm of quantum computation that the picture becomes more complicated.

Realization of advantage from quantum computation[4] will require large quantum systems, consisting of hundreds of logical qubits (each likely containing several physical qubits) that can be coupled to each other using carefully controlled interactions. The commensurate growth of the computational state-space of this system, combined with unavoidable noise and infidelities, will require sophisticated error correction techniques and place further demands on the hardware used to implement these technologies. The combination of steady progress in quantum computing technology over the past decade and the variety of promising proposals for addressing these challenges makes it conceivable that these challenges will be successfully resolved over the coming years, but the scope of the difficulties should

not be underestimated.

Quantum networking is another quantum technology that lies midway between the relative simplicity of quantum sensing and the sophistication of quantum computation, and shows promise for enabling quantum advantage in relatively simple systems[5]. A quantum network consists of a series of small quantum processors connected to each other via photonic links. These links can be used to entangle two chosen processors connected to this network regardless of the distance separating them. This entanglement can then be used as a resource for secure communication (enabled by so called quantum key distribution[6], or QKD), long distance quantum sensing, or even quantum computation[7].

The relative feasibility of quantum networking can be understood in the context of the reduced size of the individual quantum systems and the relatively small computational state space utilized during their implementation. Each quantum processor need only consist of a single digit number of qubits which need only interact with each in carefully proscribed ways. Because these systems themselves are thus confined to operate in a constrained manner the error correction required to correct for infidelity can be accomplished using simple techniques. As a result, the overhead for creating such systems can be dramatically reduced and "advantage" can be more easily realized.

A further advantage of quantum networking is that the technologies that are required for its implementation will also be useful for future platforms for quantum computation. It has long been understood that introducing an optical interface to a quantum processor, like the one necessary for quantum networking, is a straightforward technique for scaling up the size of a quantum computer. Recent advances in our understanding of all optical or cluster state quantum computing have further cemented the usefulness of realizing such interfaces[8]. Furthermore, quantum communication can act

as enabler for secure and rapid upload of quantum information onto a quantum computer. Introducing new technologies for coupling leading quantum computation platforms to quantum memories used in quantum networks thus is a promising way to scale up to useful demonstrations of quantum computational advantage[7].

Quantum networking thus represents a waypoint between quantum sensing and quantum computing in terms of technological sophistication and feasibility. By demonstrating the utility of quantum technology and allowing for tests of simple quantum computational algorithms this technology can lay the groundwork for the creation of large quantum computational systems while providing economic utility in the short term. This last point may prove critical for securing continued investment should the current wave of quantum computing technologies fail to reach the required levels of operation[9].

Over the past two decades, the identification of a platform capable of being used to create large quantum networks has been a primary goal of the quantum optics community. Target platforms have included essentially all varieties of known quantum emitters, ranging trapped atoms to quantum dots. The key demand placed on these platforms is the ability to act as a "quantum repeater"[10] that catches, stores, and corrects information transferred to the network node by way of information bearing photons. This quantum repeater functionality is required to correct for photon loss that occurs during information transmission, which acts as the dominant information loss mechanism during quantum communication.

One primary challenge has been to ensure that individual quantum memories are able to deterministically interact with individual information carrying photons. To ensure that this occurs, most

quantum memories utilized for quantum networking experiments are placed inside cavities that enhance the interactions between photons and embedded quantum emitters, utilizing the well understood physics of cavity quantum electrodynamics, or CQED[11]. Furthermore, for any viable quantum repeater candidate a mechanism for controlling the quantum memory in question must be identified, with common choices including all optical and microwave control. Finally, true quantum repeater operation requires the ability to deterministically entangle small sets of quantum memories inside individual quantum network nodes. This requires the identification of a choice of ancillary memory and gates between the various qubits used[12].

A quantum networking platform is thus defined by the combination of emitter, photon interaction enhancement mechanism, quantum memory control technique, and ancillary memories employed to realize a platform capable of acting as a quantum repeater. The work presented in this thesis will focus on the dramatic progress demonstrated by the diamond silicon vacancy (SiV) emitter inside diamond nanophotonic cavities, controlled by microwave delivered via coplanar waveguides, and coupled to nearby nuclear spins. At time of writing this platform is one of the leading candidates for the creation of a scalable quantum network due to its desirable optical and spin properties, combined with its compatibility with nanofabrication techniques. By utilizing these properties it has so far been the only platform capable of demonstrating memory enhanced communication- a primitive form of quantum advantage enabled by the platform's high fidelity and low loss operation.

A non exhaustive list of platforms believed to be promising for application in such networks includes the nitrogen vacancy center in diamond[13], the various optically active defects studied in silicon carbide and silicon[14], rare earth atoms trapped in various host crystals[15], self assembled quan-

tum dots[16], optically trapped ions and atoms[17], and atomic ensembles in fabry perot cavities[18]. Rapid progress in the field, however, means that this list will continue to change rapidly over time.

In fact, progress in the field is so rapid that creation of a large scale quantum network by the end of the decade is a plausible goal for the field. Many of the remaining technological barriers to implementation of networks could be resolved through funding of improved cryogenic, nanofabrication, and control technologies. As such, rapid identification and improvement of a promising platform that can act as a test-bed for the introduction and development of these secondary technologies should be a primary goal of the field for the coming years.

1.2 Overview

Chapter 1 of this thesis will begin by introducing diamond as a host material for quantum emitters and giving an overview of diamond color centers in general, with emphasis on the properties of the SiV in particular. Next will come an introduction to CQED, as required to understand the properties of of the SiV photon interface used throughout my PhD. Next will come a section detailing the extensive nanofabrication technique development I engaged in during my PhD, including summaries of currently unpublished efforts towards the creation of novel mask and etching technologies. Finally, I will document the work done towards integrating nanomechanical, nonlinear optical, and microwave control technologies with the diamond nanophotonics platform.

From here on my thesis will follow the standard procedure of documenting some experiments to which I contributed substantially during my PhD. Please consult the papers which represent the cul-

mination of each of these efforts for more information on the results.

Chapter 2 will document my research on strain control of SiV color centers in nanophotonic devices, which culminated in the demonstration of quantum interference between strain controlled color centers inside the same nanophotonic device.

Chapter 3 will contain a description of my work towards the demonstration of an efficient spin-photon interface formed by the SiV inside a nanophotonic cavity. This same section will contain information on our early attempts at enabling gates between the SiV and nearby nuclear spins, including some unpublished data on interactions between the SiV and the nuclear spin of its constituent silicon atom.

Chapter 4 presents a deeper analysis of some of the concepts discussed in chapter 3, and offers insights into the utilization of the SiV-cavity-CPW system for quantum networking applications.

Chapter 5 will conclude the thesis by presenting the application of our platform for memory enhanced quantum communication.

Appendices will be available to present supporting information for these experiments.

2

Diamond Nanofabrication for Quantum Networks

Over the past decade, diamond has emerged as a leading host material for optically active defects, known as color centers, used in quantum optics experiments. One of these defects is the negatively charged silicon vacancy, or SiV, which has exceptional optical and spin properties that make it an im-

portant candidate for implementation of quantum networks[5,7,19,20]. Critical to the utility of this color center is the ability to pattern diamond using nanofabrication tools to form nanophotonic cavities[21]. These cavities can be used to enhance the interaction between the SiV and incoming photons and ensure that information can be transferred between them[22]. Without these (or similar) cavities, the probability of these interactions would be too low for meaningful utilization of these color centers for quantum networking technology. Finally, diamond can also be supplemented with thin metal films that can act as pathways for control signals spanning from DC to the microwave domain. These signals can, when properly routed, be used to control the strain and microwave environments of the color center and thus control its spin and optical properties[23,24].

The primary focus of my PhD has been building a platform capable of integrating these various functionalities while continually improving the performance of our photonic crystal cavities. This section of the thesis will serve to document these efforts, with a emphasis not only on the already successful efforts that have made our current experiments possible, but also on both ongoing and unsuccessful efforts towards new fabrication techniques that provide useful insight into the challenges associated with diamond fabrication.

2.1 Diamond as a Host for Quantum Defects

The study of diamond as a material has gone on for thousands of years, with its name deriving from a ancient Greek word that can be translated as "unbreakable"[25]. This most famous of diamond properties, its hardness, is strangely one its few exceptional properties that has no direct relevance to its

usefulness for quantum optics experiments[26]. Instead, the most relevant property of diamond as a host material is its very wide bandgap of 5.47 eV, which makes it possible for a wide variety of optically active defects to exist within the high symmetry diamond lattice. This wide bandgap is supplemented by a very high speed of sound (a direct result of its hardness) and (commensurately) its exceptional thermal conductivity. These properties combine with low conductivity and microwave loss tangent to make diamond a good host for high power electronics and control signal routing, even at very low temperatures[25].

The primary challenges associated with the utilization of diamond stem from the difficulty of growing or bonding large, high purity thin films of the material on any other substrate. While great progress has been made in the utilization of plasma enhanced chemical vapor deposition (PECVD) for the growth of bulk diamond films from diamond seed crystals[27], these technique can not be adapted to other substrates without the introduction of lattice matching layer[28]. Contamination from these layers and the substrate during the PECVD process then results in a density of impurities that makes the diamonds difficult to use for quantum optics experiments. Improving these processes remains an active and promising area of research, but this challenge remains one for which no straightforward solution is yet known.

As a result of this difficulty, techniques for high selectively etching and undercutting diamond are critical for creation of diamond nanophotonic devices. Here, the hardness and relative chemical inertness of diamond limits the variety of candidate etches that can be reasonably considered. Argon etches and other processes that rely primarily on physical sputtering are possible, but would require exceptionally thick masks due to the low sputter yield of diamond. Chemical etches of diamond rely

primarily on oxygen etching, though steps containing SF6, Cl_2, CF_4, and Ar are also commonly employed[25]. These restrictions place further constraints on the choice of mask. As for undercutting, two primary techniques relying on angled etching[21] and crystallographic undercutting[29] have been developed, each with its specific advantages and drawbacks. The details of these fabrication related considerations will be discussed later in this section.

2.1.1 Diamond Color Centers

The previous section highlighted how diamond is an exceptional host for quantum defects, a fact that has made possible the careful study of the zoo of color centers that have been recognized for decades. These defects form from a combination of impurity atoms and vacancies trapped inside the diamond lattice, giving rise to their alternate name of "vacancy complexes"[26]. Each color center is defined not only by the number and nature of the impurities but also their configuration and charge state. The color center configuration is fixed at room temperature, and can only be changed through high temperature annealing[30], but the charge state can fluctuate as a result of applied electric and optical fields[31]. Furthermore, impurity atoms introduced during or after growth can cause varying levels of lattice damage to the surrounding diamond crystal, resulting in differing numbers of vacancies in the environment and differing optical properties among otherwise identical defects[24]. As a result, isolation and identification of the properties of a single defect requires carefully controlled experiments, as conclusions drawn about a defect in one environment may not hold when even small changes are made to the system.

It thus serves as a striking coincidence that the most common and easily studied color center in

diamond, the negatively charged nitrogen vacancy (NV), has exceptional optical and spin properties that lead to its continued use to this day[32,13]. This color center can be optically addressed and displays a coherence time of more than a millisecond at room temperature. At cryogenic temperatures the NV coherence time can extend to well over a second, and coupling between the NV and nearby nuclear spins can be utilized to store states for over a minute[33,34]. These properties, combined with magnetic and electric field sensitivities, make the NV exceptionally promising for quantum sensing applications that currently stand on the verge of commercialization.

These same properties also make the NV a promising candidate for quantum networking. In fact, many of the seminal quantum networking experiments relied on these color centers to demonstrate loophole free Bell's inequality tests[35], generation of entanglement at rates faster than the decoherence of the system[36], and implementation of entanglement purification[37]. Several of these experiment have yet to replicated on any other system. Despite these impressive demonstrations, large scale implementation of the NV for quantum sensing applications is held back by the sensitivity of the NV to stray electric fields- a sensitivity which complicates their implantation and integration into nanofabricated cavities[38,13]. Instead, photons from the NV are primarily collected through surface etched structures, such as solid immersion lenses (SILS) or through macroscopic cavities comprised of the diamond and an external reflective object, such as a polished fiber[13]. These techniques have already demonstrated impressive utility, and continue to be improved and explored, but have the drawback of preventing true large scale implementation of nanofabrication techniques that serve as a primary motivation for the use of solid state qubits (as opposed to trapped atoms). This deficiency spurred the exploration of alternate color centers in diamond, which led to the emergence of the SiV.

At first glance the properties of the SiV provide few reasons to prefer it over the NV. The slight gains from its longer wavelength are offset by a dramatic reduction in its room temperature coherence time (falling from millisecond to nanosecond scale)[26]. However, early experiments with the SiV noted its dramatically reduced electric field sensitivity, a property that was determined to arise from its D3d symmetry group, which includes inversion symmetry[39]. This inversion symmetry suppresses the static electric dipole moment of the color center and eliminates its first order sensitivity to slowly varying electric fields. This property meant that the SiV could be integrated into photonic crystal cavities fabricated out of bulk diamond to strongly enhance the optical properties of the color center[40]. After it was demonstrated that the SiV coherence time could be dramatically extended by cooling the system to mK temperatures and that the SiV spin state could be directly controlled using microwaves these properties combined to enable a wide variety of new quantum networking experiments[41].

Other diamond color centers are also actively being explored, seeking to improve on the SiV coherence times, quantum efficiency, and optical transition wavelength. Most prominent of these are the other group IV color centers, which are believed to share the symmetry properties of the SiV and should thus display similarly low electric field sensitivities. These color centers have also demonstrated higher quantum efficiencies and better 2 Kelvin coherence times[42,43]. However, experiments involving the GeV implanted into photonic crystal cavities displayed dramatically increased spectral diffusion, likely as a result of increased damage during implantation. These problems can be partially resolved through shallow implantation followed by overgrowth[44], but will continue to act as a limiting factor in terms of color center selection. Also of particular note is the neutral SiV (SiV0)[45] which has been shown to have improved coherence and optical properties when compared to the negatively

charged SiV. A technique that enables stabilization of the charge state of the SiVo inside nanophotonic crystal cavities while enabling efficient photon collection would provide a promising platform from which to explore new domains of quantum optics.

2.1.2 Cavity Quantum Electrodynamics with the SiV

The utility of nanophotonic cavities can be best understood in the context of cavity quantum electrodynamics, a well developed field that describes the interactions between quantum light fields, emitters, and cavities[46]. The following section will provide a brief overview of the primary results of the field as they relate to the experiments described in this thesis.

CQED deals with the properties of quantum emitters inside a cavity as they interact with a quantized light field. The important properties of this system can be understood through three parameters that describe the competing processes for information transfer and loss between the cavity mode, the emitter, and the environment. The single photon coupling rate, g is the first and most important of these. This parameter sets the rate at which information is transferred between a photon in the cavity and a single trapped emitter. This rate can be calculated as

$$g = \vec{E} \cdot \vec{\mu}\hbar$$

$$g \leq \mu\sqrt{\frac{\omega}{\epsilon_0 \hbar V}}$$

Where $\vec{E}$ is the vector electric field induced by a single photon, $\vec{\mu}$ is the electric transition dipole moment, and V is the mode volume of the cavity mode. Mode volume is defined as the ratio between

the integrated intensity of the electric field induced by a single photon, divided by the max amplitude of the field inside the cavity. In other words, a smaller mode volume indicates tighter confinement of photons and a larger peak electric field. Note the inequality presented in the second relation, which is due to the fact that equality between the two terms holds only if the emitter dipole is placed exactly at the mode maximum and is perfectly aligned with the electric field.

The two other rates relevant for CQED systems are the rates at which information is lost into the environment via the emitter, γ, and the rate at which information leaks into the environment via the cavity, κ. The term γ is dominated by spontaneous emission of a photon from the emitter, which occurs at a rate:

$$\gamma = \frac{\omega^3 \mu_{total}^2}{3\pi\epsilon_0 \hbar c^3}$$

Here μ_{total} represents the sum of the transition dipole moments out of the optically excited state. The term κ is a combination of two mechanisms by which photons are lost from the cavity. The first $\kappa_{scattering}$ (hereafter κ_s) represents the rate at which photons scatter out of the cavity into freespace, thus representing information lost from the system permanently. The second cavity loss term $\kappa_{waveguide}$ (or κ_{wg}) is the loss rate of the system into the waveguide. While this term does represent photons lost from the cavity, the information leaked into the waveguide is not lost the experiment. As a result, while the CQED formalism deals only with the summed rates in the form of κ, understanding the utility of the system requires analyzing these two terms separately.

In CQED formalism the cooperativity C represents the comparison between these three rates in

the form:

$$C = \frac{g^2}{\kappa\gamma}$$

A $C > 1$ suggests that a photon inside the cavity is more likely than not to interact with the emitter before being lost, and further improvements in cooperativity lead to commensurate increases in interaction probability. Maximizing this term thus represents a first order goal of practical CQED systems.

In pursuit of this goal, each of the components of cooperativity need to optimized. In practice, γ is largely set by emitter properties, though some emitters like the NV center in diamond can experience substantial increases in γ as a result of increased interaction with the complex solid state environment inside fabricated cavities. In the case of the SiV, this quantity is around 100 MHz and is largely insensitive to fabrication induced imperfection. What variation is experienced is attributed to damage incurred during implantation, which can in principle be eliminated through careful implantation, growth, or annealing techniques. Meanwhile, κ and g are largely determined by cavity parameters and thus sensitive to both the design and fabrication procedures used. Details of the design and fabrication of our diamond cavities can be found in later sections of the thesis. So far, the benchmark numbers for both κ and g are roughly 10 GHz, thus leading to a best case cavity cooperativity of about 100.

At this cooperativity deterministic interaction between photons and emitters is essentially guaranteed, and the question becomes what mechanism should be used to map information between these two systems. Here CQED formalism provides two mechanisms which can be used to mediate this exchange: phase and amplitude measurements applied to photons that have interacted with the cav-

ity emitter system. Each of these gates can be understood by analyzing the equation for the complex reflection coefficient of a CQED system[11]:

$$r(\omega) = 1 - \frac{2\kappa_w(i(\omega - f_a) + \gamma)}{(i(\omega - f_c) + \kappa)(i(\omega - f_a) + \gamma) + g^2} \tag{2.1}$$

Where ω is the photon frequency, f_a is the frequency of the emitter without the cavity, and f_c is the frequency of the cavity without the emitter. As shown in figure 2.1, two effects can be observed in this equation. First, as the probe passes over the emitter resonance a sharp change in phase of the reflected photon occurs. Second, at an energy associated with emitter transition a sharp reflection peak or dip can be observed. Both of these effects can be used to measure interactions between a photon and a cavity coupled emitter. In particular, if an optical transition coupled to an emitter is present inside the cavity at the probe location a sharp variation in the reflection coefficient will result, which can then be used to determine the presence (or state) of the emitter coupled to cavity by measuring the appropriate property of the photon.

The choice of which mechanism is used to measure photon-emitter interactions is usually determined by practical considerations relating to cavity properties. Of particular interest when making this decision is the relationship between κ_{wg} and κ_s. In general, the desire to maximize cooperativity provides incentive to minimize k_{wg}, as this is frequently the term in the equation which can most easily be controlled. However, the variation in the reflection spectra associated with with both the cavity a resonant emitter is maximized when the device is critically coupled, or in other words, when the two κ terms are equal. As a result, operation in the critical coupling regime is usually identified rep-

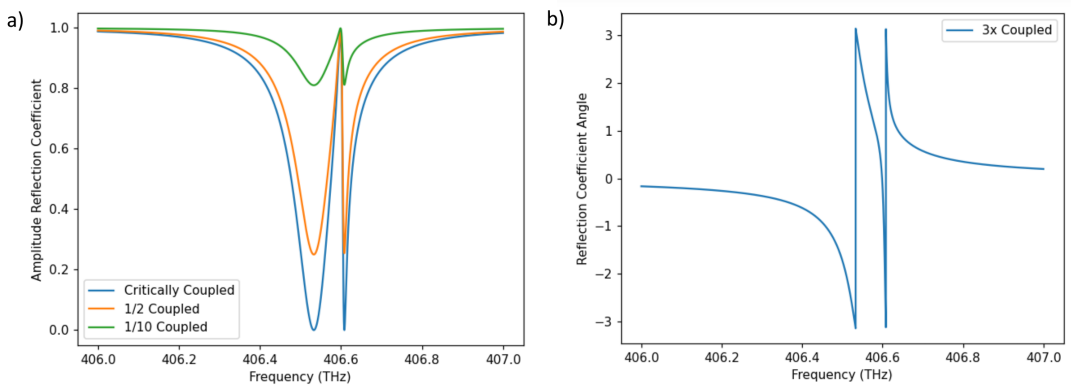


Figure 2.1: Simulated reflection properties of photonic crystal device incorporating a quantum emitter. a) Reflection intensity coefficient of a photonic crystal cavity with a single strongly coupled emitter at different cavity-waveguide couplings. As the coupling deviates further from critical coupling (where loss into the waveguide is perfectly balanced with other losses) the size of the reflection dip decreases, compromising readout efficiency despite the increased cooperativity. b) Phase picked up by a reflected photon bouncing off an overcoupled version of the cavity-emitter spectrum shown in panel a. Here the state of the quantum emitter can be read out by measuring the phase change of the reflected photon, even in this case where the amplitude of the reflection spectra varies very little.

resenting the ideal compromise between maximizing cooperativity and maximizing readout fidelity when utilizing amplitude based readout. This technique is especially appealing because it requires no interferometric stabilization of the optical path used in the experiment.

The drawback of utilizing critically coupled cavities for amplitude readout is that it results in half of the photons that interact with the cavity being lost. In an otherwise well controlled optical setup this can dominate the total loss of the system, and represent the limiting factor on experimental efficiencies. As a result there is an incentive to explore the use of overcoupled cavities, where k_{wg} dominates the system's photonic loss. In this case the total cooperativity of the system and the amplitude variation of the reflection spectrum are reduced in exchange for a larger fraction of the photons being collected into the waveguide mode. However, given sufficiently high cooperativity and the utilization of phase based readout these problems can be overcome, and high readout can be obtained at the cost of more

experimental complexity.

It should be noted that the Purcell enhancement of the optical transitions which occurs as a result of the high cooperativity emitter-photon interface also provides an upper limit on the maximum effective cooperativity which can be used for high fidelity readout. If the Purcell enhancement is sufficiently large that the optical transitions assigned to the different qubit states begin to cross then the fidelity of the readout can begin to drop. In practice, the SiV utilizes differential g factors between the ground and excited optical states of the qubit to differentiate between the two qubit spins states. This differential g factor is small enough that the maximum realizable seperation between the two qubit states is of order 2 GHz. As a result, Purcell enhancement of a factor larger than 20 will begin to cause crossing of the two transitions when the emitter is resonant with the cavity. Thus, cooperativity above this limit will only benefit the system by enabling larger detunings between the cavity and emitter, but will not increase readout fidelity. In this context, transitioning to overcoupled cavities begins to represent an advantage as soon as this cooperativity bound is reached.

2.2 Photonic Crystal Cavities

1D photonic crystals have been studied for more than 20 years, and as a result the literature covering the design and utilization of such cavities is very broad [47]. Here I present a summary of the perspectives I have found useful in my research. This information is not intended to be perceived as completely novel, but merely as a guide for practical implementation of such cavities.

2.2.1 Photonic Crystal Introduction

As discussed in the previous section, cavities can play a key part in enhancing the interactions between photons and embedded emitters, ensuring that information can be transfered between them with high probability[11]. This well understood fact has led to the development of a wide variety of photonic cavity structures, ranging in scale from macroscopic fabry-perot cavities[48] to ultra-small mode volume photonic crystals[49] for use in CQED experiments. As discussed in the previous section, the relevant parameters of these cavities are the quality factor (Q) and the mode volume (V). In general, cavities with smaller mode volume also have smaller quality factors due to a combination of increased overlap of the optical mode with surfaces and increased lateral confinement increasing the scale of the optical momentum variation, both of which contribute to increased scattering. However, below certain bounds the mode volume takes on added importance due to emitter dependent and fabrication dependent effects. For some emitters (such as the NV) close proximity to etched surfaces can degrade the optical properties of the emitter, placing an effective minimum on the realizable mode volume. However, even for CQED systems utilizing very stable emitters, mode volume below a certain point will necessarily cause wide variation in the optical resonances of the cavity modes. This can be understood from first order optical perturbation theory which indicates that the tuning of resonator mode in response to a perturbative shift in the environment's dielectric is proportional to:

$$\delta\omega = -\frac{w}{2}\frac{\int d^3r \delta\epsilon(r)|E(r)|^2}{\int d^3r \epsilon(r)|E(r)|^2}$$

where $\epsilon(r)$ is the local dielectric constant, $\delta\epsilon(r)$ is the perturbation to this constant, and $E(r)$ is the electric field of the unpreturbed mode[47]. From this formula it can be easily seen that a small shift of dielectric constant in a region of very high field intensity will result in a very large shift of the cavity resonance frequency. Combined with unavoidable fabrication imperfections, especially in regions with very small features, this places an effective minimum on realizable cavity mode volumes for a fixed level of fabrication error.

Finding an effective photonic crystal cavity design that maximizes Q, minimizes V, and reduces susceptibility to fabrication errors requires exploring an exceptionally large parameters space of possible designs. Fortunately, a number of theoretical perspectives have been developed to guide the search through this space, such that designs can be meaningfully constrained. In this work, the guiding philosophy behind photonic crystal design was the "psuedopotential" picture, which borrows the language of the standard quantum mechanics problem of "particle in a box" in order to understand the behavior of a trapped photon inside a photonic crystal cavity[50].

To better explain this picture, a brief introduction to photonic crystal cavities will be provided. Classically, photonic waveguides can be understood to operate by trapping light inside a piece of dielectric through total internal reflection. When a ray of light reaches an interface between a high dielectric constant material and a low index cladding material at a sufficient oblique angle the light is perfectly reflected and remains trapped inside the high dielectric constant region. This perspective provides a connection between the "momentum" of the light along the direction of the interface and the probability of its being trapped inside the high dielectric constant material. This connection can be further understood by analyzing the dispersion properties of light inside the high and low dielectric constant

regions. Due to the higher dielectric constant, there exists for a fixed energy some combinations of k vectors (which stands in for the momentum of the light) that can exist inside the high dielectric region but not in the low dielectric region. This can be understood from the linear dispersion relation of light in a homogeneous, linear medium which says that

$$\omega = \frac{c\sqrt{\sum_{i=1}^{3} k_i^2}}{n}$$

Where ω is the energy of the light, c the speed of light in a vacuum, n the index of refraction of the material, and i the standard set of 3 spatial dimensions. For larger values of the index of refraction, larger values of the k vector can be assigned without forcing one of the components to become imaginary. When light with one of these larger k vectors reaches the interface into the lower index region the k vector will be forced to become imaginary along one of these indices, leading to exponential decay of the resulting light field. This causes light to be trapped inside the higher dielectric constant region when it has certain values of momentum.

An interesting phenomenon occurs when this dielectric region is patterned in a periodic manner. In analogy with the well understood formation of Bloch waves in solid state physics, the light propagating through this periodic medium is forced to adopt the discrete transnational symmetry of the underlying medium. Of particular interest is what occurs at the edges of the Brillouin zone, where the k vector assumes its maximal value before folding back onto itself. In this case there are two discrete distributions of light can fulfill both the phase conditions placed on the system by the k vector and the symmetry conditions set by the medium: light can concentrate in either the low or high di-

electric regions with wavefunctions that (to first order) differ only by a half lattice constant offset. In this case the two states will have the same k vector but a different energy, due to the different energy costs associated with concentration of electric fields in regions of different dielectric constant. This phenomenon will result in the formation of a "band gap", or a region of forbidden energies between the energies of these two states. Light at this energy incident on the periodic medium will be rejected through scattering and reflection, creating in effect a highly reflective mirror. It should be noted that this same phenomenon can be understood through the lens of degenerate perturbation theory, where two modes of the same k vector, symmetry, and energy form an avoided crossing that results in the formation of a forbidden energy region.

2.2.2 Photonic Crystal Cavity Design Principles

The formation of this band gap thus provides for a mechanism of creating a controllable, selective mirror that can be fabricated from nanoscale components. Formation of a cavity from these mirror segments can be accomplished simply by placing two of these mirrors in close proximity to each other, resulting in the formation of fabry perot cavity type modes. The behavior of this system can then be loosely modeled through application of the "particle in a box" style analysis. The depth of the potential barrier generated by the photonic bandgap is equal to the energy difference between the energy of the photonic mode in question and the edge of the same symmetry band at the edge of the band gap. A wider band gap with a further detuned target cavity mode thus will confine a photonic state more effectively than a small band gap with the photonic mode only slightly detuned[50].

A further wrinkle is introduced in the form of the possibility of scattering into freespace or guided

modes. Should the photonic mode pick up a sufficiently large momentum kick, either from designed components of the photonic crystal cavity or defects introduced during fabrication, it is possible to couple the cavity mode with undesired loss channels. As a result, introduction of smooth potential gradients which avoid introducing higher order Fourier modes that can cause such scattering is key, and designing a potential well that is minimally sensitive to scattering caused by fabrication defects is important to successful fabrication.

Finally, given the importance of coupling between the waveguide and cavity modes, ensuring that the spatial overlap between the cavity and waveguide modes is maximized is key to effective cavity performance. This is usually achieved by the introduction of tapers to the end of the photonic crystal structure, which serve to match both the mode profiles and band structures between the photonic crystal region and the waveguide.

Given this theoretical guidance, a procedure for straightforward optimization of photonic crystal cavity modes can be assembled. This technique is by no means the only one in use, as other teams have assembled techniques for inverse design and other sophisticated optimization techniques. Nonetheless, the technique presented here can be straightforwardly used to create a wide variety of designs in an intuitive manner. The steps in our procedure are as follows:

1) Parameterize your design space such that designs can be readily compared to each other. This entails selection of a generalized unit cell, usually selected to have either ribbed or perforated components (or sometimes both). Selection of this unit cell is usually set by the desired device application, such as whether the target for photonic coupling is stored in dielectric or vacuum, and what fabrication techniques are available. In general perforated cavities can more easily create large band gaps, as the di-

electric material is removed from the center of the photonic waveguide, thus leading to large dielectric contrast for smaller amounts of material removed. As a result these cavities are usually the preferred. Unit cells are usually parameterized by the lattice constant, waveguide geometry parameters, and the shape and size of the contrast generating deformation of the waveguide structure. There are assigned numerical values such that designs can easily be compared and reconstructed.

2) Identify what regions of the parameter space can generate large band gap structures. This can be done rapidly using either frequency domain photonic simulation or the single unit cell-Bloch boundary condition simulations in the time domain. The goal is to identify whether sufficiently large band gaps can be created subject to the fabrication constraints provided by the techniques and materials used. In general, good band gaps are identified by a large gap to mid-gap ratio and a substantial detuning from the light cone. These parameters maximize the possibility that a low scattering (and thus high Q) resonator can be created out of these photonic crystal structures. The goal is not to identify the "best" structures, but merely to identify regions in parameter space that can be utilized as seeds for future optimization.

3) Parameterize the defect design utilized to form a cavity mode. Decades of nanophotonic crystal cavity research has helped identify the fact that smooth variations in photonic crystal parameters inside a defect cell can lead to higher quality factors and lower mode volumes. This is because slower deviations in cavity parameters produces a commensurately slower variation in the psuedopotential experienced by the trapped photon, which in turn leads to less scattering. As a result, quadratic and qubic variations in unit cell parameters (producing linear and quadratic variation in psuedopotential respectively) are commonly used. Cubic defects have the advantage of enabling smooth transitions in

the derivative of the psuedopotential, which is known to reduce scattering further. Regardless of the function used, the scaling suggested by the function is applied to unit cells, shrinking or enlarging the scales of individual elements. The choice of which elements are changed is set by the purpose of the design and the fabrication technology employed. In the case of the cavities presented in this thesis, only the lattice constant of the photonic crystal was changed, as it was discovered that using uniform hole sizes throughout the design increased nanofabrication yield substantially.

4) Using a numerical optimization technique, seeded by band gap structures resulting from step 2, explore smaller regions of the parameters space to identify the most promising photonic crystal cavity designs. After introducing the extra degree of freedom offered by the depth and nature of the photonic crystal defect, the scale of the parameter space of possible designs is too large to be explore manually. Instead, numerical optimization, targeting the largest possible device figure of merit (usually Q/V, or some variation thereof), can be employed to identify promising candidates with minimal extra overhead. In our case, a gradient ascent optimization tool, targeting a maximum $\frac{Q_S}{V}$ was used, with an artificial cap of 100,000 applied to the quality factor. This cap was set based on known limits of the nanofabrication procedure used, which introduced geometrical and scattering loss that limit quality factors. Repeated iteration of the gradient ascent process, seeded with different promising designs identified in step 2 enabled exploration of a large fraction of the parameter space, and generated a cavity design with quality factor limited by the artificial cap and a mode volume a factor of 6 better than the one generated using more straightforward techniques.

5) By removing mirror segments from the input arm of the waveguide, reduce the Q_{wg} on the input arm until it dominates the loss of the combined system. This effect can be evaluated numerically by

running full cavity simulations with field monitors that select for light emitted through the waveguide arms. In practice the extent of this waveguide damping will need to be calibrated against the true scattering loss induced by fabrication imperfections, requiring cavities with a number of different mirror segment numbers to be fabricated.

6) Introduce tapers to the outside of the photonic crystal cavity. These tapers can be designed and optimized either phenomenologically (by minimizing the excess loss experienced by light reflected off the cavity) or from first principles (by attempting to modulate the photonic band structure in a way that bring the band edge of the photonic crystal structure into contact with the target waveguide mode energy). In either case, the properties of the taper must be parameterized (usually by defining functions for the slow disappearance of the perturbative elements) and simulated either to investigate their impact on the photonic bandgap or the reflection properties of the structure.

It should be noted that this technique requires only small modifications to generate entirely different structures. For example, our attempts to generate overcoupled cavities required modification only of the defect function used and the figure of merit. As a result this technique offers a great deal of utility for generating a wide variety of designs.

2.3 Diamond Nanofabrication

Having discussed the techniques for designing nanophotonic crystal cavities in diamond, the next section will provide an overview of the progress made in fabricating such structures in diamond, and provide context in the form of description of other techniques developed for extracting photons from

diamond color centers with high efficiency.

The speed and fidelity of information transfer between different color center memories dramatically depend on the efficiency with which photons can interact with, and be distributed between, the quantum memories (both on chip and between different chips). This has spurred research activities aimed at realization of low-loss waveguides and optical resonators in diamond. All of these devices require optical isolation provided by refractive index contrast from the surrounding bulk material. One way to achieve this is through free-standing structures that rely on diamond as a device layer and air (or vacuum) as low index cladding. In traditional nanophotonic material platforms, this is accomplished through heteroepitaxial growth or bonding of the device layer on top of a sacrificial layer, which is then etched away to suspend nanophotonic devices[51]. However, the lack of techniques for heteroepitaxial growth of pure diamond thin films on foreign substrates[28] meant that nanofabrication techniques for bulk diamond had to be developed. Focused ion beam milling was initially explored[52], but this approach was limited by device yield and reproducibility. To overcome this, a thin film diamond platform was developed and used in initial diamond quantum photonic experiments[53]. However, this approach turned out to be incompatible with the post-fabrication processing (annealing, acid cleaning, etc.) needed to recover properties of color centers embedded within, particularly their optical coherence and stability. As a result, bulk diamond nanostructuring based on crystallographic[21] or angled etching has been developed.

The rapid development of fabrication technology for coupling individual diamond color centers to itinerant photons has allowed the diamond photonics platform to emerge as a leading candidate for the implementation of quantum networking protocols. Pioneering experiments with the NV center[54],

together with the recent demonstration of memory-enhanced quantum communication based on the SiV center[20], have laid the groundwork for implementation of the full quantum repeater protocol — a technology which would make the creation of long-distance quantum networks possible. Here we trace the development of integrated diamond nanophotonic devices that have enabled the creation of the spin-photon interfaces that form the backbone of these technologies.

2.3.1 Surface Etched Devices for Photon Extraction Into Free Space

The first structures that were developed to overcome total internal reflection at the diamond-air interface, and thus increase the collection efficiency for photons emitted by color centers, were diamond nanopillars[55]. In these devices, light from color centers is coupled to the optical mode of a nanopillar, emitted into free space at the pillar's facet, and collected by a lens. Nanopillars could be fabricated on the surface of diamond using reactive ion etching (RIE), implanted with ions and subsequently annealed to create color centers inside them. Alternatively, they could be fabricated in substrates with sufficient natural abundance of color centers such that each nanopillar probabilistically contained individual emitters. Diamond nanopillars allowed for a ten-fold increase in photon collection efficiency[55] when compared to bulk diamond and have found many applications in quantum sensing and scanning magnetometry[56] in particular. To enhance the light-matter interaction (e.g. via the Purcell effect) needed for quantum information applications, diamond pillars could be surrounded by metal[57]. This, however, came at the expense of increased optical losses introduced by the metal layer.

These early device experiments uncovered an important shortcoming of NV centers: although they are stable emitters in bulk diamond, their optical properties degrade substantially when they are close

to etched diamond surfaces[31]. To address this problem while still overcoming the total internal reflection of emitted photons, solid immersion lenses (SILs) have been fabricated around individually targeted color centers[58]. This could be done either by patterning and then reflowing resist masks prior to etching, or by using focused ion beam (FIB) milling to pattern desired structures. Importantly, NV centers in SILs are separated from the etched surfaces by several microns and thus are less susceptible to fabrication-induced damage. As a result, SILs preserve the stability of optical transitions of NVs while enabling dramatic improvements in photon extraction efficiency. These structures were workhorses in many of the seminal NV center quantum optics experiments[59,35].

Metasurfaces have also recently emerged[60] as a promising platform for achieving high collection efficiency, combining the scalability of the planar nanofabrication technology used for diamond nanopillars with the optical stability characteristic of color centers inside SILs. By carefully tuning the shape and spacing of structures fabricated with top-down etching technology, the emission of a single color center buried microns below the surface of the diamond can be efficiently routed into collection optics.

Research on surface-etched diamond nanophotonic structures has allowed the development of a variety of techniques for collecting light from subsurface emitters without compromising their optical properties. As a result, these approaches are primarily used in concert with color centers which are sensitive to electric fields and other forms of etch-induced damage, such as the NV center. However, these techniques are limited in the overall fraction of emitted photons they can collect by the unavoidable photon emission into the substrate and thus are not sufficient for the realization of efficient spin-photon interfaces.

2.3.2 Freestanding Diamond Devices for enhanced spin-photon interactions

One established route towards an interface between nanophotonic devices and color centers consists of a single-mode waveguide implanted with individual color centers. When properly designed, waveguides enhance the photonic density of states near the emission wavelength of color centers. In addition to diamond nanopillars discussed above, this approach has been pursued in the case of SiV and germanium vacancy (GeV) color centers embedded inside angle-etched diamond waveguides[19,42].

In order to extract emitted photons from the waveguide into an optical fiber, an interface between these two modes must be constructed. This is commonly accomplished through either physical fiber-to-waveguide contact[40] or through vertical couplers[19,61] designed to efficiently scatter light into a collection objective. Examples of vertical couplers include notches, photonic crystal mirrors, and grating couplers. While easy to implement, these approaches suffer from low collection efficiencies. However, recent progress with inverse design techniques suggests that further improvements are possible[61].

Direct fiber collection has so far proved more efficient than vertical coupling, as tapered diamond-to-fiber interfaces have demonstrated the ability to collect more than 95% of the waveguide-coupled photons[40]. This is achieved by tapering the ends of both the optical fiber and the diamond waveguide, creating an adiabatic effective mode transition from the fiber's mode into the waveguide's mode. However, this technique can currently only be used to couple to individual diamond devices, as it requires the use of bulky nanopositioning stages. Permanent bonding of fiber tips to diamond devices — fiber pigtailing — would make it possible to address multiple photonic devices simultaneously.

A final technique for extracting photons from diamond waveguides involves using a pick-and-place

process to couple them to nanophotonic devices patterned in other materials. In this technique, diamond nanophotonic devices are patterned in such a way that they can be lifted individually or in groups as large as 128 devices from the diamond substrate and attached to waveguide devices patterned in more traditional materials[62]. In exchange for added fabrication complexity, this allows for on-chip integration of diamond color centers with materials with nonlinear optical or piezoelectric properties. As a result, this technique shows promise for offering new device functionalities, including complex photon routing and multiplexing, while maintaining the efficient photon extraction required for quantum optics experiments.

Realization of near unity photon collection efficiency as well as high-cooperativity spin-photon interfaces requires the introduction of resonant optical structures to enhance and direct photon emission. Although initial demonstrations using ring resonators and whispering gallery mode structures achieved measurable emitter-cavity coupling[63], photonic crystal cavities have emerged as the dominant technology for resonant enhancement due to their high optical quality factors and small mode volumes. Both one[21]- and two-dimensional[64] photonic crystal cavities have been demonstrated, but the former has been more extensively implemented.

One-dimensional photonic crystal cavities created using an angled etch approach were used to demonstrate spin-photon interfaces with cooperativities $C > 100$[20]. For the demonstrated devices, more than 99% of emitted resonant photons are emitted into the cavity. These photons can be efficiently coupled into the waveguide and, using the aforementioned tapered fiber interface, extracted into the fiber. Microwave coherent control of the color center spin state, another requirement for many quantum optics experiments, can be achieved with on-chip coplanar microwave waveguides[22].

Combining these technologies has allowed for the demonstration of high-fidelity interfaces between photons and long-lived SiV color center spins. These interfaces can be used to entangle photons and quantum memories with high efficiency—a key step to implementing a wide variety of quantum information technologies. For example, a recent demonstration of memory-enhanced quantum communication using this SiV-nanophotonic cavity system is a key step towards the implementation of a full quantum repeater protocol and the creation of large quantum networks. In addition, this technology shows great promise for generating large cluster states with nontrivial entanglement topologies[8]. Pioneering work with the nitrogen vacancy center and the recent preliminary efforts with group IV color centers have demonstrated that diamond color centers can be efficiently linked with nearby nuclear spins[34]. This result in combination with high fidelity spin-photon interfaces could make it possible to form cluster states that can be used for quantum computation or long distance communication.

2.4 Practical Considerations for Diamond Fabrication

The above section detailed the progress made in diamond fabrication over the past two decades. Here we provide more details about specific attempts at improving 1D photonic crystal cavities in the Loncar and Lukin groups over the past 5 years. These efforts were the combined result of efforts of several fabbers within these groups. In particular the contributions of Cleaven Chia deserve recognition, as his attempts at improving telecom wavelength devices paralleled my own work on visible scale devices. Much of the work presented in this section has not yet and may never be published elsewhere, but has been essential to building our understanding of the challenges associated with diamond nanofabrica-

tion.

2.4.1 Angled and Crystallographic Undercutting

As discussed previously, the lack of techniques for heteroepitaxial diamond growth [28] leads to the necessity of using different techniques for optically isolating devices from the substrate. The two best established techniques for diamond are angled and crystallographic undercutting. This section will describe the strengths and challenges associated with each of these techniques.

Angled etching, as conducted in a ion beam etching (IBE) tool [65], has the advantage of allowing maximally reproducible, smooth etches, without concerns relating to etch loading or local pattern density. As long as two features are separated sufficiently that there is no shadowing of the ion beam between adjacent features, there is no cross talk between different elements during the etch. Furthermore, with sufficiently thick mask, small internal features can be sheltered from the angled etch entirely, allowing features of vastly different length scales to be patterned.

Unfortunately this technique does have limitations. The same shadowing that enables this technique to form photonic crystals also limits the variety of different device geometries that can be realized. If two features on the substrate partially protect each other from the etch then the final shape of the two elements will be dramatically changed in a manner that is difficult to predict. As such, bringing two waveguides sufficiently close to each other to enable junctions or couplers to be formed without introducing loss is exceptionally difficult. Furthermore, as discussed later in this thesis, lateral erosion of the etch mask during the etch is an exceptionally difficult problem to resolve, and leads to unpredictable variation in photonic crystal properties. This same lateral erosion also limits the width

of devices that can be practically undercut. As a result, this technique is extremely effective for patterning individual nanobeam photonic crystal devices, but struggles when used to create photonic circuits.

Crystallographic undercutting[29], on the other hand, presents a different set of strengths and limitations. Crystallographic undercutting is capable of generating a much wider variety of structures as shadowing and lateral erosion are not present in this technique. Furthermore, the crystallographic etch is in principle capable of generating almost atomically smooth surfaces, potentially making possible extremely low loss waveguiding. Finally, the ability to execute this technique in a standard RIE system, as opposed to a specialized IBE tool, means that access to this technique will always be much wider when compared to angled etching. As a result this technique can be more easily used for generating large, coupled arrays of photonic devices and for generating high Q, large mode volume structures such as rings and discs.

However, the limitations imposed by this technique are also substantial. The rate of the crystallographic etch varies wildly as a function of the transport of oxygen ions to the underside of the diamond surface. This leads to high sensitivity not only to 10s of micron scale etch loading, but also to shorter scale variations introduced by variations in the photonic device patterning itself. Holes in a photonic crystal, for example, can provide extra access for oxygen ions and speed up the etch rate locally, resulting in a photonic structure that varies in thickness as a function of distance from the holes. Furthermore, while in principle the surface resulting from this etch is set by the crystallographic properties of the diamond, near the edges of structures multiple crystal faces are frequently exposed due to etch loading and local heating, resulting in roughness at corners of suspended devices. Finally, the etch rate

of the crystallographic etch is extremely slow, with undercuts of large devices taking dozens of hours. This can limit the throughput of devices in an academic setting and result in slow turnaround of new devices.

In principle each of the issues with crystallographic etching can be resolved, making likely that it will eventually emerge as the dominant technology for photonic device fabrication in diamond. However, currently the quality of individual devices fabricated using angled etching still leads, indicating that angled etching will continue to play a part in near term development of diamond technology.

2.4.2 Masking Angled Etches

One of the primary challenges associated with angled etching devices in diamond is preventing lateral erosion of the etch mask from unpredictably altering the final device properties. A substantial fraction of the work documented in this thesis was a result of extensive exploration of novel masking techniques in attempt to circumvent this problem. While none of these techniques have so far been able to replace the most established masking techniques, some description of the results and lessons learned from these explorations will be documented here.

The challenge of lateral erosion is unique to angled etching, as mask erosion in traditional top down etching results in changes of the mask thickness but not, to first order, the mask shape. As such the selectivity of the masks used for angled etching must be much higher than those used for top down etching if the final pattern is going to be reproduced faithfully. This problem is made especially challenging by the fact that the highly directional oxygen etch required for good angled undercutting is ill suited for offering high selectivity with most traditional etch masks. For example, the utilization of

organic polymer resists, by far the most common resists used in nanofabrication can be entirely ruled out due to their low resistance to oxygen etching. As such, only hard metal and dielectric masks can be considered. Meanwhile the final structures desired from this fabrication process have features on the 10s of nm scale, requiring very high resolution lithography, a restriction which competes directly with the need for a large mask thickness to protect the insides of the holes during angled etching. Finally, the resulting structures must be extremely smooth to avoid scattering of photons due to roughness.

Due to these varied and often competing requirements, most of the traditional masking techniques used in the nanofabrication community are not feasible for application to diamond angled etching. In fact, the most successful masking technique, utilizing an evaporated titanium underlayer protected by an hydrogen silsesquioxane (HSQ) resist layer has been utilized with only minor changes since in the inception of this process. As such, the strengths and weaknesses of this process deserve special attention.

The Ti-HSQ process, as it is known, is conducted in the following manner. After cleaning, a layer of titanium between 20 and 40 nm is deposited on the diamond substrate. Immediately afterwards, a layer of HSQ with thickness approximately equal to the desired device width is spun onto the the diamond surface. This resist is then patterned using ebeam lithography and developed in TMAH. Two RIE steps are then done back to back. The first, an Ar-Cl etch is used to etch through the Ti layer. The second, an O_2 etch, is used to etch the diamond. After this, the diamond is transferred to an IBE tool and angled etched at the desired angle.

This masking technique has proved so enduring primarily because the HSQ top layer and the titanium (Ti) underlayer each act as the dominant etch mask for one of the two diamond etches. The top-

down RIE process is primarily limited by the HSQ, resulting in sidewalls of the pillars with smoothness set by the HSQ. The titanium then acts as the primary etch mask for the angled etch, utilizing its much higher selectivity to O_2 etching. The HSQ only acts as a shadowmask for the holes during the angled etch process, playing little part in the formation of the waveguides themselves.

The development of this understanding over the past several years can be traced through several attempts at replacing the Ti-HSQ mask with different masking techniques. In particular, three different attempts are worth discussing.

The first of these is an attempt to implement a straightforward mask transfer technique, as commonly used in other nanofabrication platforms. In a mask transfer process a thick underlayer of masking material is deposited, which is then covered with a thinner layer of resist. This resist is chosen such that there exists an etch process which can be used to remove the masking layer with very high selectivity when compared to the resist. When done correctly, this allows a thin layer of resist to be transformed into a much thicker masking layer, which can also be chosen to ensure that the substrate can be etched with very high selectivity when compared to the masking material. This technique can provide very high resolution etching processes, but is also known to introduce extra roughness as a result of the two step etching process.

In diamond, identifying the correct combination of resist and mask material poses a challenging problem. Most dielectric materials, such as SiO_2 or SiN, do not offer sufficiently better selectivity to oxygen etching when compared to HSQ to offset the increased roughness. Instead, metal masks must be considered, as certain metals such as titanium or niobium (Nb) are known to have extremely high resistance to oxygen etching.

For this experiment, mask transfer between PMMA, a standard commercial ebeam resist, and sputtered Nb was attempted using an SF6 ICP-RIE plasma. Subsequently the PMMA was removed and the diamond etching proceeded with the same two O_2 etches employed as in the Ti-HSQ process. Unfortunately, the resulting devices had holes that deviated substantially from the desired elliptical profiles, instead containing sharp points and facets. The irregularities of the holes of the photonic crystal are attributed to the exposed grain structure of the Nb which was patterned onto the diamond during the top down etch. This nanoscale roughness is sufficient to dramatically reduce the quality factors of the resulting devices. Subsequent efforts to control the grain structure of the Nb through annealing or variations of the sputtering conditions were pursued without success. These results serve as evidence of the difficulty of using metal masks for mask transfer procedures, and in general for the masking of top-down oxygen etches into diamond.

In an attempt to circumvent this problem, we developed a (to our knowledge) novel method of forming templated masks out of arbitrary masking material. In this technique a pmma or zep mold is formed using ebeam lithography, and the resulting mold is filled using sputtered material. The partially conformal deposition of masking material onto the resist sidewalls leads to exceptionally smooth patterning of the material, without evidence of grain boundaries that develop as the material becomes thicker. Excess material deposited on top of the resist template can then be removed in a planarizing manner by utilizing an argon IBE process running at a grazing angle. Using this technique the partial planarization accomplished by the conformal sputtering can be turned into an almost perfectly planarized layer. Subsequently dissolving the resist layer using acetone or Remover PG allows utilization of this templated metal layer as a etch mask.

The advantage of this process is that it enables almost any material to be used as a mask- any material can be sputtered in a reasonably directional manner can be used to fill up the resist mold and be subsequently planarized. Because the etch used to remove the excess resist is a physical etch, excessive retch rate dependence on grain structure can be avoided. As a result, the only limitations on the mask geometry are set by the aspect ratio of the features (as it proves difficult to sputter material down deep trenches) and the material properties of the mask, which can limit the total thickness of material deposited. A final challenge for using this technique is associated with elimination of the resist byproducts after planarization, which can be difficult due to the high temperatures reached during the planarizing IBE etch.

Devices patterned using this technique reveal dramatically improved adherence to desired cross section profile. As such, these devices are expected to produce much higher quality factor devices after optimization of the process. Development of this procedure is currently ongoing, but represents one of the most promising strategies for improving angled etched triangular cross section devices.

A final technique for circumventing nonuniformity induced by lateral erosion is using a single layer mask. For example, utilizing a nm scale layer of alumina to provide the adhesion for the HSQ (instead of the titanium used previously) makes possible the usage of a mask that acts in a monolithic manner, as the thin layer of alumina provides essentially no barrier to the angled etch. In this case the lateral erosion observed is dramatically greater than in the Ti-HSQ case. However, this lateral erosion operates in a uniform manner that can thus be corrected for by changing the lithographic patterning and the angle of the IBE. As a result, devices patterned in this manner have higher peak optical quality factors than those patterned using Ti-HSQ, despite the increased magnitude of the process effects.

This technique, however, imposes limits on the geometries of the devices that can be patterned, as the extent of the lateral erosion makes it impossible to form certain patterns. Furthermore, these devices are less reproducible, as the variations in the resist thickness unavoidable when spinning HSQ on 3 by 3 millimeter are exaggerated when attempting to etch through a large quantity of resist.

From these three processes, a few key lessons can be learned. First, grain boundaries play a key part in determining the properties of chemically transferred etches. Doing mask transfer into a high selectivity material by using a chemical etch can result in unacceptably high roughness. Second, metals patterned using physical techniques- such as argon milling or templating- can act as an optimal, high selectivity mask that avoids exposing grain boundaries. Third, lateral erosion is not in and of itself the limiting factor in fabricating diamond photonic crystal by angled etching. The true constraints are imposed by the irregularities of the HSQ spinning process and the other elements of the fabrication process. Transitioning to resist with more uniform spinning profiles and larger substrates will help reduce the impact of these issues.

2.4.3 Simulating Angled Etching

As discussed above, the angled etching process poses many unique fabrication challenges that need to be resolved before the full potential of the technique can be realized. Towards this end, we developed a set of simulation tools that could be used to test which aspects of the angled etch were responsible for producing the unique features which were observed. The goal was to reproduce the SEM shown in figure 1.3a. Three features of this SEM stand out as deviating from the intuitively expected cross section. First is the curvature of the device profile observed on the front corners of the cross section.

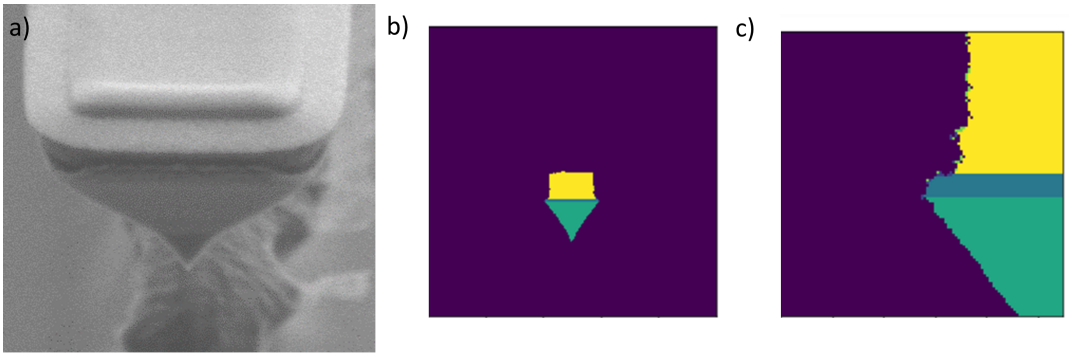


Figure 2.2: Photonic device cross sections deviate from desired shape due to lateral erosion and fabrication defects. a) Scanning electron micrograph (SEM) of cross section of photonic crystal device after angled etching. Device was fabricated using the Ti-HSQ mask and shows several nonideal properties, including rough top edges, rounded corners, and deformed lower corners. b) Simulations were used to develop understanding of the photonic device cross section nonidealities. Yellow is HSQ, blue is Ti, Dark green is diamond, light green is redep from the mask. c) Close up of corner of simulated structure. SEM by Cleaven Chia.

Second is the lip formed underneath the top corners of the triangle, where the surface is noticeable rougher. Finally, we observe the curvature at the bottom corner of the triangle. Each of these features stands in contrast to the expected smooth triangular cross section utilized in the photonic simulations, and thus represents a source of excess loss. It should be noted that these effects are only observed with multilayer masks- the alumina-HSQ mask described in the previous section did not display any of these undesired effects.

Simulations were conducted in python using Monte-Carlo techniques. Ions were generated at the edges of the simulation region with an initial trajectory and position randomly selected from those which could be produced by an ion beam etcher. These ions were then propagated towards the diamond feature in discrete time steps. When the ion reached the surface of the diamond or the mask the unit cell where the ion made contact was damaged with inverse proportion to the hardness of the material. When sufficient damage is accumulated the dielectric atom is ”sputtered” loose either specu-

larly or with a randomly chosen exit angle, depending on the simulation run. These sputtered atoms are also discretely time stepped through the environment and (when they land on dielectric surface) are redeposited such that they need to be etched again. The etch rate of materials was also adjusted based on the incidence angle of the ion, in line with results reported previously[66]. Finally, sticking coefficients for various materials can be used to enable specular "bouncing" of ions off the resist surface. Each of these quantities were calibrated from literature or measured.

The results of the simulations can be seen in figure 1.3b. Simulations shown were run using relative etch rates extracted from real fabrication runs. The angular distribution of the sputtered atoms is set to be half random and half specular. The structures resulting from these simulations are in line with naive expectations- showing a steady formation of a freestanding triangular structure. Unfortunately, none of the unexpected results observed in the SEMs of the device cross sections are observed in these simulations. While this to first order represents a failure of the simulation project, it does confirm that the effects observed are a result of other, less predictable processes. As such, we have developed a number of hypothesis that could explain the differences between the simulated and the observed results.

First, it was observed that certain metal masks imparted sufficient stress into the diamond to deform the suspended nanobeam waveguides. If this deformation occurs as a result of stress released from the mask then this stress will cause different amounts of deformation as the steady undercutting of the beam causes different strain patterns to emerge, exposing different regions fo the device to the etch as it progressed. Predicting this deformation as a function of etch time would be a very difficult challenge.

Second, it is known that sputtering of material onto (and then off of) the grids in double grid IBE

systems can result in steady redeposition of mask material onto the substrate being etched. This redeposition is difficult to prevent due to the lack of an established chamber cleaning technique like those used in traditional RIE systems. IBE grids are usually cleaned manually after dissembling the tool, a technique that is not feasible for use before every etch. Furthermore, other higher order redeposition processes from the substrate, the wafer holder, and other regions of the IBE chamber could be contributing to the redeposition as well, making it unclear if a grid cleaning procedure would resolve the issue.

Finally, we hypothesize that the ArCl etch used to etch through the titanium produces some residual Ti-Cl byproducts that are not completely removed by the argon component of the etch. The fact that the Cl etch partially undercuts the HSQ is responsible for the smoothness of the holes after the top down O_2 etch. As a result, it would be unsurprising if this same, difficult to characterize undercut produced angled etch behavior that is unpredictable. This last hypothesis would also explain the difference in etch profiles observed when comparing the Ti-HSQ mask the the alumina-HSQ mask.

While the simulations failed to provide direct insight into the causes of the strange device profiles observed, they have allowed us to eliminate some potential causes of the device profiles observed. This has enabled increased focus on the second order causes discussed above.

2.5 Nanophotonic Technology Integration

In order to act as an effective quantum network node diamond photonic crystals must be functionalized by incorporating SiV color centers and external control knobs onto the diamond substate. The

following section will provide a brief summary of the techniques employed for these purposes.

2.5.1 Microwave, RF, and strain Delivery

Microwave and RF control signals can be used to address the spin states of the electron and nuclear spins respectively. These signals are most commonly delivered via metallic waveguides coupled to signal generators and amplifiers, though some experimental platforms utilize microwave horns to direct their microwave signals towards their qubits without utilizing on chip microwave waveguides.

In our experiment, microwave and RF delivery is accomplished through microwave coplanar waveguides (CPWs) patterned onto the substrate diamond. These CPWs can most easily be patterned through liftoff, as utilization of etch based patterning requires either exposing the photonic crystals to plasma (and thus degrading the photonic crystal properties) or else doing a multistep write process to protect the photonic crystals before patterning the CPW material.

Execution of liftoff onto the diamond substrate is accomplished using the following procedure: First clean the diamond, starting with an aqua regia clean to remove any indium solder, and following up with HF and Piranha cleans before drying out of IPA. Next cover the diamond in 5 layers of MMA EL11 (Microchem) using a 45 second spin at 4K RPM, with a 1 minute bake at 180C in between each of the spins. This should be followed by 2 spins at 3K rpm of PMMA 950C4 (Microchem), each followed by a 1 minute bake at 180C. It should be noted that this recipe results in a roughly 2 um thick layer of resist, which is sufficient to protect the photonic crystals under a roughly 800 nm layer of resist. Reducing the number of EL11 spins should make it possible to pattern slightly higher resolution features without compromising the protection of the photonic crystals, should this be desired. Next a

layer of espacer is spun onto the diamond at 2K rpm for 1 minute, without any spin up step. Without further baking the diamond, transfer it into the EBL tool as quickly as possible to avoid degradation of the espacer layer. Utilizing an aligned write, expose the fine alignment markers with the dose appropriate for your accelerating voltage (for 125 keV $1500uC/cm^2$ is effective). Remove the diamond from the EBL tool, remove the espacer layer through a 60 second dip in water, then develop the resist in MIBK:IPA (1:3) for 60 seconds before drying out of IPA. Respin the espacer in the same manner as before and replace the diamond inside the ebeam tool. Align and expose the final device layer. Remove the diamond and develop the resist as before, and place the diamond inside a barrel asher for a descum. Descum should be run with a pure O2 plasma operating at 100 watts for 60 seconds. Next, transfer the diamond into an ebeam evaporator tool and deposit 20 nm of Ti and 300 nm of Au, after allowing the system to pump down to the low 10^-6 range. Be aware that thicker deposition can cause the gold to delaminate after repeated thermal cycling of the diamond.

CPW designs are simulated in Sonnet (Sonnet Software, Inc) with the goal of maximizing field intensity at the SiV location and minimizing undesired reflection and loss. The design is chosen to be a 50 Ohm line with a short at the end to concentrate the field at this location. The intensity of the field is further increased by constricting the CPW around the location of the SIV, driving up the current nearby.

This constriction unfortunately limits the number of SiVs that can be addressed simultaneously, as the series of constrictions causes the majority of the heating. To bypass this issue work is currently underway to transition to NbTiN CPW. This requires a multiwrite scheme to first protect the photonic crystals, then sputter deposit the NbTiN, pattern resist onto the NbTiN, and finally etch through the

NbTiN layer. Currently the process is limited by difficult to remove resist residue on the surface of the photonic crystals.

These same techniques can be used to form the electrostatic capacitors used to deflect waveguide and control the strain environment around the SiV. In this case electrodes are patterned both onto and below the suspended structures- thus requiring the thicker MMA/PMMA layer described in the methods. In this case designs should be simulated using COMSOL (COMSOL Group) to ensure that sufficient strain can be localized around the SiV. Care should also be taken to avoid pull-in of the capacitors, where strain deflects the capacitor plates sufficiently to start a runaway process that results in the two capacitor plates being pulled loose from their housing and into contact with each other. Furthermore, the Au layer can be replaced by tantalum to minimize the effects of electrically induced migration should extremely high voltages be required.

2.5.2 Masked Implantation

Initial efforts at fabricating photonic crystals incorporating quantum emitters relied on bulk growth of emitters, identification of the location of promising candidates, and fabricating photonic crystals around them[67]. This technique has the dual drawbacks of limiting the number of devices that can be fabricated at once while requiring two alignment steps (thus reducing the overall accuracy of implantation). In diamond this technique was quickly supplanted by the use of focused ion beam (FIB) implantation[68], where photonic crystals are fabricated first and implanted using a collimated beam of the target ionic species. This technique can in principle produce very high accuracy implantation, as FIB secondary electron imaging can operate at extremely high resolution. Unfortunately the tools

and sources used for FIB implantation can be unreliable and hard to come by for some implantation materials, and the throughput of these techniques can be quite slow.

As a result the decision was made to return to the masked implantation techniques more often used in nanofabrication foundries. In particular, the same scheme for masking liftoff could be used for masking implantation, as the stopping distance of 100 keV silicon ions in PMMA was deemed to be less than a μm using SRIM simulation. The primary change to the procedure was that implantation spots were patterned at $3000 \mu C/cm^2$ to compensate for reduced proximity effects. The masked diamonds could then be sent to a commercial foundry (Innovion Inc) where bulk ion implantation could be used. While masking is still limited by the throughput of the EBL tool, bulk implantation itself is very reliable and high throughput, as this technique has been optimized for commercial applications.

Using this technique, calibrated through use of SRIM simulations[69], ions can be localized to a point with accuracy limited by a combination of 3 factors. The first is the size of the implantation spot that can be realized. This spot size is set by the maximum aspect ratio which can be realized using the masking resist, which for our experiment is roughly 60 nm. Next is the alignment error of the EBL, which is limited to roughly 30 nm (best case) for our Elionix F125 tool. Finally, there is straggle induced by ions colliding with diamond atoms after implantation. SRIM simulation suggest that this straggle is roughly +-50 nm. From these errors an expected uncertainty in alignment of +-83 nm is expected in the xy plane and +-50 nm in the Z plane. The addition of further alignment steps will increase the alignment error by $\sqrt{n}$, where n is the number of alignment steps. Improving this accuracy will be possible by using thinner, higher stopping power resist, improving the alignment accuracy of the EBL tool, and utilizing shallower implantation followed by overgrowth to reduce each

of the 3 contributions to error. This is necessary to realize deterministic creation of high cooperativity cavities as the 80% mode maximum of the photonic crystals is roughly 60 nm across in all directions, thus leading to reduced cooperativity if the alignment error is larger than this quantity.

In general, diamond overgrowth is a valuable tool which should be explored further as a part of the diamond nanofabrication toolset. Overgrowth of electronic grade diamond on top of implanted SiV color centers promises to improve spectral uniformity and spatial clustering of SiV color centers- allowing new forms of interaction to be engineered between nearby quantum emitters. The same technique could be used for nanophotonic cavity resonance tuning- potentially increasing the yield of device fabrication. Finally, diamond overgrowth could allow for new device geometries to be realized by overgrowing low stress thin films on top of diamond, graphitized through dense ion implantation. As such this technique should be developed and explored further.

3

Quantum Interference of Strain Controlled SiV Color Centers

One of the primary challenges associated with using solid state quantum memories for quantum technology purposes is managing undesired interactions between the quantum emitter and the solid state environment. Where single trapped atoms in vacuum can count on having essentially identical envi-

ronments as long as experimental conditions are maintained, solid state emitters are surrounded by solid materials that can not only vary between different emitters in the same material, but can also change over time. These variations and fluctuations can have a number of detrimental effects on the properties of the emitters that can often be difficult to suppress. As such, the selection of emitters with fewer mechanisms for interacting with their environment, such as the SiV, offers an advantage. However, even relatively insensitive emitters like the SiV still suffer from variations in the environment due to large strain fields that can develop inside materials damaged during ion implantation or nanofabrication. The SiV's response to this unpredictable strain fields means that no two SiV color centers are exactly alike.

These variations between color centers can take a number of forms depending on the intensity and orientation of the strain. The most obvious impact of strain variations on the SiV is the existence of the so-called inhomogenous distribution of spectral lines. This means that different color centers have different energies associated with their optical transitions- making it difficult for photons emitted by one color center to interact with a different color center. Strain also plays a part in determining the magnetic field susceptibility of the SiV spin transition, leading to differences in how efficiently spin conserving readout and spin state control can be performed. As a result, substantial preselection is required to identify SiV color centers for use in single emitter experiments. This is feasible for comparatively simple experiments, but in scaling up to larger systems this preselection will eventually become a limiting factor in the size of the system that can be feasibly realized. As such, introducing a tuning knob that enables control of the SiV properties would be beneficial.

Unfortunately, the side effect of minimizing the interactions between the emitter chosen and its

environment is that this also minimizes the number of tools that can be used to control the emitter properties. As such, the SiV is to first order not sensitive to electric fields, the most common tuning knob of choice for controlling quantum emitter properties. At the same time, the rapid introduction of magnetic fields of sufficient intensity to tune SiV properties is a very challenging project. Instead, strain itself is the best tuning knob to correct these inhomogenieties. In fact, previous experiments utilizing electrostactically bendable cantilevers have shown that strain can be used for these purposes- in addition to potentially extending the coherence time of SiVs at 4 Kelvin by several orders of magnitude. The following work represents an attempt to make this technique compatible with both the diamond photonic devices developed in previous years and the quantum optics experiments that utilize them by integrating nanomechanical strain control with diamond photonic waveguides. As a proof of concept for this technique, two strain tuned emitters are tuned into resonance with each other and shown to produce an optical phenomenon tied to the formation of an entangled state. This demonstration lays the groundwork for further attempts to integrate strain control and photonics utilizing by photonic crystal cavities.

3.1 Introduction

Solid-state emitters with inversion symmetry[26] are promising for use in optical quantum networks due to their ability to be integrated into nanophotonic devices[19,41,68,70]. These emitters have suppressed static electric dipole moments, decreasing the susceptibility of their optical transition frequencies to fluctuations of electric fields that occur near device surfaces[26,68]. This fundamental property has been

leveraged most notably with the negatively charged silicon-vacancy center in diamond (SiV) to achieve emitter-photon interaction with cooperativity greater than 20 in nanophotonic cavities[70]. The platform developed around this color center also provides other essential components for quantum networking, such as a long-lived quantum memory[41] and efficient photon collection[40].

Nevertheless, in terms of advancing towards multi-qubit networks, even inversion-symmetric and other electric field insensitive[71] emitters present challenges when incorporated into nanophotonic devices. They exhibit a significant inhomogeneous distribution of their optical transition frequencies as well as residual instability in the form of spectral diffusion[26,68]. Demonstrating full control of their spectral behavior is necessary to generate mutually indistinguishable photons, the key ingredient for long distance entanglement[72]. Because these emitters cannot be spectrally tuned using electric fields, the established tuning mechanism for solid-state emitters[59,38], previous experiments involving indistinguishable photon generation from such defects have relied on Raman[19,73] and magnetic field[70] tuning. However, these techniques constrain either the spin or optical degree of freedom of the color center and are challenging to implement in the multi-qubit regime.

Inspired by experiments involving semiconductor quantum dots[74,75], initial experiments with diamond cantilevers have demonstrated the capacity to tune single SiV centers using strain[76,39]. However, the suitability of this approach for photon mediated entanglement of multiple emitters remains an open question. In this work, we show that strain control can be used to manipulate the optical resonances of solid-state emitters and generate quantum interference between them. The demonstrated integration of strain control with nanophotonic devices represents a key step towards the realization of scalable quantum networks.

3.2 Waveguides With Strain Control

Our devices, presented in Figure 3.1, consist of triangular cross-section waveguides fabricated from single crystal diamond[21,65]. Each of these waveguides is connected to a support structure on one end (Figure 3.1b). The other end is tapered to allow for collection of photons from the waveguide into an optical fiber with better than 85% efficiency[40] (Figure 3.1c). In order to embed SiV centers within diamond nanophotonic devices, we adapt a masked implantation technique previously used for bulk substrates[77]. We implant silicon ions at a density of $2 * 10^{12}\ ions/cm^2$, a density similar to that used for cavity QED experiments[70]. After the creation of SiV centers, gold electrodes are patterned onto the devices such that metallized parts of the waveguide act as one plate of a capacitor, with the other plate located on the diamond substrate (Figure 3.1b). Applying a voltage difference to these plates generates a force that deflects a portion of the waveguide, applying electrically controllable strain to the embedded SiV centers. This strain field perturbs the diamond lattice around the SiV which shifts the Coulomb energy of the orbitals and tunes the frequency of the optical transitions[26].

We measure the strain response of two SiV centers 30 μm apart within the same diamond device by resonantly exciting their optical transitions and collecting their phonon sideband emission at 4 K (Figure 3.2). The difference in the position of SiV centers in the device accounts for the difference in their response to the applied voltage[39], allowing us to overlap their optical transitions (Figure 3.2, red inset). The waveguide supports (Figure 3.1a, rounded gray region) between the SiV centers act as a mechanical clamp preventing strain from propagating and impacting spectral behavior of color centers in the portion of the waveguide beyond the clamp. We observe a tuning range of over 80 GHz (150 pm),

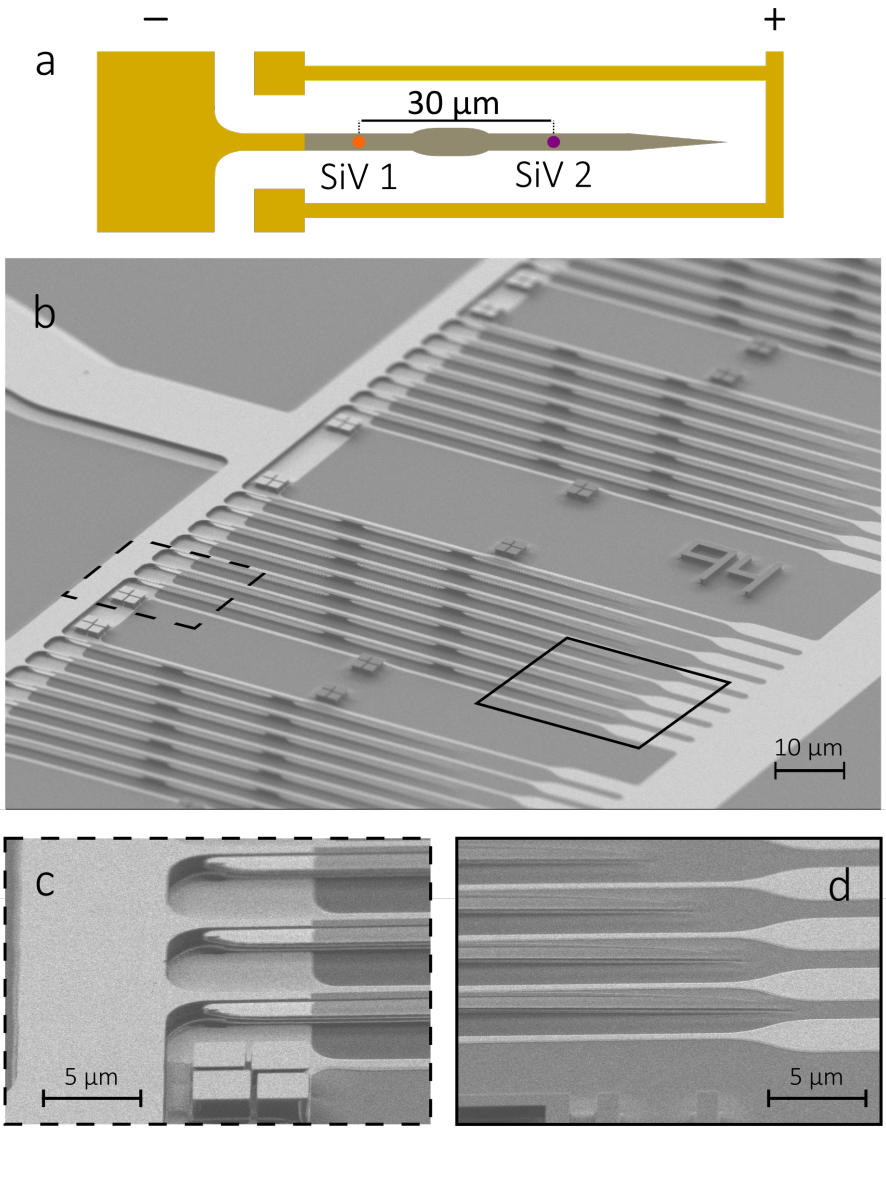


Figure 3.1: Schematic of diamond nanophotonics device. a) Diamond waveguides (gray) are implanted with color centers (purple and orange) at desired locations on the device. Electrodes (gold) are used to define a capacitor between plates located on the device (negative terminal) and below the device (positive terminal). Applying bias voltage between the plates causes the deflection of the doubly clamped cantilever. This tunes color centers between the plates and the first clamp (orange spot) without perturbing color centers beyond the clamp (purple spot). b) Scanning electron micrograph (SEM) of the photonic devices. c) Capacitor plates located on and below the devices. d) Diamond tapers used to extract photons from waveguides. This enables the extraction efficiency of more than 85% from the diamond waveguide into the fiber.

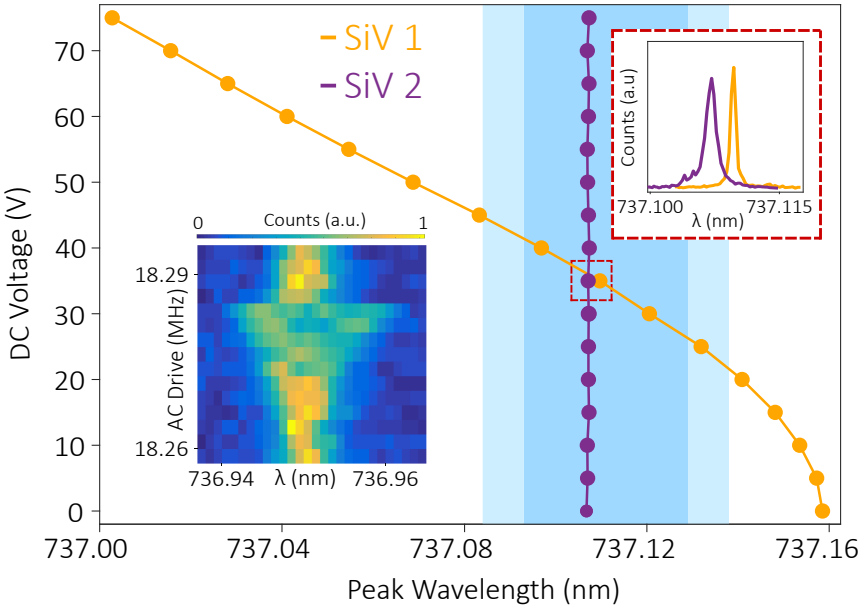


Figure 3.2: Characterization of DC and AC voltage response of the devices. Voltage bias is applied to the capacitor plates, resulting in strain fields that tune the optical transitions of SiV1 in the deflected portion of the device (orange) compared to the optical transitions of SiV2 in the stationary regions (purple). The tuning range of the SiV color center greatly exceeds the inhomogeneous distribution for 50% (75%) of SiV color centers observed in this experiment shown in dark (light) blue shading. The red inset shows the photoluminescence excitation spectra of two color centers at a voltage near the overlap. The blue inset shows the AC response of the cantilever system, measured by observing SiV optical transitions while modulating the AC driving frequency. Driving the cantilever resonance with its mechanical mode results in linewidth broadening of the color center optical transitions.

a factor of 3 larger than the total inhomogeneous distribution of the SiV optical transitions measured in these devices (Figure 3.2, blue shaded region). This is sufficient range to completely eliminate the effects of static strain variations on SiV optical transitions.

To determine the bandwidth of our electromechanical actuation scheme, we investigate an SiV color center's spectral response to AC mechanical driving of the nanophotonic structure (Figure 3.2, blue inset). We apply a DC bias combined with a variable-frequency RF signal to the gold electrodes and monitor the SiV optical transition. When the RF drive frequency matches one of the nanobeam's mechanical modes, we observe linewidth broadening of the SiV coupled to this mechanical mode due to the resonant amplification of the driving signal[78]. Using this technique, we observe and drive modes with mechanical frequencies of up to 100 MHz. Optimizing the device design could enable the electromechanical driving of vibrational modes with GHz frequencies which are resonant with SiV spin transitions. This could open new possibilities for engineering coherent spin-phonon interactions[76].

3.3 Mitigation of Spectral Diffusion

The high bandwidth of our electromechanical actuation scheme is sufficient to suppress spectral diffusion exhibited by the SiV center[68]. Monitoring an SiV center's optical transition over the course of five hours, we observe spectral diffusion that is an order of magnitude larger than its single-scan linewidth of around 300 MHz (Figure 3.3a). Using a pulsed feedback scheme that applies a voltage adjustment every 20 seconds we reduce the total summed linewidth by almost an order of magnitude on a timescale of several hours (Figure 3.3b). The efficacy of this feedback scheme is limited by the

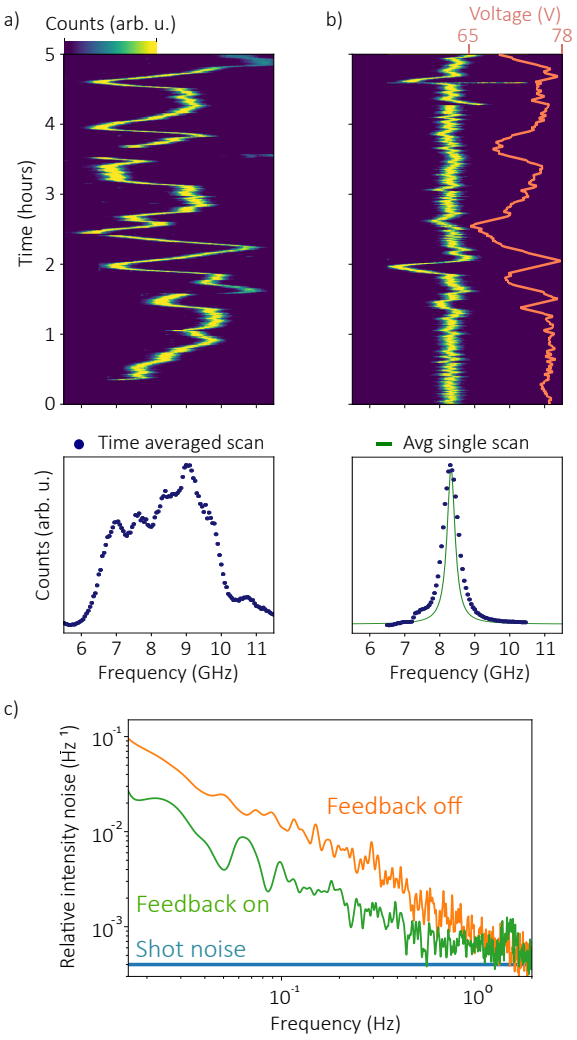


Figure 3.3: Reduction of spectral diffusion using nanomechanical strain. a) Top: Spectral diffusion of SiV center optical transition, measured over a 5-hour period. Bottom: Time-averaged spectrum over the same period. b) Top: Measurement of the SiV spectral diffusion with 20 second pulsed feedback over a 5-hour period. Bottom: Time-averaged spectra over a 5-hour period (blue dots) show the reduction of total linewidth down to 500 MHz. The average of single-scan SiV linewidths is 350 MHz (green line). c) PSD of measured SiV count fluctuations with (without) feedback is presented by the green (orange) line, showing reduction of noise by an average of 8 dB. Blue line indicates statistical noise limit set by finite photon emission and collection rate.

long duration of the laser scan used to capture the full extent of the spectral diffusion. This results in imperfect locking of the SiV optical transition to the target frequency. The bandwidth of this spectral stabilization technique is improved by performing a faster 5 Hz sweep around a narrower region around the position of the SiV center optical transition. We monitor the noise spectrum of the SiV center emission with and without a lock-in feedback scheme applied to the device voltage (Figure 3.3c). The application of feedback results in an intensity noise reduction by approximately 8 dB, consistent with the stabilization achieved in Figure 3.3b. We attribute the frequency component dominated by the 1/f noise to slow strain fluctuations and second order susceptibility to electric field fluctuations in the SiV environment. Beyond this regime, our feedback scheme is limited by photon shot noise (Figure 3.3c). Further improving the SiV count rate through Purcell enhancement using a cavity could enable higher frequency feedback, as the existing scheme uses only a small share of the available actuation bandwidth.

3.4 Observation of Quantum Interference

With the optical transitions of the SiV centers tuned and stabilized, we proceed to generate probabilistic entanglement between two color centers. We begin by using strain control to set the optical transition frequencies between the lower branch of the ground state ($|c\rangle$) and the excited state ($|e\rangle$) of two emitters at the target detuning (Δ) by applying the appropriate voltage (Figure 3.4a). The transitions between the upper branch of the ground state ($|u\rangle$) and the excited state ($|e\rangle$) of the two emitters are then continuously excited using two separate lasers (Figure 3.4a). Finally, the photons emitted into

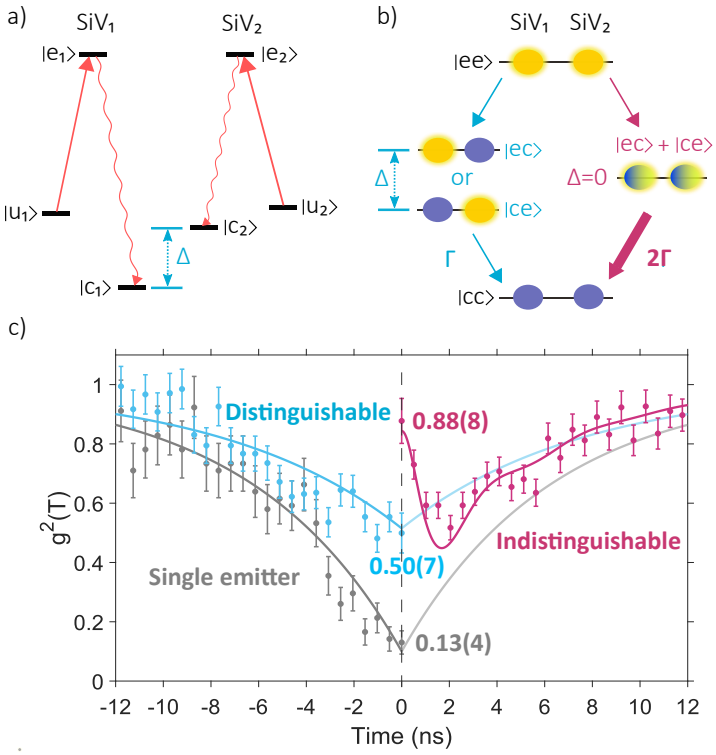


Figure 3.4: Observation of the superradiant entangled state using strain control. a) Level structure for two SiV centers. Strain tuning of one SiV color center changes the detuning (Δ) between their $|e\rangle$ to $|c\rangle$ transitions. Separate lasers are applied to excite the $|u\rangle$ to $|e\rangle$ transition of each emitter. b) A single photon emitted from the two excited emitters with distinguishable transitions ($\Delta \neq 0$) projects the system to a statistical mixture of $|ec\rangle$ and $|ce\rangle$ states (blue decay path). When the emitters are indistinguishable ($\Delta = 0$), the emission of one photon projects the system into a superradiant bright state (purple decay path) that decays at a rate two times faster than that of the statistical mixture. c) The second order photon correlation function is measured for a single emitter (left panel, gray data points) and for two spectrally distinguishable emitters (left panel, blue data points). Measured $g^{(2)}(0)$ is 0.13(4) and 0.50(7) for the single emitter and distinguishable cases, respectively. Exponential curves fit to the data are plotted and mirrored onto the right half of plot (gray and blue lines). For two emitters tuned into resonance, we observe the generation of a superradiant entangled state, signified by the peak in the photon correlation (right panel, purple data points). Data is overlaid with a simulated model with a single fitting parameter. For indistinguishable emitters, we measure $g^{(2)}(0) = 0.88(8)$, limited primarily by detector jitter.

the diamond waveguide are collected through a tapered fiber interface and filtered using a high finesse Fabry-Perot filter in order to separate the desired optical transition from the excitation laser[19].

We characterize our setup by measuring the second order correlation function between photons from a single excited SiV center (Figure 3.4c, left panel). We observe the suppression of photon coincidences with $g^{(2)}_{single}(0) = 0.13(4)$, a quantity raised above its ideal value of 0 by dark counts of the photon detectors. Next, we simultaneously excite both SiV centers and measure their photon correlation function. When two excited SiV centers are spectrally detuned ($\Delta \neq 0$), their emitted photons are distinguishable and the detection of the first photon projects the system into the statistical mixture of the $|ce\rangle$ and $|ec\rangle$ states (Figure 3.4b, blue path)[19]. In this case, the zero-time-delay photon correlation function reaches $g^{(2)}_{dist}(0) = 0.50(7)$ (Figure 3.4c, left panel).

When the two SiV optical transitions are tuned into resonance ($\Delta = 0$), detection of the first emitted photon from a pair of excited SiV color centers projects the system into an entangled, bright state (Figure 3.4b, red path). This results from the indistinguishability of the emitted photons, which eliminates the information about which SiV produced the photon. This bright state is identified by the superradiant emission of a second photon at twice the rate expected compared to the distinguishable case[19,79]. This increased emission rate results in an increased probability of observing photon coincidences- resulting in the creation of a peak in $g^{(2)}(0)$. We confirm the generation of an entangled state by observing this superradiant peak in the photon correlation function (Figure 3.4c, right panel) with $g^{(2)}_{ind}(0) = 0.88(8)$. Experimental results are in good agreement with a simulated model of our system (Figure 3.4c, red curve) which uses only a single fitting parameter, the phonon-induced mixing rate between the $|u\rangle$ and $|c\rangle$ ground states[80]. Using the height of the superradiant peak and

the value of the $g^{(2)}_{single}$, we calculate a lower bound on the conditional bright state fidelity to be 0.8(1), indicating the observation of an entangled state[19].

In particular, the $g^{(2)}$ data presented in the right panel of Figure 3.4 can be understood as consisting of two parts. First, the "dip" with a decay timescale of about 10 ns occurs because photons collected in this experiment can only be generated from the $|e\rangle$ state, and the detection of a photon leads to projection of the system into the $|c\rangle$ state. The timescale of the dip then corresponds to the average amount of time between the emitter arriving in the $|c\rangle$ state and it being excited to the $|e\rangle$ state. This timescale is primarily set by the ground state mixing rate between $|c\rangle$ and $|u\rangle$ states in our experiment, but in cases of low laser driving power can also be broadened by the slow Rabi driving between the $|e\rangle$ and $|u\rangle$ states. The second feature is the superradiant peak. Theoretically, the width of this peak should be set to roughly 1 ns (half of the excited state lifetime), as superradiant effects should dominate at this timescale. In reality, both the electronic jitter and the laser power impact the measured width. The total electronic jitter measured in our detection electronics is 350 ps, a timescale comparable to the anticipated peak timescale of 1 ns, leading to broadening of the measured feature. Fast laser driving could also reduce the timescale of the peak by providing another driven decay channel (stimulated emission) from the bright state. The oscillations in the $g^{(2)}$ for indistinguishable emitters result from a combination of small mismatch between emitter optical transitions and Rabi driving between the $|u\rangle$ and $|e\rangle$ states in line with the theory.

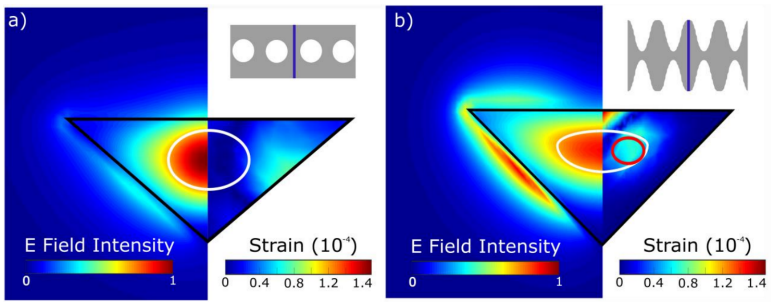


Figure 3.5: Scheme for strain tuning SiV color centers inside photonic crystal cavities. a) Optical (left) and strain (right) fields inside perforated photonic crystal cavities (inset). Blue line in inset represents cross section shown in electric field and strain plots. Strain is measured along one of the TE-oriented SiV axis. White contour indicates region with optical field intensity greater than 70%. Perforated structure requires compromising either optical or strain field intensity at color center position. b) Optical and strain fields inside ribbed cavity (inset) with simulated quality factor Q > 25,000. White contour indicates the region with optical field intensity greater than 70%. Red circle indicates potential SiV implantation spot with optimized optical and strain field coupling.

3.5 Strain Tuning in Cavities

These observations demonstrate the potential of the developed strain tuning technique to enable optically mediated interactions between spatially separated emitters. A strain-tunable, solid-state emitter strongly coupled to a nanophotonic cavity could represent an important component of a scalable quantum network. We note that current experiments using diamond photonic crystals rely on a diamond waveguide perforated with an array of holes , where the fundamental optical mode has poor overlap with the strain field induced when the device is deflected (Figure 3.5a). Dramatic improvement in the overlap between the optical and strain fields could be achieved by transitioning to a "ribbed" cavity design , where the unit cell is defined by a thin central waveguide structure with external corrugation (Figure 3.5b, inset). A suitable SiV implantation spot (Figure 3.5b, red circle) would allow for the tuning of implanted SiV centers by an average of more than 50 GHz. Using finite-difference

time-domain simulations, we developed an optimized cavity design with simulated Q of greater than 25,000 and mode volume of 1.21 $(/n)^3$. We estimate that a cooperativity C > 6 could be achieved in such ribbed cavities. Furthermore, by implanting a fraction of the color centers in regions of the cavity with low strain but high optical field intensity, SiV centers coupled to the same cavity could be tuned relative to each other. This could make it possible to rapidly modulate their cavity-mediated interactions, a potential basis for designing multiqubit registers in single quantum network nodes.

3.6 Discussion

We show a scalable approach to generating quantum interference between solid state emitters in nanophotonic devices using strain. Using our electromechanically controlled strain field, we realize a reduction of spectral diffusion by almost an order of magnitude over a broad bandwidth and achieve a spectral tuning range exceeding 150 pm (80 GHz), several times greater than the SiV inhomogeneous distribution inside nanophotonic devices. This approach can be directly adapted to other quantum emitters such as quantum dots, other inversion-symmetric color centers in diamond with higher quantum efficiency [81], as well as other electric field insensitive emitters [71]. Furthermore, high frequency strain control inside a nanophotonic cavity can lead to a photon or phonon mediated gate between quantum memories [70,82,83]. By combining long lived quantum memories with a high cooperativity nanophotonic interface and a direct mechanism for ensuring optical indistinguishability, the SiV platform fulfills the requirements for a scalable quantum network node and paves the way for realization of large-scale quantum networks.

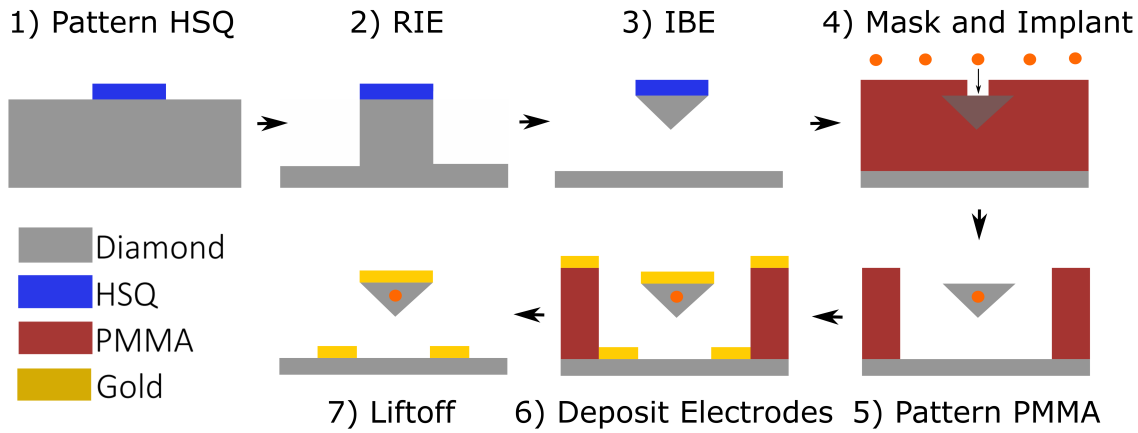


Figure 3.6: Schematic of nanofabrication process. Diamond waveguides are fabricated using top-down and angled etching technique into the diamond substrate [21,84,65]. This was followed by patterning apertures on top of the fabricated structures through which Si+ ions can reach the diamond substrate at desired locations [39]. Finally, we deposit gold electrodes on top of and below the diamond devices [69,40], which serve to deflect fabricated waveguides when a voltage is applied between them.

3.7 Device Fabrication

This section describes the fabrication of the nanophotonic devices presented in Figure 3.1 of the main text. The device fabrication presented in Figure 3.6 was based on the techniques developed in [21,84,65]. The fabrication scheme for cantilever deflection was based on [39].

Single-crystal diamond substrates were obtained from Element 6 (CVD grown, <5 ppb [N]). The substrates were mechanically polished, cleaned with a boiling 1:1:1 mixture of sulfuric acid, nitric acid, and perchloric acid (hereafter referred to as a "triacid" clean), and etched using the argon-chlorine etch (Unaxis Shuttleline ICP-RIE) to ensure maximum substrate smoothness.

We prepared the diamonds for fabrication of the photonic devices using a piranha and hydrofluoric acid clean. A 10 nm stiction layer of titanium was deposited using electron beam evaporation, followed

by spin coating with HSQ resist (FOx-16, Dow Corning) diluted in methyl isobutyl ketone (MIBK) (Figure 3.6, step 1). This resist was then exposed using electron beam lithography and developed in 25% TMAH (Sigma-Aldrich). This was followed by a reactive-ion etch (RIE) using an argon-chlorine mixture to remove exposed titanium, followed by an oxygen RIE (Unaxis Shuttleline ICP-RIE) which transfers the mask pattern into diamond (Figure 3.6, step 2). The ridge waveguides are transformed into freestanding triangular cross section waveguides using an oxygen etch at an angle of 40 degrees from the normal using an ion beam etcher (Intlvac Nanoquest II) (Figure 3.6, step 3). The etch mask was removed with a hydrofluoric acid clean, and the devices were dried in a critical point dryer.

In order to prepare the diamonds for implantation, the devices were again cleaned using piranha and hydrofluoric acid and then repeatedly spin coated with PMMA C4 (MicroChem) resist and a single layer of espacer 300Z (Showa Denko America), which served as a conductive layer. A multistep electron beam alignment procedure was then used to align to markers etched into the diamond and expose the desired implantation spots. Devices were rinsed in water and then developed in a mixture of MIBK and IPA for 60 seconds. The PMMA-coated devices were then sent for implantation with silicon ions (Innovion) (Figure 3.6, step 4) with the desired dose and implantation energy calculated using SRIM simulation [69]. This method, inspired by previous work in the NV center community [77], can be executed using standard electron-beam lithography tools, greatly increasing the accessibility of the SiV platform, which previously required specialized focused ion beam tools for implantation. Additionally, the same technique can be used to implant a variety of color centers into patterned substrates. The diamonds were then triacid cleaned, annealed at 1200 C, and triacid cleaned again in order to turn implanted Si ions into SiV centers while removing damaged diamond from the surface of the devices.

Creation of implanted SiV color centers was verified with a room temperature confocal microscope.

The final step in device preparation was the patterning of electrodes. The devices were acid cleaned and coated with layers of MMAEL11 (MicroChem) and PMMA C4 (MicroChem), patterned using ebeam lithography (Figure 3.6, step 5), and then coated with a 10 nm thin layer of titanium followed by 100 nm layers of gold using an electron beam evaporator system (Figure 3.6, step 6). Liftoff was then performed using heated Remover PG (MicroChem) (Figure 3.6, step 7), leaving deposited gold electrodes on top of and below the fabricated nanostructures. Wire-bonding to the mm-scale bonding pads provided leads through which voltage could be applied to the capacitor plates.

Fabrication of the tapered fibers followed the procedure documented in [40]. Thorlabs S630HP fibers were stripped of cladding and dipped into piranha using a home-built dip coater. A bath of hydrofluoric acid covered in a layer of o-xylene (Sigma-Aldrich) was prepared and the fibers were dipped into this mixture. By controlling the rate of the fiber extraction from this mixture we were able to control the angle of the fiber taper which optimizes the efficiency of photon extraction from the diamond devices. During experiments, the tapered diamond end is brought into contact with a tapered optical fiber using a nanopositioning stage. Once contacted, we achieve adiabatic transfer of photons from the diamond waveguide into the optical fiber with efficiency greater than 85%.

3.8 Setup

The experiment was carried out using a closed-cycle 4K Helium Cryostat (Fusion F2 Montana Instruments). The layout of the setup is shown in Fig. S2. The position of the sample and the tapered

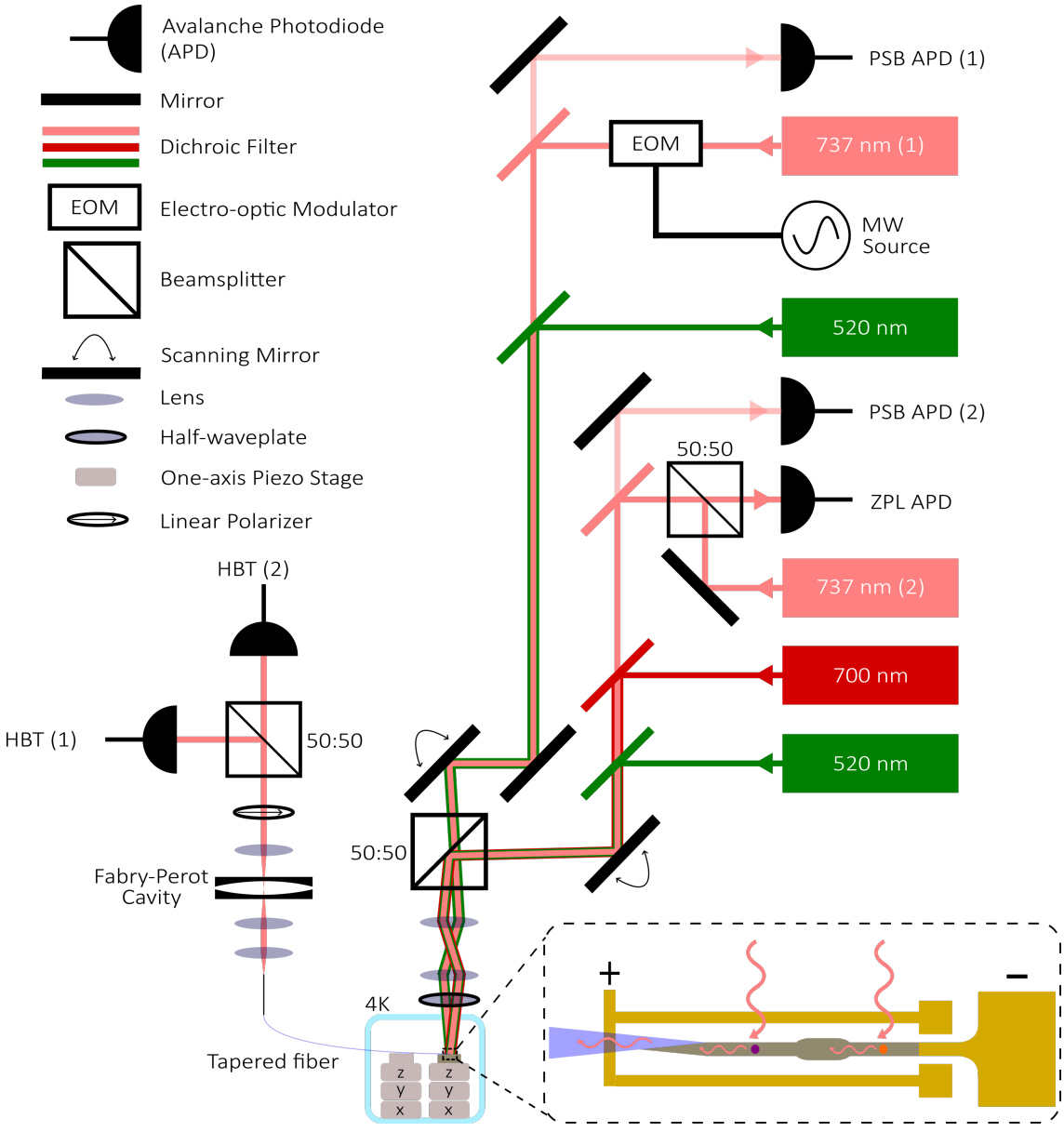


Figure 3.7: Overview of the setup used in this experiment.

fiber were controlled independently with two stacks of three axis piezo-based nanopositioning stages (Attocube: 2x ANP X101 and 1x z102 each) controlled with piezo controllers (ANC 300 and ANC 350 respectively). Strain was applied to the sample nanobeams by applying a voltage difference (from 0 to 100 volts) between two gold capacitor plates (Keithley Series 22020 voltage source). During experiments the leakage current resulting from 100 V applied bias was observed to be less than 50 nA, corresponding to less than 5 μW of heating. Based on COMSOL (COMSOL INC) simulations we estimate that the electric field at the SiV location is less than 10^4 V/m. From the SiV transition dipole moment of 14 Debye[85] we calculate that this corresponds to a second order Stark shift of roughly 1 MHz.

To allow for the independent excitation of spatially separated SiV centers, we set the location of the two independent excitation positions using two scanning mirrors (Newport FSM300 and Mad City Labs MCLS02813). We periodically pulsed a green laser (Thorlabs LP520 nm) to repump our SiV centers into the negative charge state. This laser was run at a power of 10 μW on a 10% duty cycle. For identifying the location of the SiV centers within the diamond waveguide, an off-resonant 700 nm laser (Thorlabs M700F3) was scanned along the waveguide and the color center's zero-phonon line (ZPL) emission was collected via free space using an avalanche photodiode (APD; 4X Perkin Elmer SPCM-AQRH-14-FC). Resonant excitation of SiV centers was performed using a continuous wave tunable Ti:Sapphire laser (M-Squared SolsTiS-2000-PSX-XF) and a homebuilt external-cavity diode laser (Opnext Diode HL7302MG, Littrow configuration) and the longer wavelength SiV phonon-sideband (PSB) emission was collected using a free-space APD. Fast modulation of the Ti:Sapphire laser sideband used in the feedback schemes described in Figure 3 was performed by sending the laser

through an electro-optic modulator (iXBlue photonics NIR MX800) with a microwave frequency modulation input (HP 83711B, capable of operating up to 20 GHz).

A significant part of the SiV emission coupled to the diamond waveguide mode and was collected by a tapered optical fiber (collection efficiency of about 85%). This emission was then launched into free space and sent through a home-made, tunable, high-finesse (500 MHz linewidth, 150 GHz FSR) Fabry-Perot cavity frequency filter. This filter separated the SiV fluorescence from excitation laser photons scattered into the waveguide.

In the experiment involving two emitters (Figure 4), this frequency filter was used to guarantee successful spectral overlap of the two SiV centers' emission lines. Their emission then passed through a linear polarizer which erased any polarization mismatch (containing which-path information) between the two emitters, followed by a Hanbury-Brown Twiss (HBT) interferometer consisting of a 50:50 beam splitter (fiber coupled) with equal arm lengths and two APDs. A time correlator (Picoharp PH300) connected to the two APDs of the HBT interferometer was then used to measure the second-order photon correlation function.

The photon correlation function of indistinguishable emitters (Figure 4c, right panel) was obtained by programming the automatic start of the 0.5 second long measurement sequence conditioned on the APD count rate passing the set threshold value. This threshold value ensured that the photons emitted from both SiV centers passed through the Fabry-Perot cavity, which signified that their optical transitions were on resonance and the emitted photons were indistinguishable. In the case of the count rate dropping below the threshold value, strain would be applied until the count rate through the cavity filter was again maximized and the experiment would proceed. This mechanism also stopped

the experiment when mechanical drift of the Fabry-Perot cavity or the optical alignment decreased the measured count rate. In all we estimate that the total duty cycle of our experiment was 45.3%, limited primarily by instability of the Fabry-Perot cavity. In the experiment measuring the photon correlation function of distinguishable emitters (Figure 4c, left panel), this overlap was not ensured and the polarizer was removed from the beam path, making the emitted photons distinguishable.

3.9 Feedback Scheme

In order to lock an SiV optical transition to a target wavelength, two different feedback schemes were used.

In the first scheme, chosen to give visual demonstration of the efficacy of the strain-tuning technique, we collected SiV phonon sideband emission produced during a 20 second long laser scan to extract information about the optical transition frequency. The resulting absorption profile was then fit using a Lorentzian with 3 fitting parameters, accounting for the peak wavelength, amplitude, and width of the SiV spectral line. A single voltage step was then executed to move the peak wavelength of the spectral line towards the target value, after which another scan began. This scheme underutilized the mechanical bandwidth of our actuation scheme and a substantial fraction of the duty cycle was spent on the slow and wide laser scan.

The second scheme was chosen to maximize bandwidth of the spectral diffusion correction. Instead of using a direct laser scan, an electro optic modulator (EOM) sideband of the excitation laser was scanned using a variable frequency RF source. This scan was much faster compared to the laser scan,

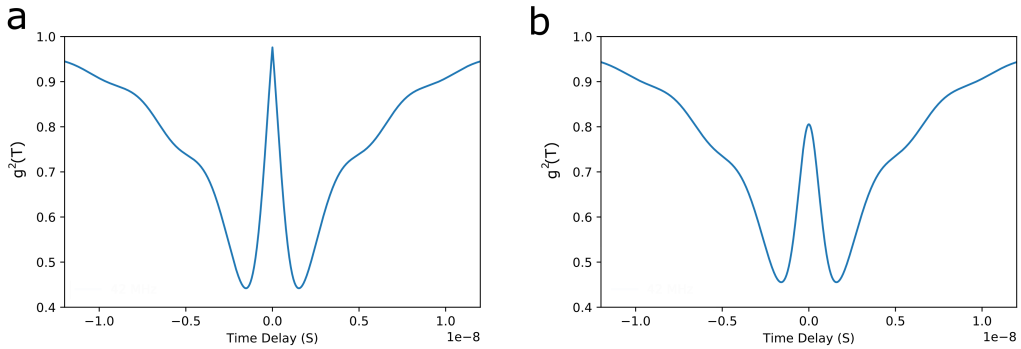


Figure 3.8: Simulated photon correlation function for two emitters on resonance without (a) and with (b) inclusion of electronic jitter measured in the experiment.

potentially allowing for modulation at up to around 100 Hz, limited by the switching time of the RF source. By scanning the EOM sideband over the target position of the SiV spectral line, a similar absorption profile could be generated. By implementing a software lock-in scheme, we were able to rapidly turn this absorption profile into an error signal which could be used to correct the voltage applied to the cantilever.

We note that, at high strain and in a magnetic field aligned to the SiV axis, the SiV spin transitions are to first order insensitive to strain field fluctuations [22]. As a result, high bandwidth stabilization of SiV optical transitions should minimally impact the electron spin levels of the SiV color center. Further, strain does not, to first order, break the inversion symmetry of the SiV [26].

3.10 Emitter model and simulation

In this section we present a model to describe the generation of an entangled state between two SiV centers and the results presented in Figure 4. We simulated our system through the Lindblad Master

Equation formalism using the QuTIP software package[80]. Each SiV center is governed by a single emitter Hamiltonian defined by:

$$H = \omega_e \left|e\right\rangle \left\langle e\right| + \omega_u \left|u\right\rangle \left\langle u\right| + \Omega \left|e\right\rangle \left\langle u\right| + \Omega \left|u\right\rangle \left\langle e\right| \tag{3.1}$$

where ω_e is the energy associated with the excited state, ω_u is the energy of the upper branch of the ground state, and Ω corresponds to the driving rate associated with the laser power. In this case the $|e\rangle$ state is the lower spin-orbit branch of the excited state, while $|u\rangle$ and $|c\rangle$ represent the upper and lower branches of the ground state respectively. Because we operated in the weak driving regime and photons can escape rapidly from our waveguide coupled color centers, we truncated our Hilbert space to:

$$\left|ee\right\rangle, \left|ec\right\rangle, \left|ce\right\rangle, \left|cc\right\rangle, \left|eu\right\rangle, \left|ue\right\rangle, \left|uu\right\rangle, \left|uc\right\rangle, \left|cu\right\rangle \tag{3.2}$$

leading to the states with at most two excitations and 0 photons being included in the simulation. Each individual emitter was also subjected to a series of collapse operators representing coupling to the environment and incoherent population transfer between energy levels. These took the form of:

$$\begin{aligned} C_1 &= \sqrt{w_1}\left|c\right\rangle \left\langle e\right| \qquad & C_2 &= \sqrt{w_2}\left|u\right\rangle \left\langle e\right| \\ C_3 &= \sqrt{w_3}\left|u\right\rangle \left\langle c\right| \qquad & C_4 &= \sqrt{w_4}\left|c\right\rangle \left\langle u\right| \\ & & C_5 &= \sqrt{w_5}\left|e\right\rangle \left\langle e\right| \end{aligned} \tag{3.3}$$

which represent, in order, the decay between $|e\rangle$ and $|c\rangle$, the decay between $|e\rangle$ and $|u\rangle$, the ground state mixing rate (up and down), and the fast spectral diffusion, along with their associated rates. The ground state mixing is a result of phonon occupation at the 50 GHz energy scale, which occurs at 4K. Finally, to account for the slow component of the spectral diffusion, the simulation was run repeatedly with the positions of two SiV center spectral lines independently and randomly chosen from a Gaussian distribution. The results of these iterations were then averaged. This enabled us to account for the dynamic effects on the time scale of a single experimental run (fast diffusion, tens of ns) and variations over the course of a single data collection period (slow diffusion, minutes) in simulations.

The initial state of the system was defined to be the two-emitter steady state, as calculated from the Lindblad formalism. Detection of the first photon corresponds to one application of the relevant collapse operator C_1. In order to calculate the two-emitter $g^{(2)}$ the collapse operators were applied to the system using the definition[19]:

$$g^{(2)}(t) = \frac{Tr\{C_1^\dagger C_1 \tilde{\rho}(t)\}}{Tr\{C_1^\dagger C_1 \rho\}} \tag{3.4}$$

Term ρ is the steady-state density matrix of the two emitter system and $\tilde{\rho}(t)$ represents the density matrix at time t after application of the collapse operator C_1, corresponding to the first photon being detected.

In order to model our experimental system, variables were extracted from our measurements and from the theoretical properties of the SiV centers. We set the average separation between the spectral lines of the two emitters to be 250 MHz, which is half of the filter cavity linewidth (a conservative

estimate), and the driving power of the laser was matched between measured and simulated saturation curves such that counts were produced at 2/3 of the saturation rate. Only the ground state mixing rate was fit to the measured $g^{(2)}$ dip timescale, visible in red line fit in Figure 4c of the main text. All other parameters could be extracted directly from optical and electrical measurements in our system.

Simulations using these parameters predicted a $g^{(2)}$ curve as shown in Figure 3.8. When no model is used to account for the jitter in detection electronics the peak of the $g^{(2)}(0)$ goes to 1 (Figure 3.8). However, in our system the jitter of the detection electronics was measured to be roughly 350 ps, a substantial fraction of the lifetime of the feature being measured. This jitter was modeled as convolution of the original $g^{(2)}$ signal with a Gaussian of the appropriate width. As a result of this jitter, the peak height of $g^{(2)}(0)$ was reduced to 0.85 (Figure 3.8), in good agreement with measured results. Using low jitter detectors in our experiment would increase the contrast of the superradiant feature observed in Figure 4.

3.11 Bright State Fidelity Analysis

A lower bound on the conditional fidelity of the generated bright state can be extracted from the two photon correlation measurements[19]. We begin by calculating the impact of the avalanche photodiode (APD) noise counts on our measurements. In our single emitter photon correlation measurement we observed a non-zero $g^{(2)}(0)$ primarily due to dark counts in our detectors. Considering the possibility that either one or both photons of the coincidence measurement was a noise photon we found that:

$$g_1^{(2)}(0) = \frac{p_{n,1}(2 + p_{n,1})}{(1 + p_{n,1})^2} \tag{3.5}$$

where $g_1^{(2)}(0)$ is the zero-time delay two photon correlation measurement for a single emitter and $p_{n,1}$ is the relative probability that a photon measured when exciting a single emitter is a noise photon. In our system $g_1^{(2)}(0) = 0.13(4)$, which results in a $p_{n,1} = 0.07(3)$. Because the dominant source of noise is the detector dark counts, the noise probability was halved in the experiment with two emitters, resulting in $p_n = 0.04(2)$.

In our experiment involving indistinguishable photons emitted from two SiV centers, both emitters were continuously excited and the excitation power was individually set to balance the measured counts from each emitter. For notational simplicity, in this analysis it was assumed that the driving power was weak enough that the admixture of the $|u\rangle$ state into the excited component of the bright state was negligible. As a result, the conditional density matrix for the system after detection of a single photon is:

$$\tilde{\rho} = \frac{1}{1 + p_n}(p_e^{(0)}\tilde{F}\,|B\rangle\,\langle B| + (1 - p_e^{(0)}\tilde{F})\rho_d) + \frac{p_n}{1 + p_n}\rho \tag{3.6}$$

where $p_e^{(0)}$ represents the probability that an emitter is in the excited state, $\tilde{F}$ represents the fidelity of the bright state if the two SiVs begin in the excited state, ρ_d is the density matrix representing all non-radiative states, and ρ is the steady state density matrix. The first term of this equation represents the state of the system if the detected photon originated from the excited emitters. The second term represents the case of the photon originating from the detector noise. This density matrix produces a

conditional $g^{(2)}$ function of the form:

$$g^{(2)}(0) = \frac{\tilde{F} + p_n(2 + p_n)}{(1 + p_n)^2} \tag{3.7}$$

which allows us to extract this conditional fidelity from our photon correlation measurements. In order to introduce our second postselection step, the probability p_c^{ee} that the system started in the doubly excited state given that two photons were detected must be calculated. This can then be used to convert $\tilde{F}$ into the correct conditional fidelity F through the relation $F = \tilde{F} p_c^{ee}$. The probability can be obtained using the relative rates of photon production by emitters and dark counts calculated above:

$$p_c^{ee} \geq \frac{\tilde{F}}{\tilde{F} + p_n(2 + p_n)} \tag{3.8}$$

From this we can calculate a lower bound on the conditional fidelity of:

$$F \geq \frac{(g^{(2)}(0)(1 + p_n)^2 - p_n(2 + p_n))^2}{(g^{(2)}(0)(1 + p_n)^2} = 0.8(1) \tag{3.9}$$

This value is limited by the jitter in our detection electronics, indicating that performing measurements with lower jitter would result in substantial improvements in the fidelity of this bright state.

The nature of the bright state generated in this experiment is dependent on the excitation power used. When driven well below saturation, the bright state in this system is defined as $|B\rangle = (|ec\rangle + |ce\rangle)/\sqrt{2}$ state. Increasing the driving power of the resonant laser increases the admixture of the $|u\rangle$ state into the excited component of the bright state. This does not change the fidelity calculations

used but does result in a different definition of the bright state observed.

The creation of the bright state in this system is not fully heralded by detection of a photon due to the three-level structure of the emitters used in this experiment. The probability of finding both emitters simultaneously in the excited state at any given point of time is low: less than 10%, according to the steady state simulations of the model described above. As a result, detection of the first photon will produce the bright state only a fraction of the time. Calculation of the concurrence conditional on photon collection[19] yields a negligibly small (roughly 0.1 sigma) concurrence for this experiment. This could be improved by employing a pulsed excitation scheme or using other deterministic schemes for entanglement generation.

3.12 Conclusion and Next Steps

The results presented here indicate the capability of strain to be used to tune color center optical transitions into resonance in a manner compatible with quantum optics experiments. This capacity is exceptionally useful for tuning not only the optical transition frequencies of the color centers, as demonstrated here, but also for controlling the magnetic field and phonon sensitivities of the SiV spin state. For example, it has been demonstrated that, when is experiences sufficient strain, the SIV coherence time can be extended by several orders of magnitude at 4 K. Being able to control these SiV properties should simplify local entanglement of SiV color centers within a single quantum network node, a key step in any implementation of quantum repeater protocols. These same techniques will also be applicable to other diamond color centers or even other electric field insensitive solid state emitters in other

materials. As a result, strain control of color centers represents a prime avenue for further research.

In order to advance this technology further a series of technical hurdles must be overcome. The most important of these is the transition to ribbed cavities to replace the perforated cavities currently in use. Designs for these cavities have already been developed in several groups, but implementation of these designs in diamond is hindered by the availability of appropriate nanofabrication techniques. The formation of ribbed cavities using angled etch techniques is rendered extremely challenging by the redeposition of mask material inside the enclosed portions of the ribs. This places a maximum aspect ratio on the depth of the ribs which is insufficient for the realization of good cavity modes. As a result, such ribbed cavities can be most easily realized using a crystalographic etch with reduced sensitivity to device geometry.

This obstacle could also be bypassed by engineering new axis along which strain could be applied. Sheer strain applied through the doubly clamped cantilever can propagate through perforated cavities in a manner that is impossible with axial strain. This technique is however, also dependent on the implementation of crystallographic etches, as realization of photonic elements separated from each other on the micron scale using the angled etch is extremely challenging due to shadowing of the angled etch.

Regardless of which technique is employed to combine photonic crystal cavities with strain control, further efforts will need be deployed to combine the electrodes used for strain control with those employed for microwave delivery. Single layer fabrication will be insufficient to enable 2 dimensional routing of both layers of electrodes for multiple devices. As a result, multi-layer fabrication of some manner will need to be employed, utilizing either airbridges or oxide cladding of underlying metal-

ized layers. This latter technique is exceptionally difficult to combine with freestanding photonic devices, suggesting that airbridge patterning represents the more straightforward technique for realization of multilayer systems. Alternately, realization of fiber splicing and flip chip technology will enable straightforward integration of these multi-layer electrode structures, as the accuracy requirements for flip chip alignment can be made to be very loose, on the several um scale.

Finally, the tools developed for strain control of color centers can also be applied for nanomechanical photon routing. By tuning the spatial separation of two waveguides the rate of photon exchange between them can be controlled, enabling the creation of tunable on chip photon routers.

From this perspective strain tuning of SiV color centers represents a fascinating technical problem with the potential for a wide variety of applications for quantum technology. The technical barriers to widescale implementation of this technique are substantial, but resolving them would enable the diamond platform to transition from an academic scale technology to a truly industrial one.

4

Quantum network nodes based on diamond qubits

Early experiments implementing diamond photonic crystal cavities were able to show Purcell enhancement of SiV photon emission and emitter dependent cavity reflection spectra, indicating that these cavities were able to enhance interactions between photons and the SiV. Further experiments in bulk

diamond showed that, at sufficiently low temperatures, implementation of microwave drives could enable the SiV to extend its coherence time into the millisecond regime. These experiments suggested that, by integrating these two technologies, the SiV-photonics system could be developed into a functional quantum network node. This would represent an important step towards the creation of a long distance quantum network, and thus realizing the technological benefits that this entails.

In order to be used as a quantum network node the SIV needed to fulfill a long list of requirements, the most challenging of which were coherent spin state control inside a photonic crystal cavity, spin-photon entanglement enabled by the photonic crystal cavity, and a high fidelity interface with an ancillary quantum memory. This last requirement was necessary to enable purification of optically mediated entanglement, which requires the ability to store one entangled state while a second one is created, and is thus dependent on the presence of two coupled quantum memories. Simultaneously realizing all of the above techniques meant implementing not only diamond photonic crystal technology, but also integrating it with microwave coplanar waveguides that would provide the control signal for the SiV spins. Setting aside the nanofabrication challenges that this posed, there were also open questions regarding system heating, reliability, and fidelity that meant there was substantial uncertainty regarding the probability of success of this enterprise, despite the promise indicated in earlier experiments.

The comparatively straightforward success thus represented a substantial step forward for the SiV platform. The microwave CPWs enabled single qubit gates with roughly 99% fidelity, the cavities enabled spin state readout without better than 99.9% fidelity, and dynamical decoupling sequences extending to several mS could be realized without causing thermally induced decoherence. Combining

these properties enabled high fidelity spin-photon entanglement and (by extension) photon storage. In this sense, the "single node" quantum network operations were all demonstrated and performed at high fidelity.

These results also made initial strides in integrating ancillary quantum memories with the SiV in the form of gates with nearby ^{13}C and ^{29}Si atoms. The first are nuclear spins that naturally occur during diamond growth, as naturally a certain fraction of the carbon atoms integrated during growth will be of the higher nuclear weight isotope. The latter atoms can be introduced during implantation to act as the silicon atom that constitutes the defect atom inside the SiV itself. Gates with nearby ^{13}C are well established in the field of NV sensing, where coupling between the NV electron and the nitrogen nucleus is also commonly employed. As such, it was expected that extending these techniques to the SiV would be straightforward.

Unfortunately it emerged that the the SiV, as a spin 1/2 system, struggled to differentiate between different ^{13}C in the environment in a manner that was not observed with the spin 1 NV. As such, the gates between the SiV and these nuclei required lengthy dynamical decoupling sequences that also degraded the fidelity of the interaction. Instead, gates between the SiV and ^{29}Si were explored further. Here, the gates between the various nuclear and electron states could be driven directly using RF and microwave pulses, as stronger interactions between the two spins could realized deterministically. The results relating to the ^{29}Si are exceptionally promising, indicating the possibility of fast, high fidelity gates that can be utilized with essentially any SiV. This would represent the creation of a deterministic, two memory quantum network node that could be utilized for full quantum repeater protocol implementation. The results relating to the ^{29}Si are not yet published elsewhere, and require further

study before final publication.

4.1 Introduction

The realization of quantum networks is one of the central challenges in quantum science and engineering with potential applications to long-distance communication, non-local sensing and metrology, and distributed quantum computing[5,86,87,88,89]. Practical realizations of such networks require individual nodes with the ability to process and store quantum information in multi-qubit registers with long coherence times, and to efficiently interface these registers with optical photons. Cavity quantum electrodynamics (QED) is a promising approach to enhance interactions between atomic quantum memories and photons[90,11,48,16,17]. Trapped atoms in optical cavities are one of the most developed cavity QED platforms for quantum processing, and have demonstrated gates between atoms and photons[91] as well as interactions between multiple qubits mediated by the optical cavity[92]. While these experiments have demonstrated all of the individual components needed for a quantum network, combining them to realize a full-featured node remains an outstanding challenge.

Nanophotonic cavity QED systems with solid-state emitters are appealing candidates for realizing quantum nodes as they can be interfaced with on-chip electronic control and photonic routing, making them suitable for integration into large-scale networks[16,93]. Numerous advances towards the development of such nodes have been made recently. Self-assembled quantum dots in GaAs have been efficiently interfaced with nanophotonic structures, enabling a fast, on-chip spin-photon interface[16,94]. Nitrogen-vacancy color centers in diamond (NVs) have demonstrated multi-qubit quantum

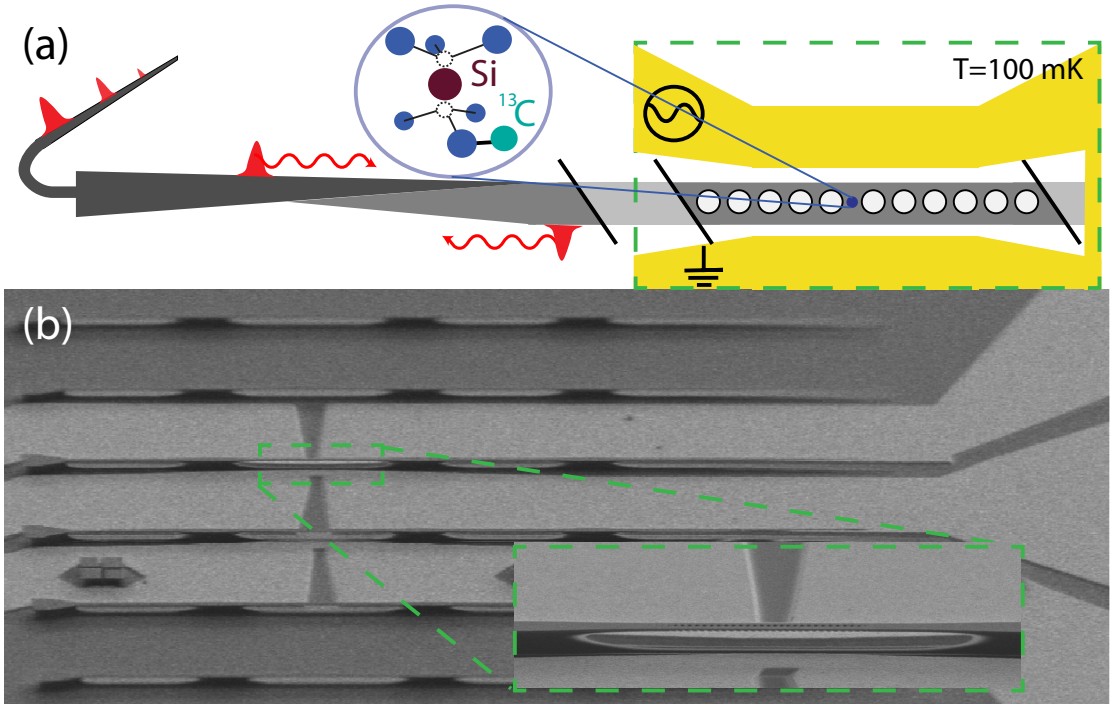


Figure 4.1: (a) Schematic of a SiV-nanophotonic quantum register. A diamond nanostructure with embedded SiV centers and ancillary ^{13}Cnuclei are coupled via a waveguide to a fiber network. Spins are controlled by an on-chip microwave CPW at 0.1 K. (b) Scanning electron micrograph of several devices. The gold CPW is designed to localize microwave fields around the cavity center (green inset).

processors with coherence times approaching one minute[34], and have been used to implement quantum error correction[95] and teleportation[96]. Despite this rapid progress, functional nodes combining all the necessary ingredients in a single device have not yet been realized. For example, quantum memory times in quantum dots are limited to a few μs by the dense bath of surrounding nuclear spins[97]. Conversely, an efficient nanophotonic interface to NVs remains elusive, in part due to the degradation of their optical properties inside nanostructures arising from electrical noise induced by the fabrication[98,99].

In this section, we demonstrate an integrated network node combining all key ingredients required

for a scalable quantum network. This is achieved by coupling a negatively charged silicon-vacancy color-center (SiV) to a diamond nanophotonic cavity and a nearby nuclear spin, illustrated schematically in Figure 4.1(a). The SiV is an optically active point defect in the diamond lattice[26,100]. Its D_{3d} inversion symmetry results in a vanishing electric dipole moment of the ground and excited states, rendering optical transitions insensitive to electric field noise typically present in nanofabricated structures[101,19]. We enhance interactions between SiVs and optical photons by incorporating them into nanocavities, which are critically coupled to on-chip waveguides. Itinerant photons in a fiber network are adiabatically transferred to this waveguide, allowing for the collection of reflected photons with efficiencies exceeding 90%[40]. After an initial optical characterization of the devices, a shorted, gold coplanar waveguide (CPW) is deposited in close proximity to a small subset of cavities [Figure 4.1 (b), inset]. This enables coherent microwave manipulation of the SiV ground state spin in a cryogenic environment ($T < 0.1\,\mathrm{K}$), where phonon-mediated dephasing and relaxation processes are mitigated[102,41,103].

4.2 Spin Readout

In what follows, we characterize these devices in the context of the three key ingredients of a quantum network node: (i) an efficient spin-photon interface, (ii) a long-lived quantum memory, and (iii) access to multiple interacting qubits.

The efficient spin-photon interface is enabled by coupling to a diamond nanophotonic cavity. For critically-coupled cavities, the presence of an SiV modulates the bare nanocavity reflection spectrum

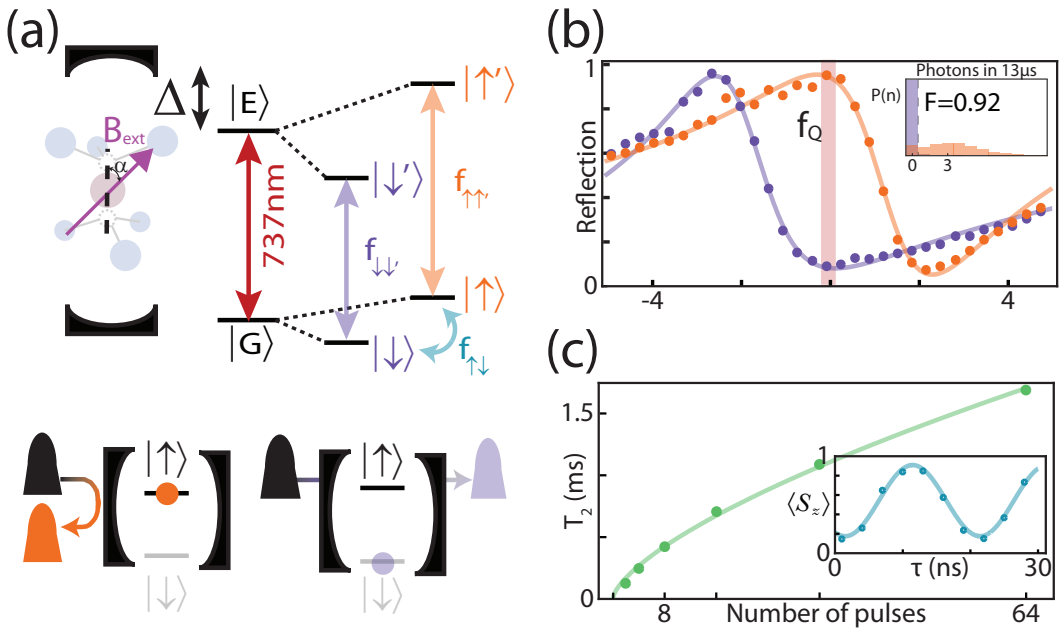


Figure 4.2: (a) Level structure of SiV spin-cavity system. The SiV optical transition at 737 nm is coupled to the nanocavity with detuning Δ. Spin conserving transitions (purple, orange) are split by an external magnetic field (Bext), at an angle α with respect to the SiV symmetry axis. Photons are only reflected by the cavity when the SiV is in state $|\uparrow\rangle$. Microwave fields at frequency $f_{\uparrow\downarrow}$ coherently drive the qubit states. (b) Spin-dependent reflection spectrum for B_{ext} = 0.19T, $\alpha = \pi/2$ at $\Delta = 0.25\kappa$ Probing at the point of maximum contrast (f_Q) results in high-fidelity spin-photon correlations and single-shot readout (inset, F = 0.92). (c) SiV spin coherence time T2(N = 64) > 1.5 ms with dynamical decoupling. (inset) Fast microwave Rabi driving of the SiV spin.

with the strength of this modulation parametrized by the cavity cooperativity $C = 4g^2/(\kappa\gamma) \sim 38$ (with the single photon Rabi frequency, cavity, and atomic energy decay rate $\{g, \kappa, \gamma\} = 2\pi \times \{5.6, 33, 0.1\}$ GHz). For $C > 1$, we expect high-contrast modulation for a small detuning (Δ) between the cavity and the SiV resonance near 737nm. An external field B_{ext} lifts the degeneracy of the SiV spin-$\frac{1}{2}$ sub-levels, creating spin-dependent reflection: photons at the frequency of maximum contrast (f_Q) are reflected from the cavity only when the SiV is in a specific spin state ([Figure 4.2(a)], $|\uparrow\rangle$). In previous works, spin readout of the SiV was performed with B_{ext} parallel to the SiV symmetry axis, where the spin-conserving transitions are highly cycling[41]. The high collection efficiency into a tapered fiber allows for fast single-shot readout of the SiV even in a misaligned field [Figure 4.2(b)], which is necessary for the nuclear spin control described below. We observe a readout fidelity of $F = 0.92$ in 13 μs even when only a few (~ 10) photons are scattered.

4.3 Microwave Control

We next demonstrate that the SiV spin in a nanocavity is a suitable quantum memory. Microwave pulses at $f_{\uparrow\downarrow} = 6.7$ GHz coherently manipulate the SiV spin qubit. The resulting Rabi oscillations, which can be driven in excess of 80 MHz while maintaining acceptable sample temperatures, are shown in the inset of Figure 4.2(c). These rotations are used to probe the coherence properties of the spin via dynamical decoupling sequences [Figure 4.2(c)][104,105]. We measure the coherence time of the SiV inside the nanocavity to be $T_2 > 1.5$ ms and scale with the number of decoupling pulses as $T_2 \propto N^{2/3}$. The coherence scaling observed here differs from that observed in bulk diamond[41], and is similar

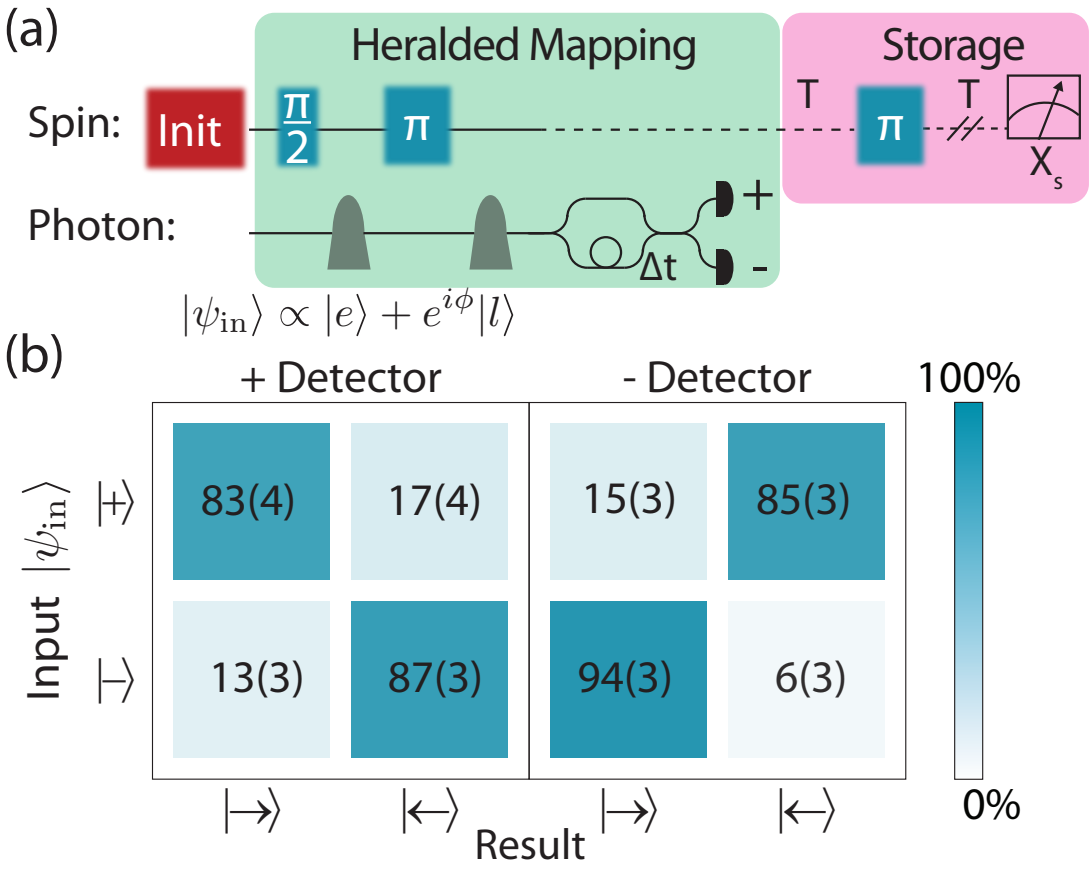


Figure 4.3: (a) Schematic for heralded photon storage. After photonic qubit is reflected off the cavity, an X measurement on the photon heralds successful state transfer which is stored for 2T = 20 μs. (b) Spin-photon storage fidelity. The state $|\pm\rangle = |\downarrow\rangle \pm |\uparrow\rangle$ is mapped onto the SiV, with average fidelity F = 87(6)%.

to NVs near surfaces[106]. This suggests that SiV memory in nanostructures is limited by an electron spin bath, for example residing near the surface of the nanostructure or resulting from implantation-induced damage.

4.4 Spin-photon Interface

We now combine the efficient spin-photon interface and control over the SiV spin state to demonstrate heralded storage of photonic qubit states in the spin-memory, a key feature of a network node[48]. Figure 4.3(a) outlines the experimental scheme, where photonic qubits are prepared using time-bin encoding and mapped onto the SiV spin. In our experiments, the SiV is first initialized into a superposition state $|{\rightarrow}\rangle \propto |{\uparrow}\rangle + |{\downarrow}\rangle$ by optical pumping followed by a microwave $\pi/2$-pulse. A pair of weak coherent pulses separated by $\delta t = 30$ ns at frequency f_Q are then sent to the cavity. The single photon sub-space corresponds to an incoming qubit state $|\Psi_\mathrm{i}\rangle \propto \beta_e |e\rangle + \beta_l |l\rangle$, where $|e\rangle$ ($|l\rangle$) denotes the presence of a photon in the early (late) time-bin. As a photon can only be reflected from the device if the SiV is in state $|{\uparrow}\rangle$ [Figure 4.3(a)], particular components of the initial product state can be effectively "carved out"[92]. We invert the SiV spin with a π-pulse between the arrival of the two time bins at the cavity, such that a photon detection event indicates that the final state has no $|e\uparrow\rangle$ or $|l\downarrow\rangle$ component. This leaves the system in the final spin-photon entangled state $|\Psi_\mathrm{f}\rangle \propto \beta_e |e\downarrow\rangle + \beta_l |l\uparrow\rangle$.

The reflected photon enters a time-delay interferometer, where one arm passes through a delay line of length δt, allowing the two time-bins to interfere and erase which-time-bin information. As can be seen by expressing the final state in the corresponding photon basis:

$$|\psi\rangle_\mathrm{f} \propto |+\rangle (\beta_e |{\downarrow}\rangle + \beta_l |{\uparrow}\rangle) + |-\rangle (\beta_e |{\downarrow}\rangle - \beta_l |{\uparrow}\rangle), \tag{4.1}$$

a detection event on either the '+' or '−' arm of the interferometer represents a measurement in the

X-basis ($|\pm\rangle \propto |e\rangle \pm |l\rangle$), effectively teleporting the initial photonic state onto the electron (up to a known local rotation). We experimentally verify generation of the entangled state $|\psi\rangle_{\mathrm{f}}$ for input states $|\psi\rangle_{\mathrm{i}} = |\pm\rangle$ by measuring spin-photon correlations, and use it to extract a teleportation fidelity of $0.92(6)$.

After detection of the heralding photon, we store the teleported photonic states (initially prepared in $\{|+\rangle$ or $|-\rangle\}$) in spin memory for $20\,\mu\mathrm{s}$ by applying an additional decoupling π-pulse on the SiV spin. The overall fidelity of teleportation and storage is $F = 0.87(6)$ after corrected for readout errors [Figure 4.3(b)]. The quantum storage time can be extended by additional decoupling sequences [Figure 4.3(c)], enabling entanglement distribution up to a T_2-limited range of $500\,\mathrm{km}$.

4.5 SiV Electron to Nuclear Spin Interface

In order to extend this range and to enable more generic quantum communication protocols, we next demonstrate a two-qubit register based on the cavity coupled SiV electronic spin and a nearby ^{13}C nuclear memory. The ^{13}C isotope of carbon is a spin-$\frac{1}{2}$ nucleus which has $\sim 1\%$ natural abundance in diamond, and is known to exhibit exceptional coherence times[34]. While direct radio-frequency manipulation of nuclear spins is impractical due to heating concerns, control over ^{13}C spins can be achieved by adapting electron mediated techniques developed for Nitrogen vacancy (NV) centers[107,1,108,33]. The physical principle of the SiV-^{13}C interaction is depicted in Figure 4.4(a). The SiV generates a spin-dependent magnetic field $\mathbf{B}_{\mathrm{SiV}}$ at the position of the ^{13}C, which is located a few lattice sites away.

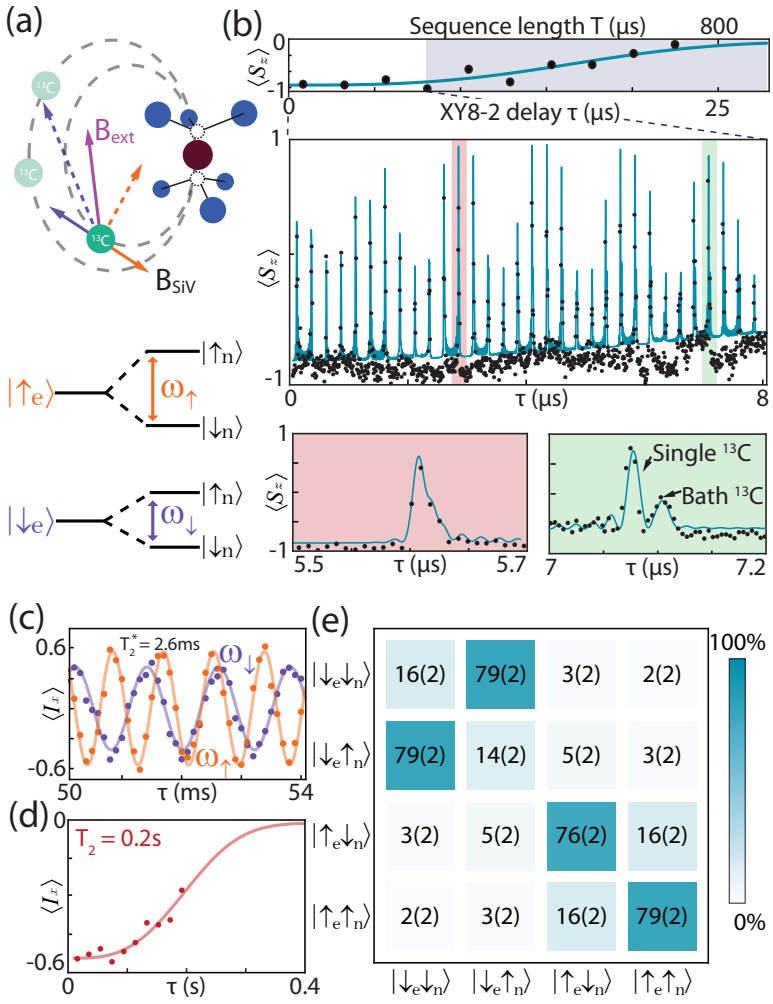


Figure 4.4: (a) Schematic of an SiV coupled to nearby ^{13}Cnuclear spins. Orange (purple) vectors are conditional fields when the SiV is in state $|\uparrow\rangle$ ($|\downarrow\rangle$). (b) XY8-2 spin-echo. (Top) envelope for spin-echo shows a $T_2(N = 16) = 603$ μs. XY8-2 at early times (Center) exhibits collapses in signal due to interaction with nuclear spins. Single ^{13}C cannot be identified at early times (red inset), but separate from the bath at long times (green inset). (c) Ramsey measurement on the ^{13}C nuclear spin. The nuclear spin precesses at a different Larmor frequency depending on whether the SiV is prepared in $|\uparrow\rangle$ (orange) or $|\downarrow\rangle$ (purple). Coherent oscillations persist for $T_2 > 2$ ms. (d) Spin echo on ^{13}C, revealing $T_2 > 0.2$ s (e) Reconstructed amplitudes for a CNOT gate transfer matrix.

This is described by a hyperfine interaction Hamiltonian:

$$\hat{H}_{\mathrm{HF}} = \hbar A_{\parallel} \frac{\hat{S}_z}{2} \frac{\hat{I}_z}{2} + \hbar A_{\perp} \frac{\hat{S}_z}{2} \frac{\hat{I}_x}{2} \tag{4.2}$$

where $\hat{S}_{z,x}$ ($\hat{I}_{z,x}$) are the Pauli operators for the electron (nuclear) spin, and $A_{\parallel,\perp}$ are the coupling parameters related to the parallel and perpendicular components of B_{SiV} with respect to the bias field B_{ext} [109,1,108]. Hyperfine interactions manifest themselves in spin-echo measurements as periodic resonances[108], shown in Fig. 4.4 for an XY8-2 decoupling sequence $\pi/2 - (\tau - \pi - \tau)^{16} - \pi/2$, where τ is the free evolution time. The coherence envelope for this sequence is $T_2(N = 16) = 603\,\mu\mathrm{s}$ [Figure 4.4(b), upper panel].

For weakly coupled ^{13}C ($A_{\perp} \ll \omega_l$, and $A_{\parallel} \ll \omega_l$, as used in this letter), the positions of the resonances[108]

$$\tau_k \approx \frac{2k+1}{2\omega_l} \left(1 - \frac{1}{2} \left(\frac{A_{\perp}}{2\omega_l} \right)^2 \right), \tag{4.3}$$

where ω_l is the larmor frequancy of a bare ^{13}C, are insensitive to specific ^{13}C hyperfine parameters at first order, rendering them indistinguishable at early times ($\tau_k \ll 4\,\mu\mathrm{s}$, [Figure 4.4(b), red inset]). Individual ^{13}C can be isolated at longer times[108], and are used to engineer gates between a single ^{13}C and the SiV [Figure 4.4(b), green inset] *. The fundamental two-qubit gate associated with such interaction is a conditional $\pm\pi/2$ rotation of the ^{13}C-spin around the X axis ($R_x^{\pm\pi/2}$), which is a maximally entangling gate. Together with unconditional rotations of the nuclear spin (which are also generated

*This is in contrast with the NV center, which is a spin-1 system and therefore features a linear shift of the resonances with coupling strength $A_{\parallel}$ in the $S = \{0, -1\}$ sub-system.

via dynamical decoupling sequences), and MW rotations on the SiV, these sequences form a universal set of gates for the register[108].

We characterize the ^{13}C via Ramsey spectroscopy [Figure 4.4(c)]. The nuclear spin is initialized and read out via the optically addressable SiV spin by transferring population between the SiV and ^{13}C. Depending on the SiV state before the Ramsey sequence, we observe oscillations of the nuclear spin at its eigenfrequencies $\omega^2_{\uparrow,\downarrow} = \left(\omega_l \pm A_\parallel/2\right)^2 + (A_\perp/2)^2$), allowing us to determine the hyperfine parameters $\{\omega_l, A_\parallel, A_\perp\} = 2\pi\{2.0, 0.70, -0.35\}$MHz. This coherence persists for $T_2^* > 2\,\mathrm{ms}$, and can be further extended to $T_2 > 0.2\,\mathrm{s}$ by applying a single dynamical decoupling π-pulse on the nucleus, demonstrating the exceptional memory of the ^{13}C nuclear spin [Figure 4.4(d)].

4.6 CNOT gates and Bell State Formation

We benchmark the two-qubit register by demonstrating an SiV-controlled X-gate (CNOT) on the ^{13}C-spin by combining a $R_x \pm \pi/2$ with an unconditional nuclear $\pi/2$ rotation. This gate results in a spin flip of the ^{13}C only if the SiV spin is in the state $|\downarrow\rangle$ [Figure 4.4(e)]. We use this gate to prepare a Bell state by initializing the register in $|\downarrow\downarrow\rangle$, and applying a $\pi/2$-rotation gate on the SiV spin followed by a CNOT gate. Correlation measurements yield a concurrence of $\mathcal{C} = 0.22(9)$ corresponding to a Bell state fidelity of $F = 0.59(4)$ after correcting for readout errors.

4.7 Limitations of the SiV - ^{13}C Gate

Our experiments demonstrate the first prototype of a nanophotonic quantum network node combining all necessary ingredients in a single physical system. We emphasize that both spin-photon and spin-spin experiments are performed in the same device under identical conditions (cavity detuning and bias field), thereby providing simultaneous demonstration of all key requirements for a network node.

The main limitation on the demonstrated fidelities are related to the specific ^{13}C in the proximity of the SiV, requiring an unfavorable alignment of the external magnetic field in order to isolate a single ^{13}C. Specifically, the fidelity of two-qubit gates is limited by residual coupling to bath nuclei, SiV decoherence during the gate operations, and under/over-rotations of the nuclear spin arising from the granularity of spin-echo sequences. To reduce these errors, fine-tuned adaptive pulse sequences can be used to enhance sensitivity to specific nearby ^{13}C, and tailor the rotation angle and axis of rotation [110,111]. Alternatively, replacing gold with superconducting microwave coplanar waveguides will significantly reduce ohmic heating, and allow direct radio-frequency control of nuclear spins.

4.8 SiV-^{29}Si Gates

Here we present early results from the experimental realization of a deterministic spin register between a single SiV color center and its constituent silicon 29 nuclear spin inside a nanophotonic device. This spin register can be created on demand through selective implantation of silicon 29 during device fabrication, and demonstrates high fidelity (greater than 95%) operation at high speeds (swap gate times

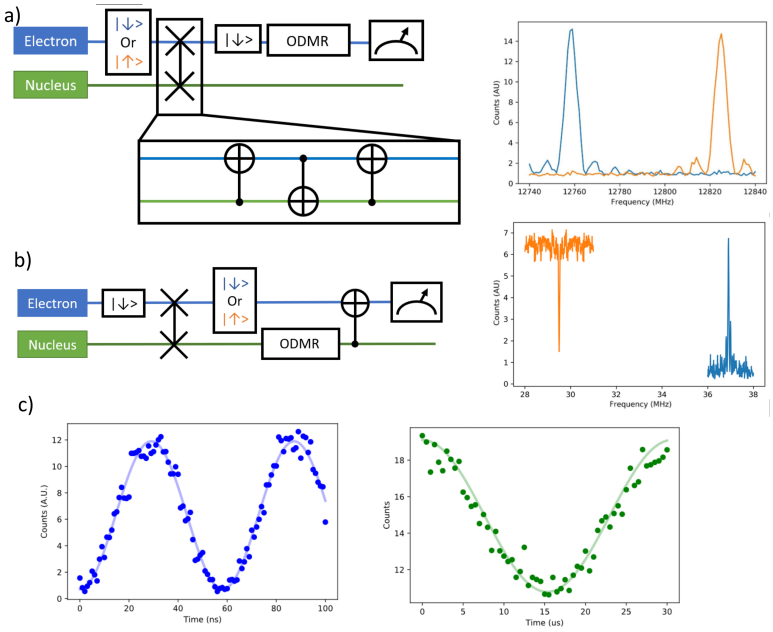


Figure 4.5: Initial results probing the nuclear to electron spin interface for the SiV-^{29}Si system. a) Left: experimental sequence for probing the electron spin properties. The 2 qubits register is initialized using a swap gate before ODMR is performed. Right: the the electron spin ODMR after initializing the nucleus in the up(down) state is in orange (purple). b) Experimental sequence for probing the ^{29}Si spin. After initializing the 2 qubit system the electron is reinitialized in the up (down) state yielding a nuclar spin transition shown in orange (blue). c) Rabi drive for drive applied to one of the electron (left) and nuclear (right) transitions, giving pi times of 25 ns and 16 uS respectively.

of 15 μS).

Under application of an aligned external magnetic field, the ground state properties of the two qubit register are governed by the interaction Hamiltonian between the ^{29}Si and the SiV electron spin states:

$$H = \vec{S} \cdot A \cdot \vec{I} + g\mu_B \vec{B} \cdot \vec{S} + \gamma_n \vec{B} \cdot \vec{I}$$

Where A is the hyperfine structure constant, $\vec{S}$ is the electon spin vector, and $\vec{I}$ is the nuclear spin

vector. Subject to appropriate strain and magnetic field conditions, each of the transitions described by this Hamiltonian can be directly driven using microwave or RF tones, allowing for coherent control of the 2 qubit register. Optical initialization and readout of the SiV electron state is facilitated through the use of nanophotonic crystal cavities into which individual ^{29}Si ions are implanted. We extract these properties of our two qubit register using the following experimental sequence. First, the electron spin is prepared in a well defined spin state through optical preselection on the cavity reflection spectra. This state is then transferred onto the nuclear spin using a swap gate consisting of alternating controlled π (cpi) pulses on the electron and nuclear spin transitions. Subsequent optical reinitialization of the electron spin completes the initialization of our two qubit spin register, which is followed by the desired experimental sequence (Figure 4.5 a and b, left). Nuclear state readout is accomplished through application of a cpi pulse to one of the two electron spin states. Using this scheme, optical detection of magnetic resonances (ODMR) can be used to extract the hyperfine splitting and linewidths of both the electron (Figure 4.5a, right) and nuclear (Figure 4.5b right) states. Next, we explore the coherence of readout and control operations on the components of this spin register. We use the same experimental sequence displayed in figure 4.5a, but now apply Rabi drives to each of the different spin transitions in turn before reading out the final state of both the electron and the nuclear states. Using this sequence gate times can be extracted from the Rabi oscillations of each of the qubits, giving pi times of 15 uS for the nuclear spin (Figure 4.5c, right) and 25 nS for the electron(Figure 4.5c, left). Experiments establishing the maximum fidelity of these gates are still ongoing, but early results suggests fidelities of greater than 95% can be realized in a straightforward manner.

4.9 Conclusion and Outlook

In conjunction with recent advances in controlling emitter inhomogeneity via electromechanical tuning[112], these techniques should allow for chip-scale fabrication of quantum network nodes, laying the groundwork for the realization of scalable quantum repeater[10,86] architectures. Further development of the ^{29}Si nucleus as an ancillary quantum memory for SiV network nodes could further extend the utility of the SiV-nanophotonics platform to enable full implementation of these protocols, subject to further study of the coherence properties of entangled states generated using these memories. The ability to store quantum information in highly coherent ^{13}C nuclei, as well as the opportunity to extend these results to other group-IV color-centers, may open up the possibility of operating such nodes at at temperatures > 1 K[113,114,115,116]. Finally, the efficient quantum network node demonstrated in this section could enable generation of multi-dimensional cluster states of many photons, which could facilitate realization of novel, ultra-fast one-way quantum communication architectures[117].

5

An Integrated Nanophotonic Quantum Register in Diamond

During development of the technology for the SiV quantum network node, a number of new scientific observations were made that offered insights into both the specifics of SiV diamond technology and the general challenges associated with the implementation of quantum networking protocols. This

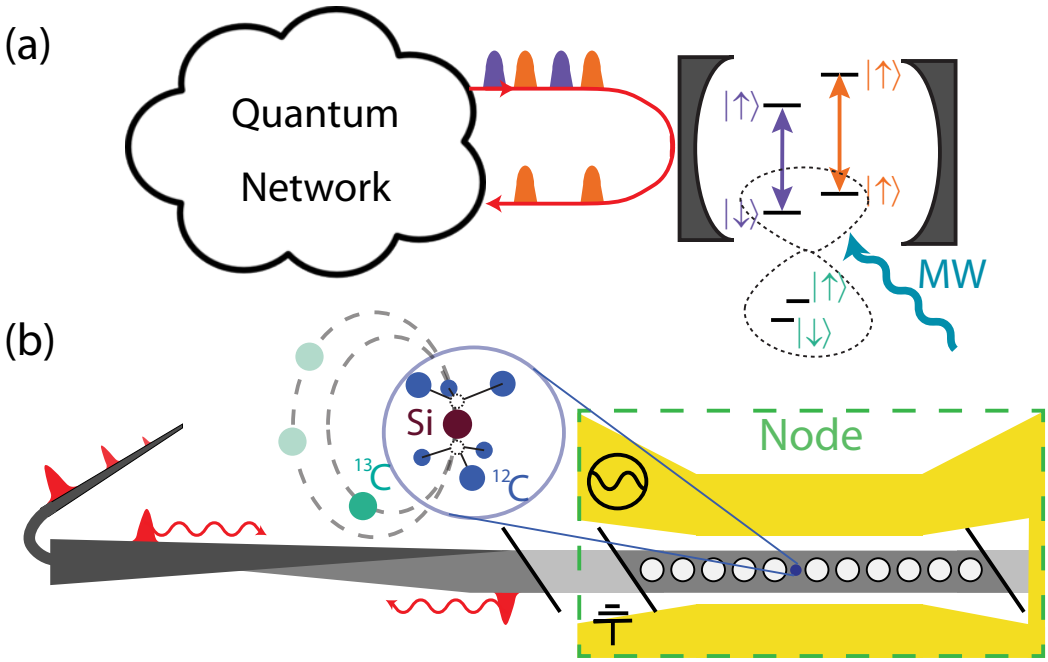


Figure 5.1: (a) Schematic of a quantum network. Nodes consisting of several qubits are coupled together via an optical interface. (b) A quantum network node based on the SiV. SiV centers and ancilla ^{13}C are incorporated into a nanophotonic device and addressed with a coupled fiber and microwave coplanar waveguide.

section serves to document some of these results. In particular, the details of the SiV strain, microwave, and magnetic field responses are covered in detail, with special emphasis on how these fields combine to change the SiV properties. A detailed study of the noise environment effecting SiV is presented, which in the context of dynamical decoupling sequences leads naturally into a study of the SiV-^{13}Cgates. Finally, details related to the design and noise properties of the SiV-nanophotonic system and the resulting decoherence are presented.

5.1 Introduction

Quantum networks have the potential to enable a plethora of new technologies including secure communication, enhanced metrology, and distributed quantum computing[5,86,87,88,89]. Such networks require nodes which perform quantum processing on a small register of interconnected qubits with long coherence times. Distant nodes are connected by efficiently interfacing qubits with optical photons that can be coupled into an optical fiber [Fig. 5.1(a)].

The prevailing strategy for engineering an efficient, coherent optical interface is that of cavity quantum electrodynamics (QED), which enhances the interactions between atomic quantum memories and photons[118,11,48,16,17]. Nanophotonic cavity QED systems are particularly appealing, as the tight confinement of light inside optical nanostructures enables strong, high-bandwidth qubit-photon interactions[119,120,19]. In practice, nanophotonic devices also have a number of technological advantages over macroscopic optical cavities, as they can be fabricated en-masse and interfaced with on-chip electronics and photonics, making them suitable for scaling up to large-scale networks[16,93]. While strong interactions between single qubits and optical photons have been demonstrated in a number of cavity QED platforms[16,94,33,95,96,17], no single realization currently meets all of the requirements of a quantum network node. Simultaneously achieving high-fidelity, coherent control of multiple long-lived qubits inside of a photonic structure is a major outstanding challenge.

Recent work has established the silicon-vacancy color-center in diamond (SiV) as a promising candidate for quantum networking applications[121,41,122,70,76,113]. The SiV is an optically active point defect in the diamond lattice[26,100]. Its D_{3d} inversion symmetry results in a vanishing permanent electric

dipole moment of the ground and excited states, rendering the transition insensitive to electric field noise typically present in nanostructures[68]. Recent work has independently shown that SiV centers in nanostructures display strong interactions with single photons[70] and that SiV centers at temperatures below 100 mK (achievable in dilution refrigerators) exhibit long coherence times[102,41]. While these results indicate the promising potential of the SiV center for future quantum network nodes, significant technical challenges must be overcome in order to combine these ingredients.

In this paper, we outline the practical considerations and approaches needed to build a quantum network node with SiV centers in nanophotonic diamond cavities coupled to ancillary nuclear spins [Fig. 5.1(b)][22]. Section 5.2 describes recent improvements to the fabrication techniques used to create and incorporate SiV centers into high-quality factor, critically-coupled nanophotonic cavities with an efficient fiber-optical interface. Section 5.3 describes the millikelvin experimental apparatus and several common experimental protocols. Section 5.4 describes the SiV level structure and electronic transitions, illusutrating the interplay of strain and magnetic field in enabling both coherent control of– and a photonic interface for– SiV spins. Sections 5.5, 5.6 and 5.7 outline experimental implementations of optical and microwave control of SiV centers, and use this control to create electron-photon Bell states with high fidelity in section 5.8. Section 5.9 introduces techniques for coupling to additional qubits consisting of naturally occuring ^{13}C in diamond. We describe our method for initializing and reading out these nuclear spins via the SiV, coherent control of ^{13}C with microwave and radio-frequency driving, probe the coherence of these nuclei, and finally entangle the SiV with a nearby ^{13}C and demonstrate electron-nuclear Bell states.

5.2 Nanophotonic device fabrication

5.2.1 Device design

The devices used in these experiments integrate nanophotonic cavities, implanted SiV centers, and microwave coplanar waveguides onto a single diamond chip. Here we present the fabrication process used to realize such devices.

Typically, high-quality photonic crystal resonators are fabricated from 2-D membranes, which tightly confine light due to total internal reflection off of material boundaries. Difficulties in growing high-purity, single-crystal diamond films on non-diamond substrates are one of the key challenges to fabricating such resonators in diamond[123]. As a result, nanophotonic diamond structures must be etched out of bulk diamond, which requires non-traditional etching techniques[84,29]. In particular, two methods have emerged for creating freestanding diamond nanostructures: Isotropic undercutting[29,124] and angled ion-beam etching (IBE)[65]. In this work, we use the latter technique, resulting in freestanding, triangular-cross-section waveguides.

Preliminary design of the nanophotonic structures are described in a later section, and are optimized to maximize atom-photon interaction while maintaining high waveguide coupling. To take advantage of the scalable nature of nanofabrication, these optimized devices are patterned in sets of roughly 100 with slightly modified fabrication parameters. The overall scale of all photonic crystal cavity parameters are varied between different devices on the same diamond chip to compensate for fabrication errors (which lead to unexpected variations in the resonator frequency and quality-factor).

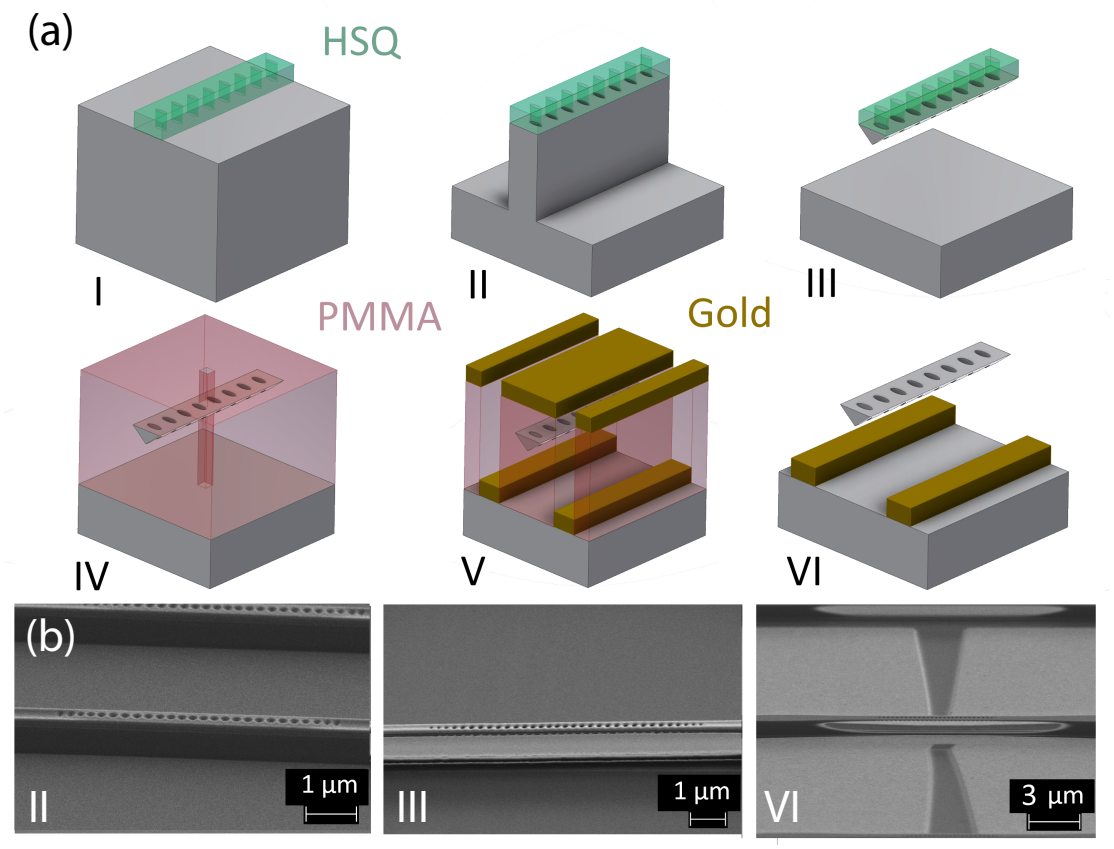


Figure 5.2: (a) Schematic of the nanofabricataion process used to produce devices. I: Titanium-HSQ mask is patterned using EBL. II: Pattern is transferred onto diamond using top down O_2 RIE. III: Angled IBE is used to separate structures from substrate. IV: Devices are covered in PMMA and implantation aperatures are formed using EBL. Device are then cleaned, implanted, and annealed. V: PMMA is used in a litoff procedure to pattern gold microwave striplines. VI: Final devices are cleaned and prepared for experiment. (b) Scanning electron micrographs corresponding to steps II, III, and VI in the fabricaton procedure.

Due to these errors, roughly one in six cavities are suitable for SiV experiments. Fortunately, hundreds of devices are made in a single fabrication run, ensuring that every run yields many usable devices.

The diamond waveguide region (as opposed to the photonic crystal cavity region) has two distinguishing features. First, thin support structures are placed periodically along the waveguide and are used to suspend the structures above the substrate. These supports are portions of the waveguide which are adiabatically tapered to be $\sim 30\%$ wider than the rest of the waveguide, and take longer to etch away during the angled etch process. By terminating the etch after normal waveguide regions are fully etched through, these wide sections become $\sim 10\,\mathrm{nm}$ thick supports which tether the waveguide structures to the substrate while minimizing scattered loss from guided modes. Second, one end of the waveguide structure is adiabatically tapered into free-space[40]. These tapers are formed by a linear taper of the waveguide down to less than $50\,\mathrm{nm}$ wide over a $10\,\mu\mathrm{m}$ length. This tapered region can be coupled to a similarly tapered optical fiber, allowing structures to efficiently interface with a fiber network [Sec. 5.3]. This tapered end of the waveguide is the most fragile portion of the structure, and can break after repeated fiber coupling attempts. This is often what limits the total measurement lifetime of a device.

The number of devices (and thus the relative yield of the fabrication process) is limited by the maximum packing density on the diamond chip. This is primarily limited by the need to accommodate $10\,\mu\mathrm{m}$ wide microwave coplanar waveguides (CPWs) between devices, which are patterned directly onto the diamond surface to efficiently control SiV spins using microwaves. Simulations (Sonnet Inc) of prospective design geometries ensure that the CPW is impedance matched with our $50\,\Omega$ feed lines, which minimizes scattered power from the waveguides. Tapers in the CPW near the center of the cav-

ity regions concentrate current and increase the amplitude of the microwave field near the SiVs, and CPWs are terminated with a short in order to ensure a magnetic field maximum along the device.

5.2.2 Device fabrication

Fabrication of the diamond structures proceeds as described in ref.[40] with the notable modification that the angled etch is conducted not with a Faraday cage loaded inside a reactive ion etching chamber, but instead with an IBE. The Faraday cage technique[84,21] offered the benefit of simplicity and accessibility—requiring only that the reactive ion etching chamber in question was large enough to accommodate the cage structure—but suffered from large fluctuations in etch rate across the surface of the sample, as well as between different fabrication runs, due to imperfections in the Faraday cage mesh. These irregularities could be partially compensated for by repeatedly repositioning and rotating the cage with respect to sample during the etch, but this process proved to be laborious and imprecise. Instead, IBE offers collimated beams of ions several cm in diameter, leading to almost uniform etch rates across the several mm diamond chip. This technique allowed for consistent fabrication of cavities with $Q > 10^4$, $V < 0.6[\lambda/(n = 2.4)]^3$, and resonances within $\sim 10\,\mathrm{nm}$ of SiV optical frequencies.

Once the diamond cavities are fabricated [Fig. 5.2(a I-III)], SiV centers must be incorporated. To ensure the best possible atom-photon interaction rate [Sec. 5.5], SiVs should be positioned at the cavity mode maximum. Ideally, this requires implantation accuracy of better than $50\,\mathrm{nm}$ in all 3 dimensions due to the small mode volume ($\sim 0.5[\lambda/(n = 2.4)]^3$) of the cavities used. In the past, implantation of silicon ions (which form SiV centers following a high-temperature anneal) was done using focused ion-beam implantation, but this technique required specialized tools and lacked the accuracy neces-

sary for maximally efficient mode coupling[19]. Instead, we adapt the standard masked implantation technique and use commercial foundaries for ion implantation.

For the implantation process, we repeatedly spin and bake MMA EL11 and PMMA C4 (Microchem) to cover the nanophotonic cavities completely with polymer resist. We then spin-coat a conductive surface layer of Espacer (Showa Denko). An E-beam lithography (EBL) tool then aligns with large markers underneath the polymer layer, allowing it to expose an area surrounding smaller, high-resolution alignment markers on the diamond. The exposed regions are developed in a 1:3 mixture of MIBK:IPA. Espacer is again spin-coated, and a second EBL write can be done, aligned to the high-resolution markers. Based on these alignment markers, holes of less than 65 nm diameter (limited by the resolution of PMMA resist) are patterned onto the center of the photonic crystal cavity which, after subsequent development, act as narrow apertures to the diamond surface [Fig. 5.2(a IV)]. The rest of the diamond surface is still covered in sufficiently thick PMMA to prevent ions from reaching masked portions of the device. Diamonds are then sent to a commercial foundry (Innovion) where they are implanted with silicon ions at the appropriate energy and dose [Fig. 5.2 (b)]. Annealing in a UHV vacuum furnace (Kurt-Lesker) at $\sim$1400 K converts these implanted ions into SiV centers[125,68].

CPWs are fabricated using a liftoff process similar to that used to create masked implantation windows. The most notable difference is an additional oxygen plasma descum after development to remove PMMA residue from the surface. Following development, a 10 nm titanium film serves as an adhesion layer for a 250 nm thick gold CPW [Fig. 5.2 (a V)]. Liftoff is performed in heated Remover PG (Microchem) [Fig. 5.2 (a VI)]. The metal thicknesses used here are chosen to improve adhesion of the gold, as well as prevent absorption of cavity photons by the metallic CPW. We observe that the

cavity quality factor significantly degrades with gold films $> 300\,\mathrm{nm}$. Due to ohmic heating, which can degrade the coherence properties of SiV spins [Sec. 5.6], the length of the CPW is constrained to address a maximum of roughly 6 devices.

Future improvements in diamond device performance will be predicated on improvements of the fabrication technology. Device quality factors are currently limited by deviations in device cross section caused by imperfect selectivity of the HSQ hard mask to oxygen etching. Replacing this mask with a sufficiently smooth metal mask could result in improved etch selectivity and device performance. Isotropic undercut etching could also lead to improved control over device cross sections and facilitate more sophisticated device geometries[124,61] at the cost of reduced control over isotropically etched surface roughness. Various techniques exist for the formation of smaller implantation apertures[77,126], but these techniques are difficult to use in conjunction with implantation into completed nanophotonic devices. Finally, the use of superconducting striplines could reduce heating, which would enable the CPW to potentially address all devices on the diamond chip and allow for faster driving of SiV spin and nuclear transitions [Sec. 5.6, 5.9].

5.3 Experimental Setup

Experiments are performed in a home-built photonic-probe setup inside of a dilution refrigerator (DR, BlueFors BF-LD250) [Fig. 5.3(a)]. The diamond substrate is mounted to a gold-plated copper sample holder via indium soldering below the mixing chamber in the bore of a (6,1,1) T superconducting vector magnet (American Magnetics Inc.) anchored to the 4 K stage. A thermal link between the device

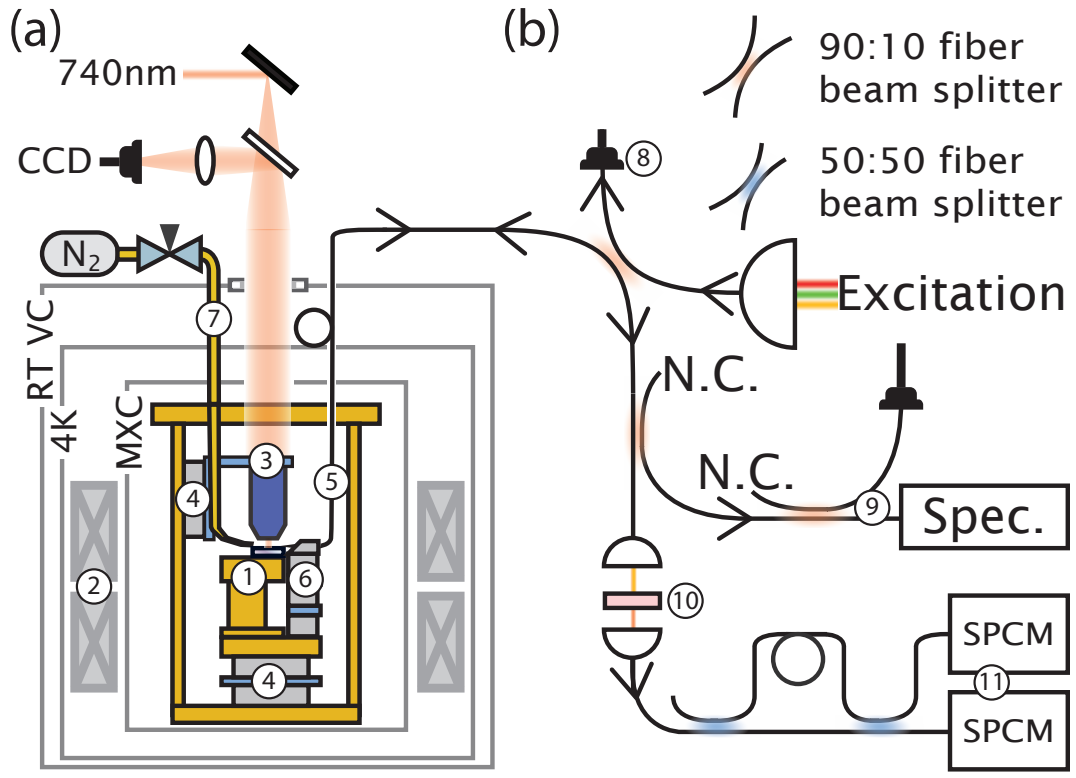


Figure 5.3: (a) Experiment schematic. Devices 1 are mounted in the bore of a SC magnet 2 inside of a dilution refrigerator, and imaged with wide-field imaging 3 and piezo steppers 4 . Devices are addressed with a tapered optical fiber 5 positioned using a second set of piezo steppers 6 . Cavities are tuned using a nitrogen 7 . (b) Fiber network used to probe devices. Excitation light is monitored 8 and sent to the device. Collected light is monitored 9 and filtered 10 then sent to one or several SPCMs 11 . N.C. indicates no connection.

and the mixing chamber plate is provided by gold-plated copper bars, as well as oxygen-free copper braids (Copper Braid Products), ensuring maximal thermal conductivity between the mixing chamber plate and the sample, which reaches a base temperature of roughly 60 mK. We address single nanophotonic devices via a tapered optical fiber, which can be coupled *in-situ* with collection efficiencies exceeding 90% [40]. The tapered fiber is mounted to a 3-axis piezo stepper (ANPx101, ANPz101), and imaged in free-space by an $8f$ wide-field scanning confocal microscope which focuses onto a cryo-compatible objective (Attocube LT-APO-VISIR). This setup allows for coupling to several cavities during a single cooldown.

Once coupled, the cavity resonance is red-shifted via nitrogen gas condensation [70]. A copper tube is weakly thermalized with the 4 K plate of the DR and can be heated above 80 K in order to flow N_2 gas onto the devices. This gas condenses onto the photonic crystal, modifying its refractive index and red-shifting the cavity resonance. When the copper tube is not heated, it thermalizes to 4 K, reducing the blackbody load on the sample and preventing undesired gas from leaking into the vacuum chamber.

After red-tuning all devices in this way, each cavity can be individually blue-tuned by illuminating the device with a $\sim$100 μW broadband laser via the tapered fiber, locally heating the device and evaporating nitrogen. This laser-tuning can be performed very slowly to set the cavity resonance with a few GHz. The cavity tuning range exceeds 10 nm without significantly degrading the cavity quality factor, and is remarkably stable inside the DR, with no observable drift over several months of measurements.

In previous work [70], SiVs were probed in transmission via the free-space confocal microscope focused onto a notch opposing the tapered fiber. Mechanical vibrations arising from the DR pulse tube ($\sim$1 μm pointing error at the sample position) result in significant fluctuations in power and polar-

ization of incoupled light. In this work, we demonstrate a fully integrated solution by utilizing the same tapered fiber to both probe the device and collect reflected photons. This approach stabilizes the excitation path and improves the efficiency of the atom-photon interface, allowing for deterministic interactions with single itinerant photons. High-contrast reflection measurements are enabled by the high-cooperativity, critically-coupled atom-cavity system. Resonant light is sent via the fiber network [Fig. 5.3(b)] and reflected off of the target device. We pick off a small fraction ($\sim 10\%$) of this signal and use it to monitor the wide-band reflection spectrum on a spectrometer (Horiba iHR-550) as well as calibrate the coupling efficiency to the nanocavity. The remaining reflection is then routed either directly to a single-photon counting module (SPCM, Excelitas SPCM-NIR), or into a time-delay interferometer for use in spin-photon experiments [Sec. 5.8]. Due to this high-efficiency fiber-coupled network, we observe overall collection efficiencies of $\sim 40\%$, limited by the quantum efficiency of our APDs.

5.4 Optimal strain regimes for SiV spin-photon experiments

Similar to other solid state emitters[127,128], the SiV is sensitive to local inhomogeneity in the host crystal. In the case of the SiV, which has D_{3d} symmetry, the dominant perturbation is crystal strain. In this section, we describe the effects of strain on the SiV spin and optical properties, and how they can enable efficient microwave and optical control of SiV centers inside nanostructures.

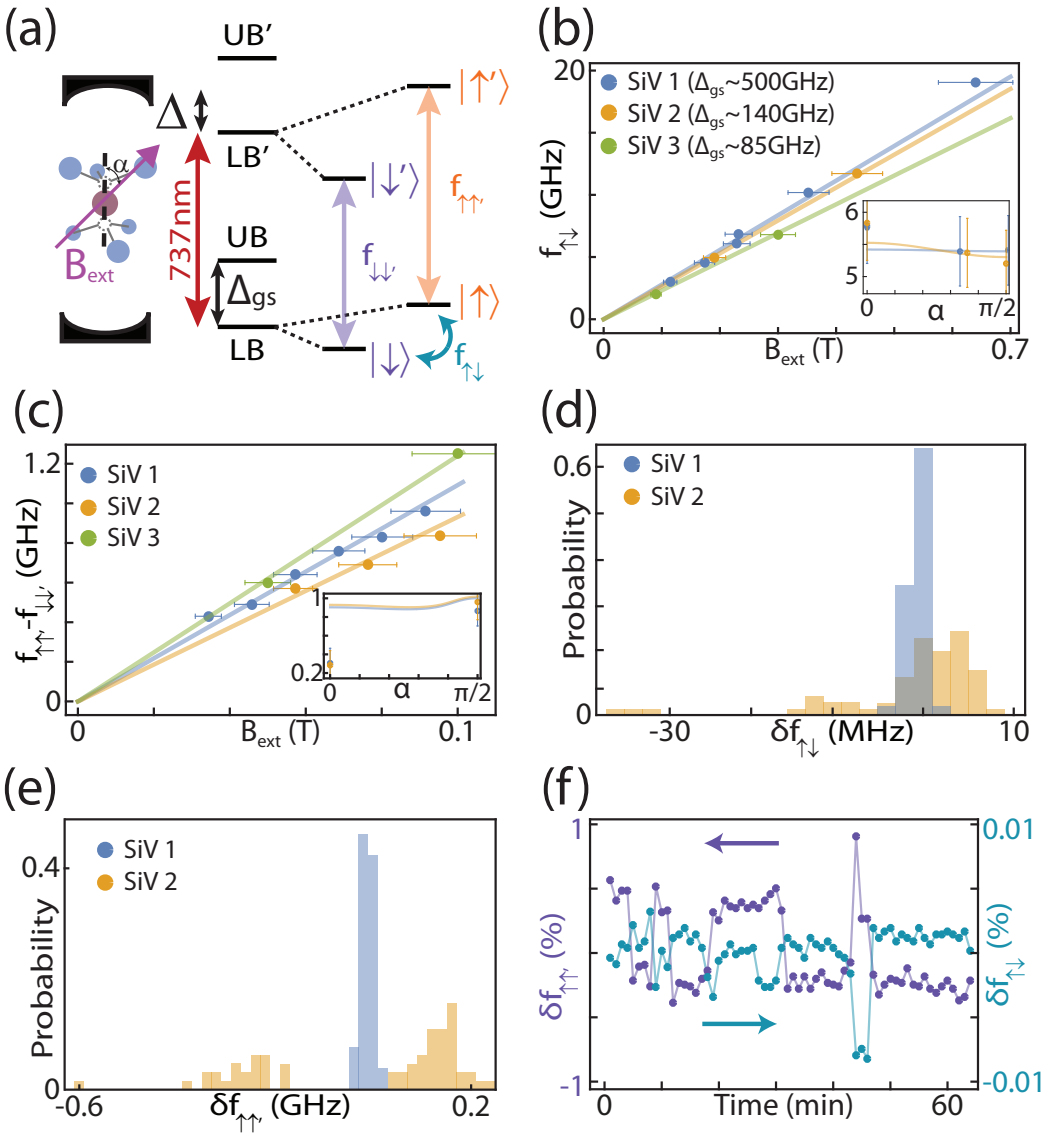


Figure 5.4: (a) SiV level diagram. Optical transitions $f_{\uparrow\uparrow'}, f_{\downarrow\downarrow'}$ $\sim 737\,\mathrm{nm}$ are coupled to a nanophotonic cavity with mean detuning Δ. Microwaves at frequency $f_{\uparrow\downarrow}$ drive rotations in the lower branch (LB). (b) Qubit frequency $f_{\uparrow\downarrow}$ for differently strained emitters. Modeled splitting for ground state g-factors $\mathrm{g_{gs1}} = 1.99, \mathrm{g_{gs2}} = 1.89, \mathrm{g_{gs3}} = 1.65$ (solid lines) based on independent measurements of Δ_{gs}. (inset) Angle dependence of $f_{\uparrow\downarrow}$ at fixed field $B_{\mathrm{ext}} = 0.19\,\mathrm{T}$. Solid lines are predictions using the same model parameters. (c) Optical splitting $f_{\uparrow\uparrow'} - f_{\downarrow\downarrow'}$. Fits extract excited state g-factors $\mathrm{g_{es1}} = 1.97, \mathrm{g_{es2}} = 1.83, \mathrm{g_{es3}} = 1.62$ (solid lines). (inset) Angle dependence of $f_{\uparrow\uparrow'} - f_{\downarrow\downarrow'}$ at fixed field $B_{\mathrm{ext}} = 0.1\,\mathrm{T}$. (d) Histogram of MW transition frequency for two different emitters. (e) Histogram of Optical transition frequency for two different emitters. (f) Simultaneous measurement of $f_{\uparrow\downarrow}$ and $f_{\uparrow\uparrow'}$ reveals correlations between optical and microwave spectral diffusion for emitter 2.

5.4.1 SiV Hamiltonian in the presence of strain and spin-orbit coupling

The SiV electronic structure is comprised of spin-orbit eigenstates split by spin-orbit interactions. Optical transitions connect the ground state manifold (LB, UB) and excited state manifold (LB', UB') [Fig. 5.4(a)]. In a DR, phonon absorption $LB \rightarrow UB$ (and $LB' \rightarrow UB'$) is supressed, resulting in thermal polarization into LB.

We consider the ground state SiV Hamiltonian with spin-orbit and strain interactions, in the combined orbital and spin basis $\{|e_y\uparrow\rangle, |e_y\downarrow\rangle, |e_x\uparrow\rangle, |e_x\downarrow\rangle\}$ [26,76]

$$\mathcal{H}_{SiV} = \mathcal{H}_{SO} + \mathcal{H}_{\text{strain}} \tag{5.1}$$

$$= \begin{pmatrix} \alpha-\beta & 0 & \gamma-i\lambda & 0 \\ 0 & \alpha-\beta & 0 & \gamma+i\lambda \\ \gamma+i\lambda & 0 & \alpha+\beta & 0 \\ 0 & \gamma-i\lambda & 0 & \alpha+\beta \end{pmatrix} \tag{5.2}$$

where α corresponds to axial strain, β and γ correspond to transverse strain, and λ is the strength of spin-orbit interaction. Diagonalizing this reveals the orbital character of the lower branch:

$$LB \propto \begin{cases} |e_x\uparrow\rangle - \frac{1+\sqrt{1+(\gamma/\beta)^2+(\lambda/\beta)^2}}{\gamma/\beta-i\lambda/\beta}|e_y\uparrow\rangle \\ |e_x\downarrow\rangle - \frac{1-\sqrt{1+(\gamma/\beta)^2+(\lambda/\beta)^2}}{\gamma/\beta-i\lambda/\beta}|e_y\downarrow\rangle \end{cases} \tag{5.3}$$

We investigate these electronic levels in the context of the SiV as a spin-photon interface.

5.4.2 Effects of strain on the SiV qubit states

In the limit of zero crystal strain, the orbital factors simplify to the canonical form[26]

$$LB = \begin{cases} |e_+ \downarrow\rangle \\ \\ |e_- \uparrow\rangle \end{cases} \tag{5.4}$$

In this regime, the spin-qubit has orthogonal electronic orbital and spin components. As result, one would need to simultaneously drive an orbital and spin flip to manipulate the qubit, which is forbidden for direct microwave driving alone. Thus, in the low strain regime, two-photon optical transitions between the qubit states in a misaligned external field, already demonstrated at millikelvin temperatures in[122], are likely necessary to realize a SiV spin qubit.

In the high strain limit ($\sqrt{\beta^2 + \gamma^2} \gg \lambda$), these orbitals become

$$LB = \begin{cases} (\cos(\theta/2)|e_x\rangle - \sin(\theta/2)|e_y\rangle) \otimes |\downarrow\rangle \\ \\ (\cos(\theta/2)|e_x\rangle - \sin(\theta/2)|e_y\rangle) \otimes |\uparrow\rangle \end{cases} \tag{5.5}$$

where $\tan(\theta) = \frac{\beta}{\gamma}$. In this regime, the ground state orbital components are identical, and the qubit states can be described by the electronic spin degree of freedom only. As such, the magnetic dipole transition between the qubit states is now allowed and can be efficiently driven with microwaves.

In addition to determining the efficiency of qubit transitions, the spin-orbit nature of the SiV qubit states also determines its susceptibility to external fields. In an externally applied magnetic field, LB

splits due to magnetic moments associated with both spin– and orbital– angular momenta. This splitting is parameterized by an effective g-tensor which, for a fixed angle between the external field and the SiV symmetry axis, can be simplified to an effective g-factor: $\mu\, \mathrm{g}\, B_{\mathrm{ext}}/h = f_{\uparrow\downarrow}$. In the limit of large strain, the orbital component of the two LB wavefunctions converge, and g trends towards that of a free electron ($\mathrm{g} = 2$). As a result, the qubit states behave akin to a free-electron in the high strain regime, and there is no dependence of g on external field angle or small perturbations in crystal strain.

While it is difficult to probe β or γ directly, they relate to the energy difference between UB and LB via $\Delta_{\mathrm{gs}} = 2\sqrt{\beta_{\mathrm{gs}}^2 + \gamma_{\mathrm{gs}}^2 + \lambda_{\mathrm{gs}}^2}$ [Fig. 5.4(a)]. From this, we extract $\sqrt{\beta^2 + \gamma^2}$, given the known value of λ_{gs} =46 GHz[26,100,129]. Numerically diagonalizing the SiV Hamiltonian using the extracted values for β and γ closely matches the measured ground state splitting, both as a function of applied field magnitude and angle [Fig. 5.4(b)].

5.4.3 Effects of strain on the SiV spin-photon interface

Strain also plays a crucial role in determining the optical interface to the SiV spin qubit. The treatment shown above can be repeated for the excited states, with the caveat that the parameters $\beta, \gamma,$ and λ are different in the excited state manifold as compared to the ground state manifold[76]. These differences give rise to a different g-factor in the excited state (g_{es}). If the strain is much larger than both λ_{gs} =46 GHz and λ_{es} =255 GHz, then $\mathrm{g}_{\mathrm{gs}} \approx \mathrm{g}_{\mathrm{es}} \approx 2$. In this case, the two spin-cycling transition frequencies $f_{\uparrow\uparrow'}$ and $f_{\downarrow\downarrow'}$ are identical, and the only spin-selective optical transitions are the dipole-forbidden spin-flipping transitions $f_{\uparrow\downarrow'}$ and $f_{\downarrow\uparrow'}$.

Under more moderate strain, the difference $\delta g = |g_{es} - g_{gs}|$ splits the degenerate optical transitions $f_{\uparrow\uparrow'}$ and $f_{\downarrow\downarrow'}$, making them spin-selective as well. Due to differences in the anisotropic g-tensor in the ground and excited states, δg depends on the orientation of the magnetic field as well, and is minimized in the case of a $\langle 111 \rangle$-aligned field [Fig 5.4(c), inset]. In such an external field aligned with the SiV symmetry axis, optical transitions become highly spin-conserving[41], allowing many photons to scatter without altering the SiV spin state. This high cyclicity enables high-fidelity single-shot readout of the spin state[22], even without high collection efficiencies[41]. This makes working with the spin-cycling transitions highly desirable, at the expense of a reduced ability to resolve spin-selective transitions for a given field magnitude. The need to resolve individual transitions suggests an optimal strain regime where $\sqrt{\beta_{gs}^2 + \gamma_{gs}^2} \gg \lambda_{gs}$, where MW driving is efficient, while $\sqrt{\beta_{es}^2 + \gamma_{es}^2} \lesssim \lambda_{es}$, where one can independently address $f_{\uparrow\uparrow'}$ and $f_{\downarrow\downarrow'}$ [Fig. 5.4(c)].

5.4.4 Effects of strain on SiV stability

Despite the SiV's symmetry-protected optical transitions, spectral diffusion of the SiV has been observed in many experiments[130,68] (but still much smaller compared to emitters without inversion symmetry, for example, nitrogen-vacancy centers[98,131]). While the exact nature of this diffusion has not been studied in depth, it is often attributed to the second-order Stark effect or strain fluctuations, both of which affect the energies of SiV orbital wavefunctions. In this paper, we also observe significant fluctuations of the spin qubit frequency.

As can be seen in reference[76], for an appropriately low static strain value, fluctuating strain can give rise to fluctuations in the g-tensor of the ground state, causing spectral diffusion of the qubit frequency

$f_{\uparrow\downarrow}$ [Fig. 5.4(d)]. Since g_{gs} asymptotically approaches 2 as the static strain increases[76], the qubit susceptibility to this fluctuating strain is reduced in the case of highly strained SiV centers, resulting in a more stable qubit.

While spectral diffusion of the optical transition should not saturate in the same way as diffusion of the microwave transition, we observe qualitatively different spectral diffusion properties for different emitters [Fig. 5.4(e) and Fig. 5.12]. SiV 1 ($\Delta_{gs} = 500$ GHz) displays slow drift of the optical line which is stable to <100 MHz over many minutes. We do not observe significant fluctuations (> 500 kHz) of the microwave transition for this SiV. On the other hand, SiV 2 ($\Delta_{gs} = 140$ GHz) drifts over a wider range, and also exhibits abrupt jumps between several discrete frequencies.

We simultaneously record the optical transition and qubit frequency for SiV 2 and observe correlations between the two frequencies [Fig. 5.4(f)], indicating that they could arise from the same environmental perturbation. In a later section, we calculate the qubit and optical transition frequencies using the strain Hamiltonian (eq. 5.2) and find that both correlations and absolute amplitudes of spectral diffusion can simultaneously be explained by strain fluctuations on the order of 1% ($\sim 10^{-7}$ strain).

In this work we rely on static strain, likely resulting from damage induced by ion implantation and nanofabrication, and select for spectrally stable SiVs with appropriate strain profiles. This is characterized by first measuring Δ_{gs} in zero magnetic field at 4 K by exciting the optical transition $LB \rightarrow LB'$ and measuring emission from the $LB' \rightarrow UB$ on a spectrometer. We use this to screen for SiVs with Δ_{gs} >100 GHz to ensure efficient MW driving of the spin qubit. We further apply a static external magnetic field and measure spectral stability properties as well as $f_{\uparrow\uparrow'} - f_{\downarrow\downarrow'}$ to guarantee a good spin-photon interface. We measured $\sim$ 10 candidate emitters, and found 4 which satisfy all of the

necessary criteria for spin-photon experiments.

5.5 Regimes of cavity-QED for SiV spin-photon interfaces

Efficient spin-photon interactions are enabled by incorporating SiV centers into nanophotonic cavities. In this section, we describe SiV-cavity measurements in several regimes of cavity QED, and comment on their viability for spin-photon experiments.

5.5.1 Spectroscopy of cavity-coupled SiVs

We measure the spectrum of the atom-cavity system at different atom-cavity detunings in order to characterize the device and extract key cavity QED parameters [Fig. 5.5(a)]. The reflection spectrum of a two-level system coupled to a cavity is modeled by solving the frequency response of the standard Jaynes-Cummings Hamiltonian using input-output formalism for a cavity near critical coupling[11]:

$$\mathcal{R}(\omega) = \left| 1 - \frac{2\kappa_l}{i(\omega - \omega_c) + \kappa_{\mathrm{tot}} + g^2/(i(\omega - \omega_a) + \gamma)} \right|^2, \tag{5.6}$$

where κ_l is the decay rate from the incoupling mirror, κ_{tot} is the cavity linewidth, $\omega_c(\omega_a)$ is the cavity (atom) resonance frequency, g is the single-photon Rabi frequency, and γ is the bare atomic linewidth. Interactions between the SiV optical transition and the nanophotonic cavity result in two main effects. First, the SiV center can modulate the reflection spectrum of the bare cavity, as seen in the colored curves of figure 5.5(a). Second, the coupling to the cavity can broaden the linewidth of the SiV based

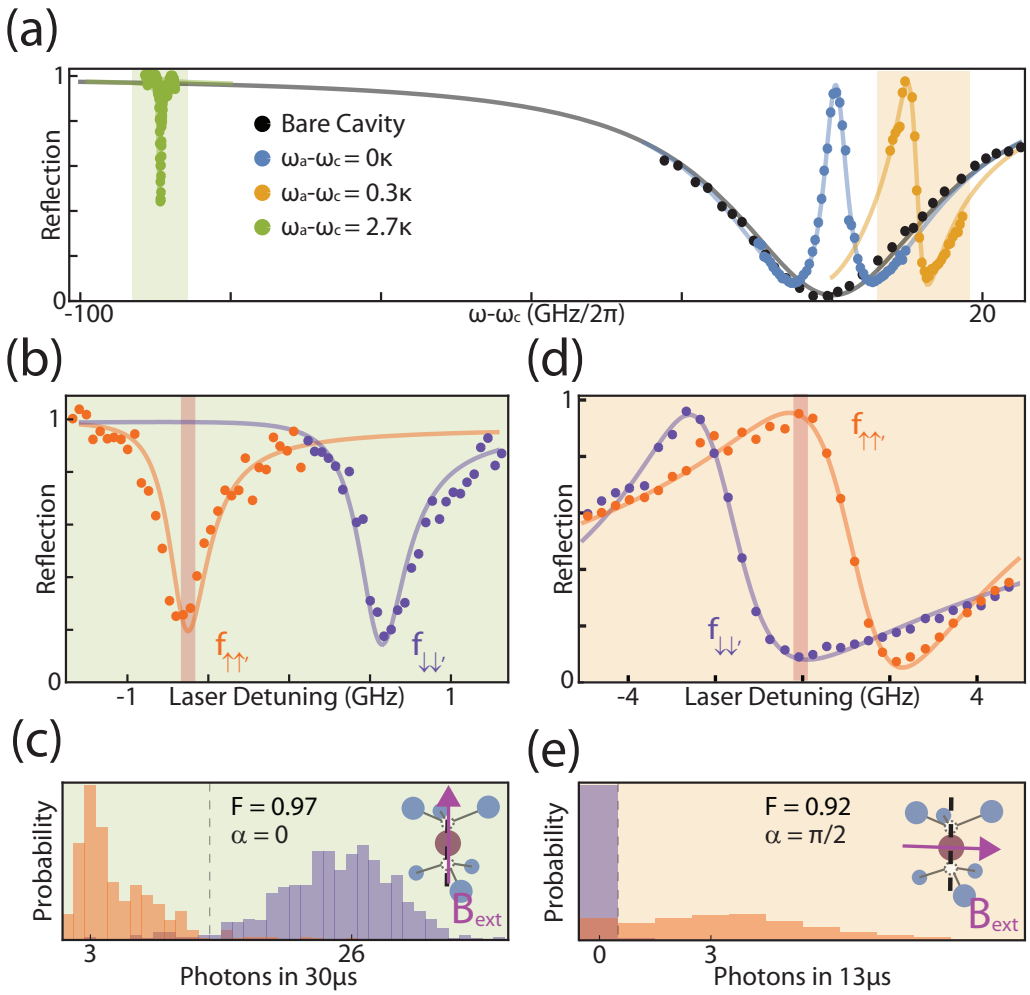


Figure 5.5: (a) SiV-cavity reflection spectrum at several detunings. The bare cavity spectrum (black) is modulated by the presence of the SiV. When the atom cavity detuing is small (Blue, orange), high-contrast, broad features are the result of Purcell enhanced SiV transitions. Far from the cavity resonance (green), interaction results in narrow SiV-assisted transmission channels. (b) Spin-dependent reflection for large SiV-cavity detuning $\Delta \approx -3\kappa, B_{\text{ext}} = 0.35\,\text{T}$. In this regime, SiV spin states can be individually addressed. (c) Probing either transmission dip results in high-fidelity single-shot readout in an aligned field ($F = 0.97$, threshold on detecting 13 photons). (d) Spin-dependent reflection near resonance $\Delta \approx 0.5\kappa, B_{\text{ext}} = 0.19\,\text{T}$. Dispersive lineshapes allow for distinguishable reflection spectra from both SiV spin states. (e) A probe at the frequency of maximum contrast (f_Q) can determine the spin state in a single shot in a misaligned field($F = 0.92$, threshold on detecting > 1 photon).

on the Purcell effect:

$$\Gamma \approx \gamma + 4g^2/\kappa \frac{1}{1 + 4(\omega_c - \omega_a)^2/\kappa^2}$$

When the cavity is far detuned from the atomic transition $|\omega_c - \omega_a| \equiv \Delta > \kappa$ [Fig. 5.5(a), green], Purcell enhancement is negligible and the cavity and atomic linewidths $\kappa, \gamma = 2\pi \times \{33, 0.1\}$ GHz are estimated. When the cavity is on resonance with the atom ($\Delta = 0$), we fit (5.6) using previously estimated values of κ and γ to extract $g = 2\pi \times 5.6$ GHz. Together, these measurements allow us to determine the atom-cavity cooperativity $C = 4g^2/\kappa\gamma = 38$. Importantly, interactions between the SiV and single photons becomes deterministic when $C > 1$.

As mentioned in section [Sec. 5.4], we would like to make use of spectrally resolved spin conserving optical transitions ($f_{\uparrow\uparrow'}, f_{\downarrow\downarrow'}$) to build a spin-photon interface using the SiV. Here, we make this criteria more explicit: $f_{\uparrow\uparrow'}$ and $f_{\downarrow\downarrow'}$ can be resolved when $|f_{\uparrow\uparrow'} - f_{\downarrow\downarrow'}| \gtrsim \Gamma$.

5.5.2 Cavity QED in the detuned regime

In the detuned regime ($\Delta > \kappa$), $\Gamma \approx \gamma$, and narrow atom-like transitions are easily resolved under most magnetic field configurations, including when the field is aligned with the SiV symmetry axis [Fig. 5.5(b)]. In this case [sec. 5.4][41], optical transitions are highly spin-conserving, and many photons can be collected allowing for high-fidelity single-shot readout of the SiV spin state ($F = 0.97$) [Fig. 5.5(c)]. Rapid, high-fidelity, non-destructive single-shot readout can enable projective-readout based initialization: after a single measurement of the SiV spin state, the probability of a measurement-induced spin flip is low, effectively initializing the spin into a known state.

While this regime is useful for characterizing the system, the maximum fidelity of spin-photon entanglement based on reflection amplitude is limited. As seen in figure 5.5(b), the contrast in the reflection signal between an SiV in $|\uparrow\rangle$ (orange) vs. $|\downarrow\rangle$ (purple) is only $\sim 80\%$, implying that in 20% of cases, a photon is reflected from the cavity independent of the spin state of the SiV, resulting in errors. We note that the residual 20% of reflection can be compensated by embedding the cavity inside an interferometer at the expense of additional technical stabilization challenges, discussed below.

5.5.3 Cavity QED near resonance

Tuning the cavity onto the atomic resonance ($\Delta \approx 0$) dramatically improves the reflection contrast [Fig. 5.5(a) (blue curve)]. Here, we observe nearly full contrast of the reflection spectrum due to the presence of the SiV. Unfortunately, this is associated with a broadened atomic linewidth ($\Gamma = \gamma(1+C) \sim$4 GHz). While it is, in principle, still possible to split the atomic lines by going to higher magnetic fields, there are several technical considerations which make this impractical. Large magnetic fields ($|B_{\mathrm{ext}}| > 0.5\,\mathrm{T}$) correspond to large qubit frequencies ($f_{\uparrow\downarrow}$), which can induce spontaneous qubit decay due to phonon emission ($|\uparrow\rangle \rightarrow |\downarrow\rangle$), as well as increased local heating of the device from microwave dissipation, both of which reduce the SiV spin coherence time rendering it ineffective as a quantum memory.

At intermediate detunings ($0 < \Delta < \kappa$), the SiV resonance is located on the cavity slope and results in high-contrast, spin-dependent Fano lineshapes which exhibit sharp features smaller than Γ [Fig. 5.5(a), orange curve]. By working at an optimal B_{ext} where the peak of one spin transition is overlapped by the valley of the other, the best features of the resonant and far-detuned regimes are

recovered [Fig. 5.5(e)]. Probing the system at the point of maximum contrast ($f_Q \approx (|f_{\uparrow\uparrow'} - f_{\downarrow\downarrow'}|)/2$, contrast $> 90\%$) enables single-shot readout of the SiV spin state for an arbitrary field orientation, even when transitions are not cycling [Fig. 5.5(f)].

This demonstrates an optical regime of cavity QED where we simultaneously achieve high-contrast readout while maintaining spin-dependent transitions. In this regime, we still expect residual reflections of about 10%, which end up limiting spin-photon entanglement fidelity. This infidelity arises because the cavity is not perfectly critically coupled ($\kappa_l \neq \kappa_{tot}/2$), and can in principle be solved by engineering devices that are more critically coupled. Alternatively, this problem can be addressed for any cavity by interfering the signal with a coherent reference to cancel unwanted reflections. In this case, one would have to embed the cavity in one arm of a stabilized interferometer. This is quite challenging, as it involves stabilizing $\sim 10\,\mathrm{m}$ long interferometer arms, part of which lie inside the DR (and experience strong vibrations from the pulse-tube cryocooler).

A fundamental issue with critically coupled cavities is that not all of the incident light is reflected from the device. If the spin is not initialized in the highly-reflecting state, photons are transmitted and not recaptured into the fiber network. Switching to overcoupled (single-sided) cavities, where all photons are reflected with a spin-dependent phase, could improve both the fidelity and efficiency of spin-photon entanglement. Once again, however, measurement of this phase would require embedding the cavity inside of a stabilized interferometer. As such, the un-compensated reflection amplitude based scheme employed here is the most technically simple approach to engineering spin-photon interactions.

5.6 Microwave spin control

While the optical interface described in previous sections enables high-fidelity initialization and readout of the SiV spin qubit, direct microwave driving is the most straightforward path towards coherent single-qubit rotations. Typically, microwave manipulation of electron spins requires application of significant microwave power. This presents a challenge, as SiV spins must be kept at local temperatures below 500 mK in order to avoid heating-related dephasing. In this section, we implement coherent microwave control of SiV centers inside nanostructures at temperatures below 500 mK.

5.6.1 Generating microwave single-qubit gates

The SiV spin is coherently controlled using amplitude and phase controlled microwave pulses generated by a Hittite signal generator (HMC-T2220). A target pulse sequence is loaded onto an arbitrary waveform generator (Tektronix AWG 7122B), which uses a digital channel to control a fast, high-extinction MW-switch (Custom Microwave Components, CMCS0947A-C2), and the analog channels adjust the amplitude and phase via an IQ-mixer (Marki, MMIQ-0416LSM). The resulting pulse train is subsequently amplified (Minicircuits, ZVE-3W-183+) to roughly 3 W of power, and sent via a coaxial cable into the dilution refrigerator. At each cryogenic flange, a 0 dB attenuator is used to thermalize the inner and outer conductors of the coaxial line while minimizing microwave dissipation. The signal is then launched into a coplanar waveguide on a custom-built circuit board (Rogers4003C, Bay Area Circuits) so it can be wire-bonded directly to the diamond chip [Sec. 5.2, Fig. 5.6(c)]. The qubit frequency ($f_{\downarrow\uparrow}$) is measured by its optically detected magnetic resonance spectrum (ODMR)

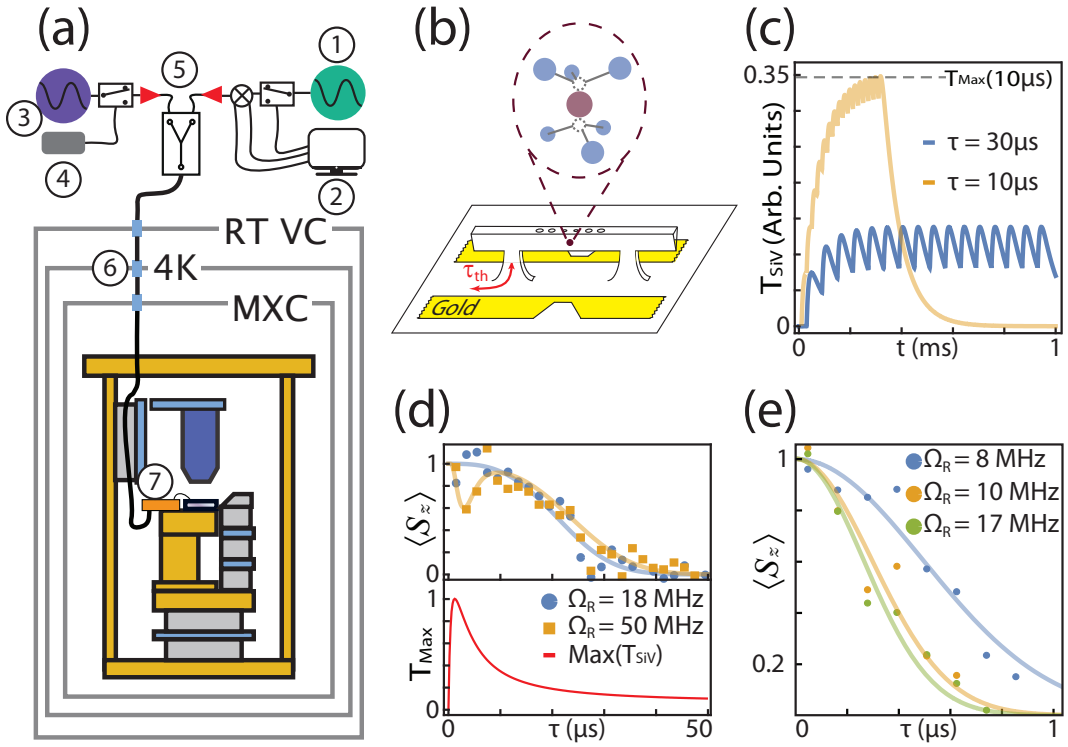


Figure 5.6: (a) Experimental schematic for microwave control. The amplitude and phase of a CW microwave source 1 are modulated via a microwave switch and IQ mixer controlled externally by an AWG 2 . A CW radio frequency source 3 is controlled using a digital delay generator 4 . Both signals are amplified by 30dB amplifiers 5 before entering the DR. 0dB cryo-attenuators 6 thermalize coax cables at each DR stage, ultimately mounted to a PCB 7 on the sample stage and delivered to the devices. (b) Schematic depicting microwaveinduced heating of devices. (c) Modeled temperature at the SiV from a dynamical decoupling sequence. At long τ , device cools down between each decoupling pulse, resulting in low temperatures. At short τ , devices are insufficiently cooled, resulting in a higer max temperature (T_{max}). (d) Effects of microwave heating on SiV coherence time. (Top panel) At high Rabi frequencies, SiV coherence is temporarily reduced for small τ . (Bottom panel) The local temperature (T_{max}) at the SiV calculated by taking the maximum value of the plots in figure (c). (e) Hahn-echo for even lower Rabi frequencies, showing coherence times that scale with microwave power

identically to the method described in [41]. We observe ODMR from 2 GHz to 20 GHz (corresponding to fields from 0.1 T to 0.7 T), implying that microwave control of SiV centers in this configuration is possible at a wide variety of external field magnitudes. This allows the freedom of tuning the field to optimize other constraints, such as for resolving spin transitions [Sec. 5.5] and identifying ancillary nuclear spins [Sec. 5.9].

Once the qubit frequency has been determined for a given field, single-qubit gates are tuned up by measuring Rabi oscillations. The frequency of these oscillations scales with the applied microwave power $\Omega_R \sim \sqrt{P}$ and determines the single-qubit gate times. We can perform π-pulses (R^{π}_{ϕ}) in under 12 ns, corresponding to a Rabi frequency exceeding 80 MHz [22]. This coherent control is used to implement pulse-error correcting dynamical decoupling sequences, either CPMG-N sequences of the form $R^{\pi/2}_x - \left(\tau - R^{\pi}_y - \tau\right)^N - R^{\pi/2}_x = x - (Y)^N - x$ [132] or XY8-N sequences of the form $x - (XYXYYXYX)^N - x$ [133]. Sweeping the inter-pulse delay τ measures the coherence time T_2 of the SiV.

5.6.2 Effects of microwave heating on coherence

As mentioned in sections 5.3 and 5.4, thermally induced T_1 relaxation can dramatically reduce SiV coherence times. To explain this phenomenon, we model the nanobeam as a $1D$ beam weakly coupled at two anchor points to a uniform thermal bath [Fig. 5.6(b)]. Initially, the beam is at the steady-state base temperature of the DR. A MW pulse instantaneously heats the bath, and the beam rethermalizes on a timescale τ_{th} set by the thermal conduction of diamond and the beam geometry. Once the pulse ends, this heat is extracted from the beam on a similar timescale. By solving the time-dependent 1-D

heat equation, we find that the change in temperature at the SiV caused by a single pulse (starting at time t_0) scales as $T_{\mathrm{SiV}} \propto (e^{-(t-t_0)/t_{\mathrm{th}}} - e^{-9(t-t_0)/t\mathrm{th}})$. We take the sum over N such pulses to model the effects of heating from a dynamical-decoupling sequence of size N.

At early times ($\tau < \tau_{\mathrm{th}}$), the SiV does not see the effects of heating by the MW line, and coherence is high. Similarly, at long times ($\tau \gg \tau_{\mathrm{th}}$) a small amount of heat is able to enter the nanostructure and slightly raise the local temperature, but this heat is dissipated before the next pulse arrives [Fig. 5.6(c), blue curve]. At intermediate timescales however, a situation can arise where the nanobeam has not fully dissipated the heat from one MW pulse before the second one arrives [Fig. 5.6(c), orange curve]. We plot the maximum temperature as seen by the SiV as a function of pulse spacing [Fig. 5.6(d), lower panel], and observe a spike in local temperature for a specific inter-pulse spacing τ, which depends on τ_{th}. Dynamical-decoupling sequences using high Rabi frequency pulses reveal a collapse in coherence at a similar time [Fig. 5.6(d), upper panel]. This collapse disappears at lower Rabi frequencies, suggesting that it is associated with heating-related dephasing. We fit this collapse to a model where the coherence time T_2 depends on temperature[102], and extract the rate of heating $\tau_{\mathrm{th}} = 70\,\mu\mathrm{s}$.

Typically, faster π-pulses improve measured spin coherence by minimizing finite-pulse effects and detuning errors. Unfortunately, as seen above, faster pulses require higher MW powers which cause heating-related decoherence in our system. We measure Hahn-echo at lower MW powers [fig. 5.6(e)], and find MW heating limits T_2 even at $\Omega_R \sim 10\,\mathrm{MHz}$. For applications where long coherence is important, such as electron-nuclear gates [Sec. 5.9], we operate at an optimal Rabi frequency $\Omega_R = 2\pi \times 10\,\mathrm{MHz}$ where nuclear gates are as fast as possible while maintaining coherence for the entire gate duration. For applications such as spin-photon entangling gates where fast gates are necessary

[Sec. 5.8], we operate at higher Rabi frequencies $\Omega_R = 2\pi \times 80$ MHz at the cost of reduced coherence times.

Heating related effects could be mitigated by using superconducting microwave waveguides. This approach would also enable the fabrication of a single, long superconducting waveguide that could simultaneously address all devices on a single chip. However, it is still an open question whether or not superconducting waveguides with appropriate critical temperature, current, and field properties can be fabricated around diamond nanostructures.

5.7 Investigating the noise bath of SiVs in nanostructures

At low temperatures, the coherence time of SiV centers drastically depends on the surrounding spin bath, which can differ from emitter to emitter. As an example, we note that the T_2 of two different SiV centers in different nanostructures scales differently with the number of applied decoupling pulses [Fig. 5.7(a)]. Surprisingly, the coherence time of SiV 2 does not scale with the number of applied pulses, while the coherence time of SiV 1 does scale as $T_2(N) \propto N^{2/3}$. Notably, both scalings are different as compared to what was previously measured in bulk diamond: $T_2(N) \propto N^1$ [41]. In this section, we probe the spin bath of these two SiVs in nanostructures to investigate potential explanations for the above observations.

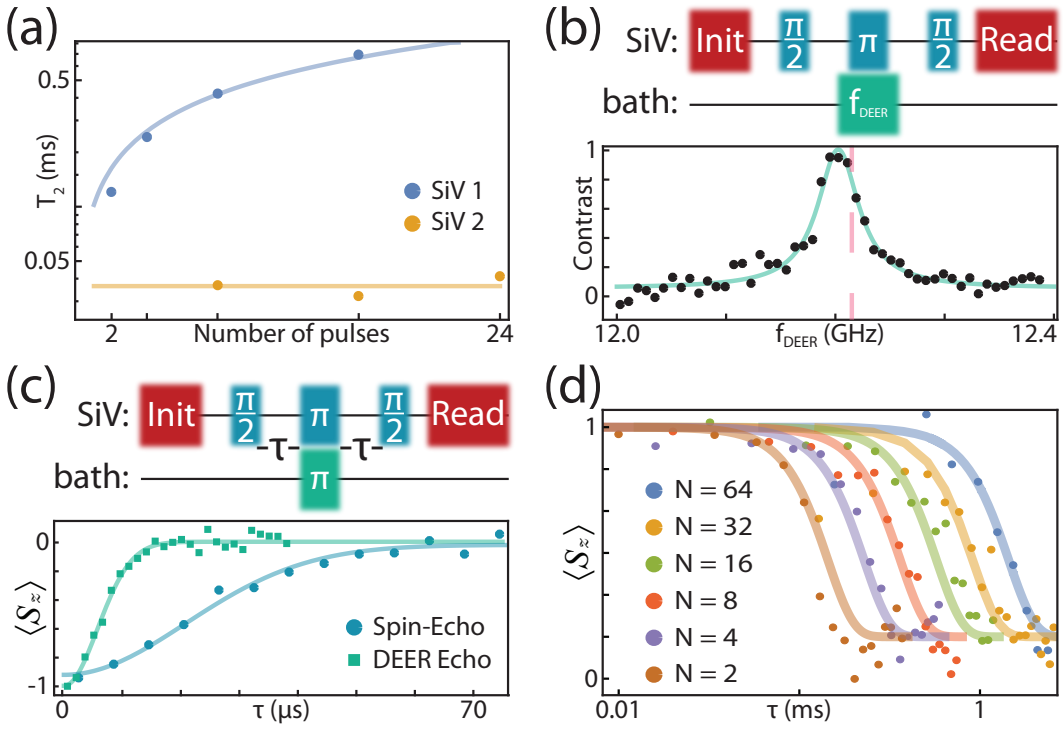


Figure 5.7: (a) T2 scaling for two different SiVs. SiV 2 exhibits no scaling with number of pulses ($T_{2,\mathrm{SiV2}} = 30\,\mu\mathrm{s}$). (b) DEER ESR on SiV 2. Vertical red line is the expected frequency of a $g = 2$ spin based on our ability to determine the applied external field (Typically to within 10%). (c) DEER Echo on SiV 2. $T_{2,DEER} = 10\,\mu\mathrm{s}$. (d) Dynamical-decoupling on SiV 1. Data points are T_2 measurements used in part (a, blue curve), and solid lines are a noise model consisting of two Lorentzian noise baths.

5.7.1 Double electron-electron resonance spectroscopy of SiVs in nanostructures

In order to investigate the poor coherence of SiV 2, we perform double electron-electron resonance (DEER) spectroscopy[134] to probe the spin bath surrounding this SiV. We perform a Hahn-echo sequence on the SiV, and sweep the frequency of a second microwave pulse (taking the RF path in figure 5.6(a)), contemporaneous with the echoing SiV π-pulse [Fig. 5.7(b), upper panel]. If this second pulse is resonant with a spin bath coupled to the SiV, the bath can flip simultaneously with the SiV, leading to increased sensitivity to noise from the bath [Fig. 5.7(b), lower panel]. We observe a significant reduction of coherence at a frequency consistent with that of a free-electron spin bath ($g_{\mathrm{bath}} = 2$) (resonance expected at $12(1)$ GHz).

Next, we repeat a standard Hahn-echo sequence where a π-pulse resonant with this bath is applied simultaneously with the SiV echo pulse (DEER echo). The coherence time measured in DEER echo is significantly shorter than for standard spin-echo, indicating that coupling to this spin bath is a significant source of decoherence for this SiV. One possible explanation for the particularly severe bath surrounding this SiV is a thin layer of alumina (Al_2O_3) deposited via atomic layer deposition on this device in order to tune cavities closer to the SiV transition frequency. The amorphous oxide layer–or its interface with the diamond crystal–can be host to a large number of charge traps, all located within $\sim$50 nm of this SiV. Unfortunately, we could not measure this device without alumina layer due to our inability to gas-tune the nanophotonic cavity close enough to the SiV resonance [Sec. 5.3].

These observations are further corroborated by DEER measurements in SiV 1, where the alumina

layer was not used (only N_2 was used to tune this cavity). In this device, we observe longer coherence times which scale $T_2(N) \propto N^{2/3}$, as well as no significant signatures from $g_{\mathrm{bath}} = 2$ spins using DEER spectroscopy. We fit this scaling to a model consisting of two weakly-coupled spin baths [Fig. 5.7(d)], and extract bath parameters b_1 =5 kHz, τ_1 =1 µs, b_2 =180 kHz, τ_2 =1 ms, where b corresponds to the strength of the noise bath, and τ corresponds to the correlation time of the noise[135,106].

While the source of this noise is an area of future study, we find that the b_2 term (likely due to bulk impurities) is the dominant contribution towards decoherence in the system. Removing this term from the model results in coherence times up to a factor of 1000 times larger than measured values. Higher-temperature[68] or *in situ*[136] annealing could potentially mitigate this source of decoherence by eliminating paramagnetic defects such as vacancy clusters. Additionally, by accompanying Si implantation with electron irradiation[137], SiV centers could be created more efficiently, and with reduced lattice damage. Finally, working with isotopically purified diamond samples with very few ^{13}C, a spin-1/2 isotope of carbon, could also result in a reduced spin bath[41].

5.8 Spin-photon entanglement

The previous sections characterize the SiV as an efficient spin-photon interface and a quantum memory with long-lived coherence. Here, we combine these two properties to demonstrate entanglement between a spin qubit and a photonic qubit. The mechanism for generating entanglement between photons and the SiV can be seen in figure 5.5(b,d): Depending on the spin state of the SiV, photons

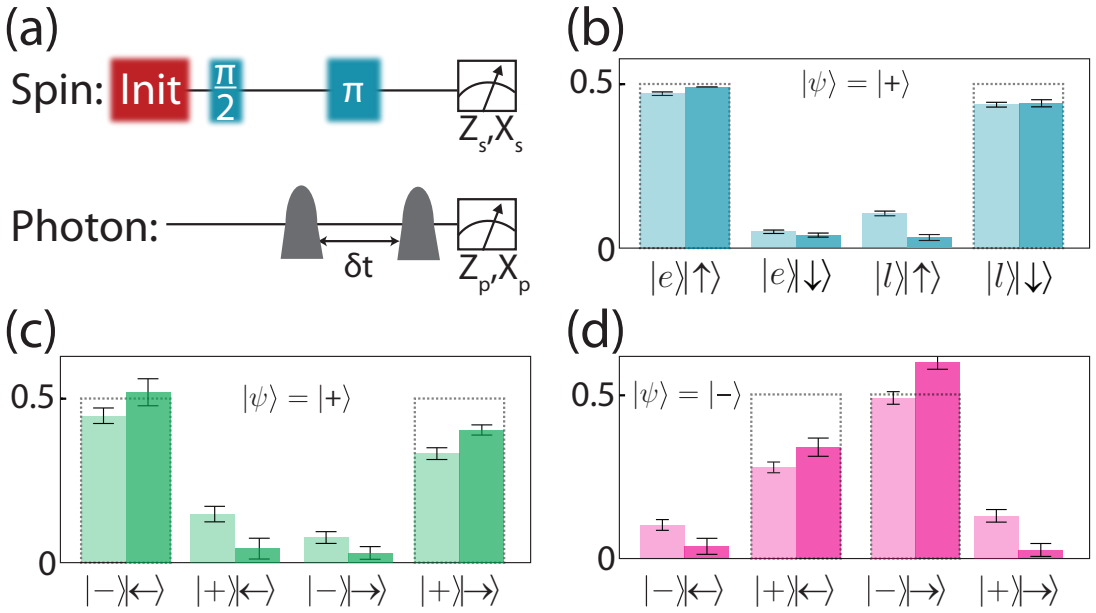


Figure 5.8: (a) Experimental sequence for generating and verifying spin-photon entanglement. A time-bin encoded qubit is reflected by the cavity, and both the SiV and the photonic qubits are measured in the Z and X bases. (b) Spin-photon correlations measured in the Z-Z basis. Light (dark) bars are before (after) correcting for known readout error associated with single-shot readout of the SiV. (c) Spin-photon correlations measured in the X-X basis. Bell-state preparation fidelity of $F \geq 0.89(3)$ and a concurrence $\mathcal{C} \geq 0.72(7)$. (d) Preparation of second spin-photon Bell state. Changing the phase of the incoming photonic qubit prepares a Bell-state with inverted statistics in the X basis.

at the probe frequency are either reflected from the cavity and detected, or are transmitted and lost.

5.8.1 Generating time-bin qubits

We begin by explaining our choice of time-bin encoding for photonic qubits. One straightforward possibility is to use the Fock state of the photon. However, it is extremely challenging to perform rotations on a Fock state, and photon loss results in an error in the computational basis. Another, perhaps more obvious possibility is to use the polarization degree of freedom. While the SiV spin-photon interface is not polarization selective (both spin states couple to photons of the same polarization), one could consider polarization based spin-photon entangling schemes already demonstated in nanophotonic systems[138,139]. However, this requires embedding the nanostructure inside of a stabilized interferometer, which has a number of challenges [Sec. 5.5]. In addition, it requires careful fabrication of overcoupled, single-sided cavities (unlike the critically coupled diamond nanocavities used here [Sec. 5.2]). As such, we believe time-bin encoding is a natural choice given the critically-coupled SiV-cavity interface described here [Sec. 5.5].

These qubits are generated by passing a weak coherent laser though a cascaded AOM, amplitude-EOM, and phase-EOM. The time-bins are shaped by an AWG-generated pulse on the amplitude-EOM, and are chosen to be much narrower than the delay δt between time bins. We can choose to prepare arbitrary initial photonic states by using the phase-EOM to imprint an optional phase shift to the second bin of the photonic qubit. Since we use a laser with Poissonian photon number statistics, we set the average photon number $\langle n_{ph} \rangle = 0.008 \ll 1$ using the AOM to avoid events where two photons are incident on the cavity.

Using this encoding, measurements in a rotated basis (X-basis) become straightforward. We send the time-bin qubit into an actively stabilized, unbalanced, fiber-based, Mach-Zender interferometer, where one arm passes through a delay line of time δt. With 25% probability, $|e\rangle$ enters the long arm of the interferometer and $|l\rangle$ enters the short arm, and the two time bins interfere at the output. Depending on the relative phase between the two bins, this will be detected on only one of the two arms of the interferometer output [Fig. 5.3(b)], corresponding to a measurement in the X basis of $|\pm\rangle$.

5.8.2 Spin-photon Bell states

We prepare and verify the generation of maximally entangled Bell states between the SiV and a photonic qubit using the experimental sequence depicted in figure 5.8(a). First, the SiV is initialized into a superposition state $|\rightarrow\rangle = 1/\sqrt{2}(|\uparrow\rangle + |\downarrow\rangle)$. Then photons at frequency f_Q [Sec. 5.5] are sent to the cavity, corresponding to an incoming photon state $|+\rangle = 1/\sqrt{2}(|e\rangle + |l\rangle)$, conditioned on the eventual detection of only one photon during the experiment run. Before any interactions, this state can be written as an equal superposition: $\Psi_0 = |\rightarrow\rangle \otimes |+\rangle = 1/2(|e\uparrow\rangle + |e\downarrow\rangle + |l\uparrow\rangle + |l\downarrow\rangle)$. The first time bin is only reflected from the cavity if the the SiV is in state $|\uparrow\rangle$, effectively carving out $|e\downarrow\rangle$ in reflection[92]. A π-pulse on the SiV transforms the resulting state to $\Psi_1 = 1/\sqrt{3}(|e\downarrow\rangle + |l\downarrow\rangle + |l\uparrow\rangle)$. Finally, reflection of the late time-bin off of the cavity carves out the state $|l\downarrow\rangle$, leaving a final entangled state $\Psi_2 = 1/\sqrt{2}(|e\downarrow\rangle + |l\uparrow\rangle)$. To characterize the resulting state, we perform tomography on both qubits in the Z and X bases [Fig. 5.8(a)].

In order to enable high-bandwidth operation and reduce the requirements for laser and interferometric stabilization in generating and measuring time-bin qubits, it is generally beneficial to set δt

as small as possible. The minimum δt is determined by two factors: First, each pulse must be broad enough in the time-domain (narrow enough in the frequency domain) so that it does not distort upon reflection off of the device. From figure 5.5(d), the reflection specturm is roughly constant over a $\sim 100\,\mathrm{MHz}$ range, implying that $\sim$ nanosecond pulses are sufficient. The second consideration is that a microwave π-pulse must be placed between the two pulses. In this experiment, we drive fast $(12\,\mathrm{ns})$ π-pulses. As such, we set $\delta t = 30\,\mathrm{ns}$ and use $5\,\mathrm{ns}$ optical pulses to satisfy these criteria.

5.8.3 Spin-photon entanglement measurements

For Z-basis measurements, photons reflected from the cavity are sent directly to a SPCM and the time-of-arrival of the time-bin qubit is recorded. Afterwards, the SiV is read out in the Z-basis [Sec. 5.5]. Single-shot readout is calibrated via a separate measurement where the two spin-states are prepared via optical pumping and read out, and the fidelity of correctly determining the $|\uparrow\rangle$ ($|\downarrow\rangle$) state is $F_\uparrow = 0.85$ ($F_\downarrow = 0.84$), limited by the large o component of the geometric distribution which governs photon statistics for spin-flip systems [Sec. 5.5]. In other words, since we work in a misaligned field in this experiment, the probability of a spin flip is high, making it somewhat likely to measure o photons regardless of initial spin state. Even before accounting for this known error, we observe clear correlations between the photonic and spin qubits [Fig. 5.8(b), light-shading]. Error bars for these correlation histograms (and the following fidelity calculations) are estimated by statistical bootstrapping, where the scattered photon histograms (post-selected on the detection of $|e\rangle$ or $|l\rangle$) are randomly sampled in many trials, and the variance of that ensemble is extracted.

Measurements in the X-basis are performed similarly. The photon is measured through an interfer-

ometer as described above, where now the detector path information is recorded for the overlapping time-bin. After a $R_y\pi/2$ pulse on the SiV, the scattered photon histograms again reveal significant correlations between the '+' and '-' detectors and the SiV spin state [fig. 5.8(c)]. By adding a π-phase between the early and late time bins, we can prepare an orthogonal Bell state. Measured correlations of this state are flipped in the X-basis [Fig. 5.8(d)].

Measurements of this Bell state in the Z- and X-bases are used to estimate a lower bound on the fidelity: $F = \langle\Psi^+|\rho|\Psi^+\rangle \geq 0.70(3)$ ($F \geq 0.89(3)$ after correcting for readout errors). The resulting entangled state is quantified by its concrrence $\mathcal{C} \geq 0.42(6)$ ($\mathcal{C} \geq 0.79(7)$ after correcting for readout errors). This high-fidelity entangled state between a photonic qubit and a quantum memory is a fundamental resource for quantum communication[86] and quantum computing schemes[89], and can be used, for example, to demonstrate heralded storage of a photonic qubit into memory[22].

5.9 Control of SiV-^{13}C register

While demonstrations of a quantum node with a single qubit is useful for some protocol, nodes with several interacting qubits enable a wider range of applications, including quantum repeaters[10]. In this section, we introduce additional qubits based on ^{13}C naturally occurring in diamond [sec. 5.7].

5.9.1 Coupling between the SiV and several ^{13}C

For all of the emitters investigated in section 5.6, we observe collapses in the echo signal corresponding to entanglement with nearby nuclear spins [Fig. 5.9(a)]. As the diamond used in this work has 1% ^{13}C [Sec. 5.7], we typically observe several such nuclei, with all of their resonances overlapping due to

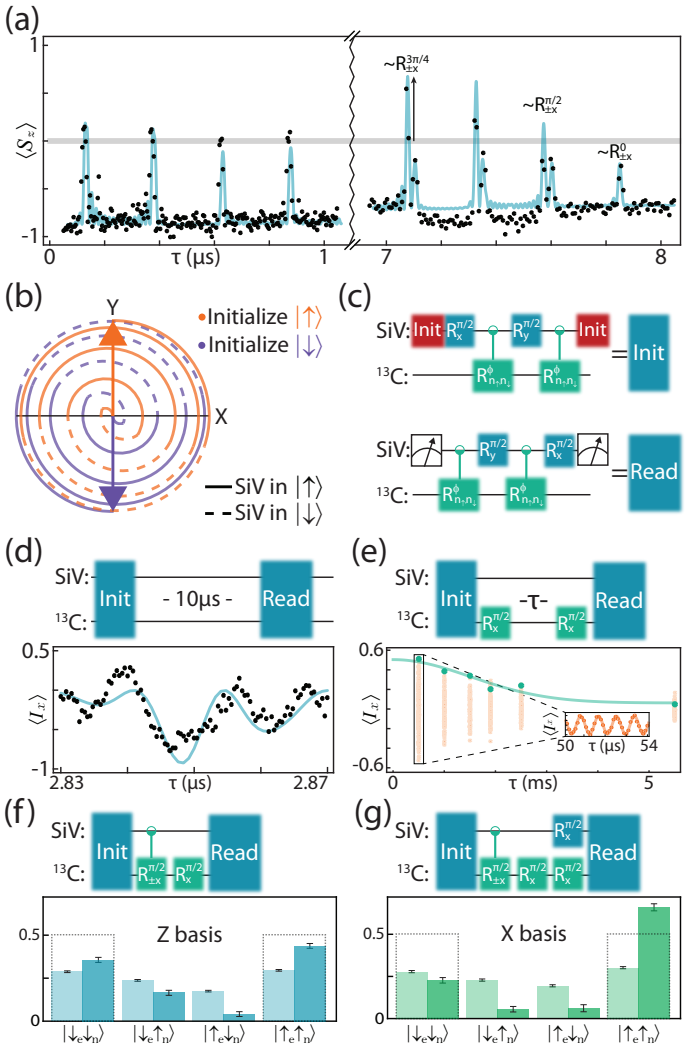


Figure 5.9: (a) XY8-2 spin echo sequence reveals coupling to nuclear spins. (Left panel) Collapses $\langle S_x \rangle = 0$ at short times indicate coupling to many nuclei. (Right panel) Collapses $\langle S_x \rangle \neq 0$ at long times indicate conditional gates on a single nuclear spin. (b) Trajectory of ^{13}C on the Bloch sphere during a maximally entangling gate. Orange (purple) lines correspond to the SiV initially prepared in state $|\uparrow\rangle$ ($|\uparrow\rangle$); transitions from solid to dashed lines represent flips of the SiV electronic spin during the gate. (c) Maximally entangling gates of the form $\mathcal{R}^{\phi}_{\vec{n_\uparrow},\vec{n_\downarrow}}$ are used to initialize and readout the two-qubit register. (d) Tuning up an initialization gate. Inter-pulse spacing τ for Init and Read gates are swept to maximize polarization. Solid line is the modeled pulse sequence using the hyperfine parameters extracted from (a). (e) Nuclear Ramsey measurement. Driving the ^{13}C using composite gates on the SiV reveals $T_2^* = 2.2\,\mathrm{ms}$. (Inset) Orange points are coherent oscillations of the Ramsey signal due to hyperfine coupling to the SiV. (f) Electron-nuclear correlations measured in the ZZ-basis. Light (dark) bars are before (after) correcting for known errors associated with reading out the SiV and ^{13}C. (g) Electron-nuclear correlations measured in the XX-basis. We estimate a Bell state preparation fidelity of $F \geq 0.59(4)$ and a concurrence $\mathcal{C} \geq 0.22(9)$.

their second-order sensitivity to hyperfine coupling parameters[22]. Consequently, during a spin echo sequence the SiV entangles with many nuclei, quickly losing coherence and resulting in a collapse to $\langle S_z \rangle = 0$ [Fig. 5.9(a), left side]. If single ^{13}C can be addressed however, this entanglement results in coherent population transfer and echo collapses which can, in some cases, completely flip the SiV spin state ($\langle S_z \rangle = \pm 1$). This entanglement forms the basis for quantum gates [Fig. 5.9(a), right side]. These gates can be tuned by changing the alignment of B_{ext} with respect to the hyperfine coupling tensor, or by using different timings. Unfortunately, as a result of the complicated nuclear bath for this device, a majority of field orientations and amplitudes only show collapses to $\langle S_z \rangle = 0$. The highest fidelity nuclear gates demonstrated here are based on echo resonances with the largest contrast which, crucially, were not commensurate with an aligned field. Thus, in this device, single ^{13}C could only be isolated at the cost of lower SSR fidelity [Sec. 5.5].

5.9.2 Initializing the nuclear spin

Once a single nuclear spin is identified, resonances in spin-echo form the building block for quantum gates. For example, a complete flip of the SiV is the result of the nuclear spin rotating by π conditionally around the axes $\pm$X ($\mathcal{R}^{\pi}_{\pm x,\text{SiV}-\text{C}}$), depending on the state of the SiV. We can vary the rotation angle of this pulse by choosing different spacings τ between pulses [Fig. 5.9(a)], or by using different numbers of π-pulses. We find a maximally entangling gate ($\mathcal{R}^{pi/2}_{\pm x,\text{SiV}-\text{C}}$) by applying $N = 8$ π-pulses separated by $2\tau = 2 \times 2.859\,\mu$s. This can be visualized on the Bloch sphere in figure 5.9(b), where the state of the SiV (orange or purple) induces different rotations of the ^{13}C.

A similarly constructed entangling gate ($\mathcal{R}^{\phi}_{\vec{n_\uparrow},\vec{n_\downarrow}}$, discussed in a later section is used to coherently

map population from the SiV onto the nuclear spin or map population from the nuclear spin onto the SiV [Fig. 5.9(c)]. The fidelity of these gates is estimated by polarizing the SiV, mapping the population onto the ^{13}C, and waiting for $T \gg T_2^*$ (allowing coherence to decay) before mapping the population back and reading out [Fig. 5.9(d)]. We find that we can recover 80% of the population in this way, giving us an estimated initialization and readout fidelity of $F = 0.9$.

Based on the contrast of resonances in spin-echo (also 0.9), this is likely limited by entanglement with other nearby ^{13}C for this emitter, as well as slightly sub-optimal choices for τ and N. Coupling to other ^{13}C results in population leaking out of our two-qubit register, and can be improved by increasing sensitivity to single ^{13}C, or by looking for a different emitter with a different ^{13}C distribution. The misaligned external field further results in slight misalignment of the nuclear rotation axis and angle of rotation, and can be improved by employing adapted control sequences to correct for these errors[110,111].

5.9.3 Microwave control of nuclear spins

As demonstrated above, control of the ^{13}C via composite pulse sequences on the SiV is also possible. A maximally entangling gate has already been demonstrated and used to initialize the ^{13}C, so in order to build a universal set of gates, all we require are unconditional single-qubit rotations. This is done following reference[108], where unconditional nuclear rotations occur in spin-echo sequences when the inter-pulse spacing τ is halfway between two collapses. For the following gates, we use an unconditional $\pi/2$-pulse composed of 8 π-pulses separated by $\tau = 0.731\,\mu$s.

We use this gate to probe the coherence time T_2^* of the ^{13}C. After mapping population onto the nu-

clear spin, the SiV is re-initialized, and then used to perform unconditional $\pi/2$-rotations on the ^{13}C [Fig. 5.9(d)]. Oscillations in the signal demonstrate Larmor precession of the nucleus at a frequency determined by a combination of the external field as well as ^{13}C-specific hyperfine interactions[22], which are seen as the orange data points in figure 5.9(d). The green envelope is calculated by fitting the oscillations and extracting their amplitude. The decay of this envelope $T_2^* = 2.2\,\mathrm{ms}$ shows that the ^{13}C has an exceptional quantum memory, even in the absence of any dynamical decoupling.

We characterize the fidelity of our conditional and unconditional nuclear gates by generating and reading out Bell states between the SiV and ^{13}C. First, we initialize the 2-qubit register into one of the 4 eigenstates: $\{|\uparrow_e\uparrow_N\rangle, |\uparrow_e\downarrow_N\rangle, |\downarrow_e\uparrow_N\rangle, |\downarrow_e\downarrow_N\rangle\}$, then perform a $\pi/2$-pulse on the electron to prepare a superposition state. Afterward, a CNOT gate, comprised of an unconditional $\pi/2$ pulse followed by a maximally entangling gate, prepares one of the Bell states $|\Psi_\pm\rangle, |\Phi_\pm\rangle$ depending on the initial state [Fig. 5.9 (e,f)]. We report an error corrected fidelity of $F \geq 0.59(4)$ and $\mathcal{C} \geq 0.22(9)$, primarily limited by our inability to initialize the ^{13}C[22].

5.9.4 Radio-frequency driving of nuclear spins

The previous section demonstrated a CNOT gate between SiV and ^{13}C using composite MW pulses. This approach has several drawbacks. First, the gate fidelity is limited by our ability to finely tune the rotation angle of the maximally entangled gate which can not be done in a continuous fashion [see Fig.9(a)]. Second, this gate requires a specific number of MW pulses and delays between them, making the gate duration ($\sim$50 μs in this work) comparable to the SiV coherence time. Finally, this scheme relies on a second order splitting of individual ^{13}C resonances to resolve individual ones; resid-

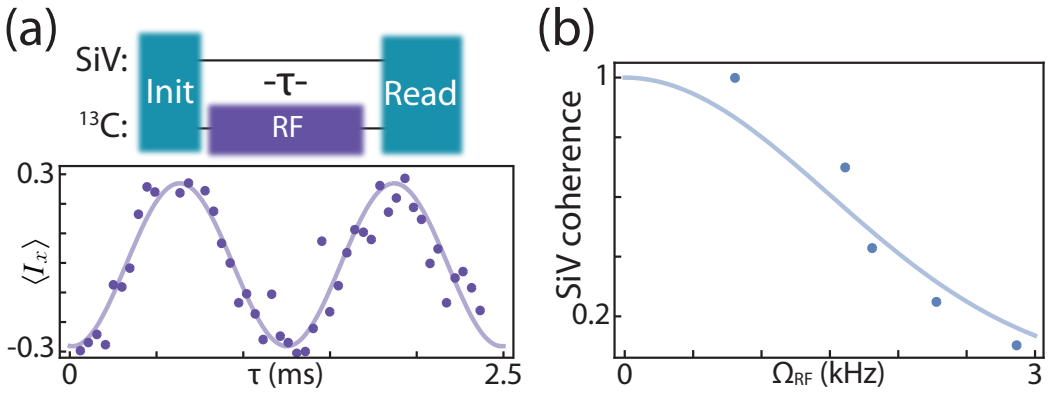


Figure 5.10: (a) RF Rabi oscillations. Applying an RF tone directly drives nuclear rotations of a coupled ^{13}C. (b) SiV coherence in the presence of an RF drive. As the strength of the RF drive is increased, local heating from the CPW reduces the SiV T_2.

ual coupling to additional ^{13}C limits the fidelity for a pulse sequence of given total length.

Direct RF control[113] would be a simple way to make a fast and high-fidelity CNOT gate since it would require a single RF π-pulse on a nuclear spin transition[140]. Furthermore, since the nuclear spin transition frequencies depend on the hyperfine coupling to leading order, these pulses could have higher ^{13}C selectivity and potentially shorter gate duration.

We use the RF port inside the DR [Sec. 5.6] to apply RF pulses resonant with nuclear spin transitions. Figure 5.9(a) shows RF Rabi oscillations of the nuclear spin. Since the ^{13}C gyromagnetic ratio is about 3 orders of magnitude smaller compared to the SiV spin, RF driving is much less efficient than MW one and requires much more power. To investigate local heating of the SiV [Sec. 5.6] we measured the SiV spin coherence contrast in spin-echo sequence right after applying off-resonant RF pulse of 100 μs at different power (calibrated via RF rabi oscillations) [Figure 5.9(b)]. Unfortunately, Even modest Rabi frequencies (Ω_{RF} $\sim$1 kHz) result in 20% loss in SiV coherence. Replacing the gold CWG used in this work by superconducting ones may solve heating issue and make RF driving

practically useful.

5.10 Nanophotonic cavity design

We simulate and optimize our nanophotonic structures to maximize atom-photon interactions while maintaining high waveguide coupling, which ensures good collection efficiency for the devices. In particular, this requires optimizing the device quality-factor to mode volume ratio, the relative rates of scattering into waveguide modes, and the size and shape of the optical mode. Each of these quantities are considered in a three-step simulation process (FDTD, Lumerical). We first perform a coarse parameter sweep over all possible unit cells which define the photonic crystal gemometry and identify families of bandgap-generating structures. These structures are the starting point for a gradient ascent optimization procedure, which results in generating high quality-factor, low mode volume resonators. Finally, the generated designs are modified to ensure efficient resonator-waveguide coupling.

Optimization begins by exploring the full parameter space of TE-like bandgap generating structures within our waveguide geometry. For hole-based cavities [Fig. 5.11(a)], this sweep covers a 5-dimensional parameter space: The lattice constant of the unit cell (a), the hole size and aspect ratio (H_x and H_y), the device etch angle (θ) and the waveguide width (w). Due to the size of this parameter space, we start by performing a low-resolution sweep over all parameters, with each potential design simulated by a single unit cell with the following boundary conditions: 4 perfectly matched layer (PML) boundary conditions in the transverse directions and 2 Bloch boundary conditions in the waveguide directions. The band structure of candidate geometries are determined by sweeping the

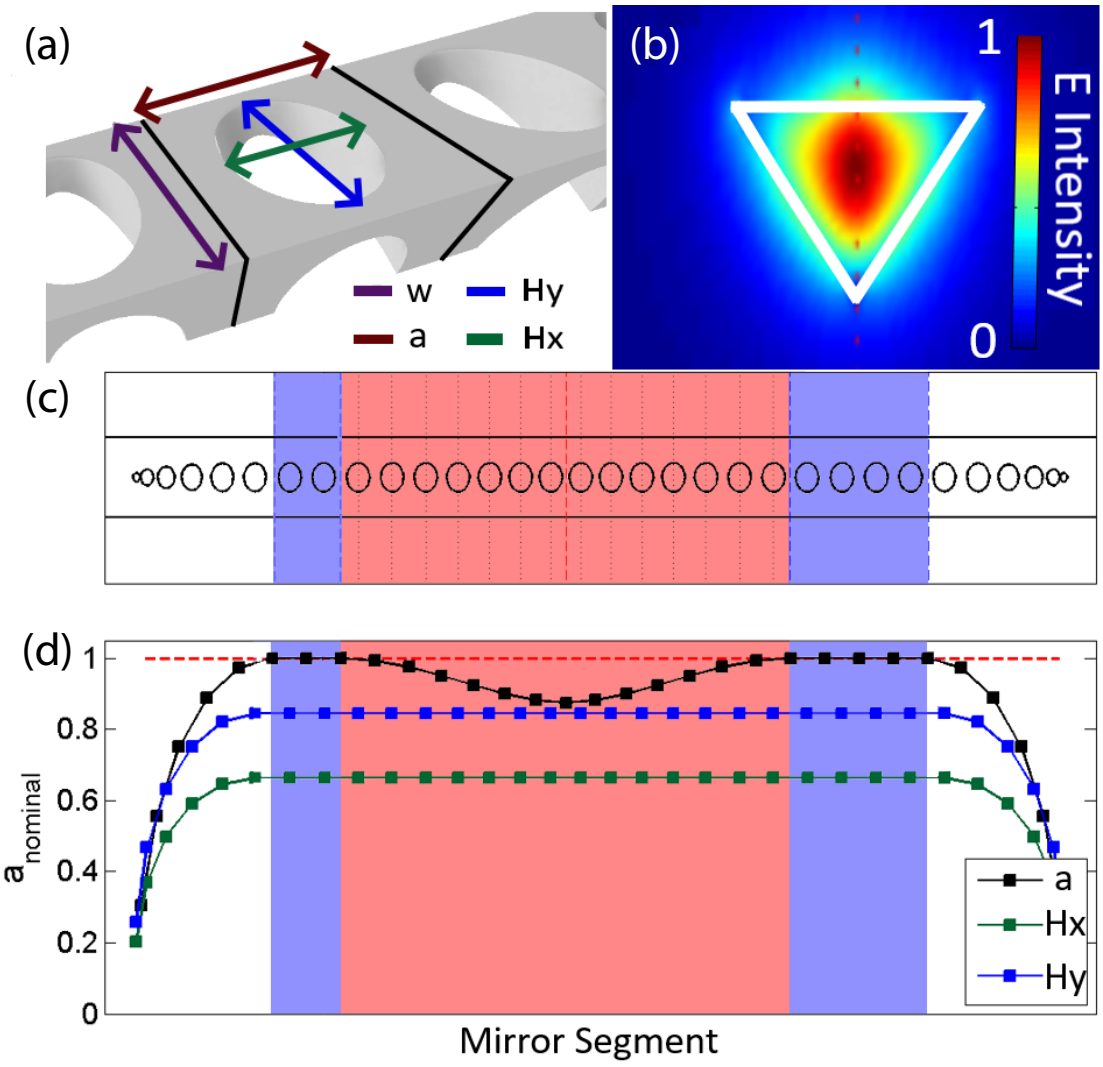


Figure 5.11: (a) Unit cell of a photonic crystal cavity (bounded by black lines). H_x and H_y define the size and aspect ratio of the hole, a determines the lattice constant, and w sets the waveguide width. (b) Electric field intensity profile of the TE mode inside the cavity, indicating strong confinement of the optical mode inside the waveguide. (c) Schematic of photonic crystal design. Blue shaded region is the bandgap generating structure, red shaded region represents the cavity structure. (d) Plot of a, H_x, and H_y for the cavity shown in (c), showing cubic taper which defines the cavity region. All sizes are shown in fractions of a_{nominal}, the unperturbed lattice constant.

effective k-vector of the Bloch boundary condition and identifying allowed modes. Using this technique, families of similar structures with large bandgaps near the SiV transition frequency are chosen for further simulation. Each candidate photonic crystal is also inspected for the position of its optical mode maximum, ensuring that it has first-order modes concentrated in the center of the diamond, where SiVs will be incorporated [Fig. 5.11(b)].

The second step is to simulate the full photonic crystal cavity design, focused in the regions of parameter space identified in step one. This is done by selecting a fixed θ, as well as a total number of unit cells that define the structure, then modifying the bandgap of the photonic crystal with a defect region to form a cavity mode. We define this defect using a cubic tapering of one (or several) possible parameters:

$$A(x) = 1 - d_{\max}|2x^3 - 3x^2 + 1| \tag{5.7}$$

where A is the relative scale of the target parameter(s) at a distance x from the cavity center, and $d_{\max}$ is the defect depth parameter. Photonic Crystal cavities with multi-parameter defects are difficult to reliably fabricate, therefore, devices used in this work have cavity defect geometries defined only by variations in the lattice constant. The cavity generated by this defect is scored by simulating the optical spectrum and mode profile and computing the scoring function F:

$$F = \min(Q, Q_{\text{cutoff}})/(Q_{\text{cutoff}} \times V_{\text{mode}}) \tag{5.8}$$

Where Q is the cavity quality-factor, $Q_{\text{cutoff}} = 5 \times 10^5$ is an estimated maximum realizable Q based

on fabrication constraints, and V_{mode} is the cavity mode volume. Based on this criteria, we employ a gradient ascent process over all cavity design parameters (except θ and the total number of unit cells) until F is maximized, or a maximum number of iterations has occurred. Due to the complexity and size of the parameter space, a single iteration of this gradient ascent is unlikely to find the optimal structure. Instead, several candidates from each family of designs found in step one are explored, with the best moving on to the final step of the simulation process. These surviving candidates are again checked to ensure confinement of the optical mode in the center of the cavity structure and to ensure that the structures fall within the tolerances of the fabrication process.

The final step in the simulation process is to modify the optimized designs to maximize resonator-waveguide coupling. This is done by removing unit cells from the input port of the device, which decreases the overall quality-factor of the devices in exchange for better waveguide damping of the optical field. Devices are once again simulated and analyzed for the fraction of light leaving the resonator through the waveguide compared to the fraction scattering into free-space. The number of unit cells on the input port is then optimized for this ratio, with simulations indicating that more than 95% of light is collected into the waveguide. In practice, fabrication defects increase the free-space scattering rate, placing resonators close to the critically-coupled regime. Finally, the waveguide coupling fraction is increased by appending a quadratic taper to both ends of the devices such that the optical mode is transferred adiabatically from the photonic crystal region into the diamond waveguide. This process produces the final cavity structure used for fabrication [Fig. 5.11(c)].

5.11 Strain-induced frequency fluctuations

Here we calculate changes the SiV spin-qubit frequency and optical transition frequency arising from strain fluctuations. We start with the Hamiltonian for SiV in an external magnetic field B_z aligned along trhe SiV symmetry axis[26,76]:

$$H = -\lambda \underbrace{\begin{pmatrix} 0 & 0 & i & 0 \\ 0 & 0 & 0 & -i \\ -i & 0 & 0 & 0 \\ 0 & i & 0 & 0 \end{pmatrix}}_{\text{spin-orbit}} + \underbrace{\begin{pmatrix} \alpha-\beta & 0 & \gamma & 0 \\ 0 & \alpha-\beta & 0 & \gamma \\ \gamma & 0 & \beta & 0 \\ 0 & \gamma & 0 & \beta \end{pmatrix}}_{\text{strain}} + \underbrace{q\gamma_L B_z \begin{pmatrix} 0 & 0 & i & 0 \\ 0 & 0 & 0 & i \\ -i & 0 & 0 & 0 \\ 0 & -i & 0 & 0 \end{pmatrix}}_{\text{orbital Zeeman}} + \underbrace{\frac{\gamma_S B_z}{2} \begin{pmatrix} 1 & 0 & 0 & 0 \\ 0 & -1 & 0 & 0 \\ 0 & 0 & 1 & 0 \\ 0 & 0 & 0 & -1 \end{pmatrix}}_{\text{spin Zeeman}}, \quad (5.9)$$

where λ is a spin-orbit coupling constant, $\gamma_L = \mu_B$ and $\gamma_S = 2\mu_B$ are Landé g-factors of the orbital and spin degrees of freedom (μ_B the Bohr magneton), $q = 0.1$ is a Ham reduction factor of the orbital momentum[141,26], and α, β, γ are local strain parameters which can be different for the ground and excited sates [Sec. 5.4]. As measuring the exact strain parameters is challenging [Sec. 5.4] we assume only one non-zero component in this tensor (ϵ_{zx}) in order to simplify our calculations. In this case,

strain parameters are:

$$\beta = f_{\mathrm{g(e)}}\epsilon_{zx}, \tag{5.10}$$

$$\alpha = \gamma = 0, \tag{5.11}$$

where $f_{\mathrm{g(e)}} = 1.7 \times 10^6$ (3.4×10^6) GHz/strain[76] for the ground (excited) state and the GS splitting is:

$$\Delta_{GS} = 2\sqrt{\lambda_g^2 + \beta^2}, \tag{5.12}$$

where $\lambda_g \approx 25$ GHz is the SO-constant for the ground state. Next, we solve this Hamiltonian and investigate how the qubit frequency changes as a function of relative strain fluctuations (ξ):

$$\Delta f_{\mathrm{MW}} = \frac{2\left(f_{\mathrm{g}}\epsilon_{zx}\right)^2 \lambda_g B_z q \gamma_L}{\left(\left(f_{\mathrm{g}}\epsilon_{zx}\right)^2 + \lambda_g^2\right)^{3/2}}\xi. \tag{5.13}$$

The corresponding change in the optical frequency is:

$$\Delta f_{\mathrm{optical}} = \left(\frac{\left(f_{\mathrm{g}}\epsilon_{zx}\right)^2}{\sqrt{\left(f_{\mathrm{g}}\epsilon_{zx}\right)^2 + \lambda_g^2}} - \frac{\left(f_{\mathrm{e}}\epsilon_{zx}\right)^2}{\sqrt{\left(f_{\mathrm{e}}\epsilon_{zx}\right)^2 + \lambda_e^2}}\right)\xi, \tag{5.14}$$

where $\lambda_e \approx 125$ GHz is the SO-constant for the excited state.

For SiV 2 [Sec. 5.4] we measured $\Delta_{GS} = 140$ GHz and find $\epsilon_{zx} = 3.8 \times 10^{-5}$. With $\xi = 1\%$ strain fluctuations (corresponding to $\sim 10^{-7}$ strain), frequencies change by $\Delta f_{\mathrm{MW}} \approx 4$ MHz and $\Delta f_{\mathrm{optical}} \approx -300$ MHz. This quantitatively agrees with the data presented in [Fig. 5.4(f)].

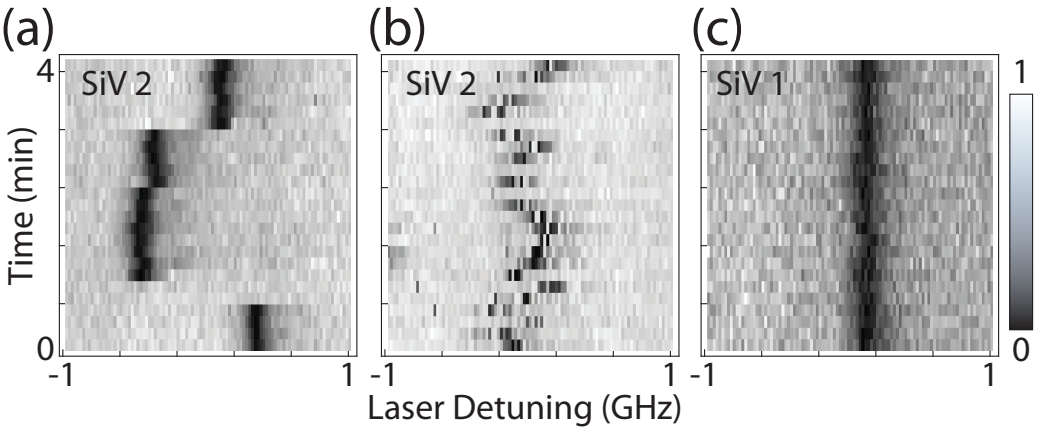


Figure 5.12: (a) Spectral diffusion of SiV 2. We observe slow spectral wandering as well as spectral jumps. (b) Applying a short green repumping pulse before every measurement significanly speeds up the timescale for spectral diffusion. (c) Spectral diffusion of SiV 1 in nanostructures. Line is stable to below $100\,\mathrm{MHz}$ over many minutes. Scale bar indicates normalized SiV reflection signal.

5.12 Mitigating spectral diffusion

In order to couple SiV centers to a quantum network, electronic transitions must be stabilized with respect to a probe laser. We note that such spectral diffusion is a universal challenge for solid-state quantum systems[98,142,143]. In the case of the SiV center, spectral diffusion can be seen explicitly in figure 5.12(a), where the optical transition frequency can either drift slowly (central region), or undergo large spectral jumps. As this diffusion can be larger than the SiV linewidth, any given instance of an experiment could have the probe laser completely detuned from the atomic transition, resulting in a failed experiment.

There are several possible solutions to mitigate this spectral diffusion. First, exploiting a high-cooperativity interface, one can Purcell-broaden the optical linewidth [sec. 5.5] to exceed the spectral diffusion[19]. Second, a high collection efficiency can be used to read out the optical position faster than

the spectral diffusion. The frequency can then be probabilistically stabilized by applying a short laser pulse at 520 nm which dramatically speeds up the timescale of spectral diffusion,[42,70] [Fig. 5.12(b)]. Alternatively this signal could be used to actively stabilize the line using strain-tuning[39,112]. From the observations in figure 5.4(f), this technique should mitigate spectral diffusion of both the optical and spin transitions. Strain tuning also offers the capability to control the DC strain value, which has important effects on qubit properties as discussed previously, and enables tuning multiple SiV centers to a common network operation frequency. As such, this tunability will likely be an important part of future quantum networking technologies based on SiV centers.

The severity of spectral diffusion is different for different emitters however, and this control is not always necessary, especially for proof-of-principle experiments with a small number of emitters. For SiV 1, the main SiV used in the following sections, and the SiV used in ref[22], we find almost no spectral diffusion, with optical transitions stable over many minutes [Fig. 5.12(c)]. This is an ideal configuration, as experiments can be performed without any need to verify the optical line position.

5.13 Model for SiV decoherence

The scaling of $T_2(N) \propto N^{2/3}$ is identical to that found for nitrogen-vacancy centers, where it is assumed that T_2 is limited by a fluctuating electron spin bath[135,106]. Motivated by DEER measurements with SiV 2, we follow the analysis of ref.[106] to estimate the noise bath observed by SiV 1.

The measured coherence decay is modeled by:

$$\langle S_z \rangle = \mathrm{Exp}\left(- \int \mathrm{d}\omega \, S(\omega) \mathcal{F}_N(t, \omega) \right), \tag{5.15}$$

where $S(\omega)$ is the noise power-spectrum of the bath, and $\mathcal{F}_N(t, \omega) = 2\sin(\omega t/2)(1 - \sec(\omega t/2N))^2/\omega^2$ is filter function for a dynamical-decoupling sequence with an even number of pulses[106]. We fit successive T_2 echo curves to the functional form $A + Be^{-(t/T_2)^\beta}$, with A, B being free parameters associated with photon count rates, and $\beta = 3$ providing the best fit to the data. This value of β implies a decoherence bath with a Lorentzian noise power-spectrum, $S(\omega, b, \tau) = b^2\tau/\pi \times 1/(1 + \omega^2\tau^2)$, where b is a parameter corresponding to the strength of the noise bath, and τ is a parameter corresponding to the correlation time of the noise[135,106].

Empirically, no one set of noise parameters faithfully reproduces the data for all measured echo sequences. Adding a second source of dephasing $\tilde{S} = S(\omega, b_1, \tau_1) + S(\omega, b_2, \tau_2)$, gives reasonable agreement with the data using parameters b_1 =5 kHz, τ_1 =1 μs, b_2 =180 kHz, τ_2 =1 ms [Fig. 5.7(d)]. The two drastically different set of noise parameters for each of the sources can help illuminate the source of noise in our devices.

As explained in the previous section, one likely candidate for this decoherence is a bath of free electrons arising from improper surface termination or local damage caused during nanofabrication, which are known to have correlation times in the ∼μs range. The SiV studied in this analysis is approximately equidistant from three surfaces: the two nearest holes which define the nanophotonic cavity, and the top surface of the nanobeam [sec: 5.2], all of which are approximately 50 nm away. We

estimate a density of $\sigma_{\mathrm{surf}} = 0.067$ spins/nm^2 using:

$$b_1 = \gamma_{\mathrm{SiV}} \langle B_{\mathrm{surf}} \rangle = \frac{\mathrm{g}^2 \mu_B^2 \mu_0}{\hbar} \frac{1}{4\pi \Sigma d_i^2} \sqrt{\frac{\pi}{4\sigma_{\mathrm{surf}}}} \tag{5.16}$$

where b_1 is the measured strength of the noise bath, g is the electron gyromagnetic ratio, and d_i are the distances to the nearest surfaces. This observation is consistent with surface spin densities measured using NVs[106].

The longer correlation time for the second noise term suggests a different bath, possibly arising from free electron spins inside the bulk diamond. Vacancy clusters, which can persist under annealing even at 1200 C, are known to posses $g = 2$ electron spins, and are one possible candidate for this noise bath[30]. Integrating over d in eq. 5.16, we estimate the density of spins required to achieve the measured b_2. We estimate $\rho_{\mathrm{bulk}} \sim 0.53$ spins per nm^3, which corresponds to a doping of 3ppm. Interestingly, this is nearly identical to the local concentration of silicon incorporated during implantation (most of which is not successfully converted into negatively charged SiV), and could imply implantation-related damage as a possible source of these impurities.

Another possible explanation for this slower bath could be coupling to nuclear spins in the environment. The diamond used in this experiment has a natural abundance of ^{13}C, a spin-1/2 isotope, in concentrations of approximately 1.1%. Replacing $\mu_B \rightarrow \mu_N$ in the term for $\langle B \rangle$ gives an estimated nuclear spin density of $\rho_{\mathrm{bulk,N}} = 0.6\%$, only a factor of two different than the expected nuclear spin density.

5.14 Concurrence and Fidelity calculations

5.14.1 Spin-photon concurrence and fidelity calculations

From correlations in the Z- and X-bases, we estimate a lower bound for the entanglement in our system. Following reference[144], we note that the density matrix of our system conditioned on the detection of one photon can be described as:

$$\rho_{ZZ} = 1/2 \begin{pmatrix} p_{e\uparrow} & 0 & 0 & 0 \\ 0 & p_{e\downarrow} & c_{e\downarrow,l\uparrow} & 0 \\ 0 & c^{\dagger}_{e\downarrow,l\uparrow} & p_{l\uparrow} & 0 \\ 0 & 0 & 0 & p_{l\downarrow} \end{pmatrix} \tag{5.17}$$

where p_{ij} are the probabilities of measuring a photon in state i, and the spin in state j. $c_{e\downarrow,l\uparrow}$ represents entanglement between $p_{e\uparrow}$ and $p_{l\downarrow}$. We set all other coherence terms to zero, as they represent negligibly small errors in our system (for example, $c_{e\uparrow,e\downarrow} > 0$ would imply that the SiV was not initialized properly at the start of the measurement). We quantify the degree of entanglement in the system by its concurrence $\mathcal{C}$, which is 0 for seperable states, and 1 for a maximally entangled state[145]:

$$\mathcal{C} = \mathrm{Max}(0, \lambda_0^{1/2} - \sum_{i=1}^{N} \lambda_i^{1/2}), \tag{5.18}$$

where λ_i are the eigenvalues of the matrix $\rho_{ZZ} \cdot \left(\sigma_y \cdot \rho_{ZZ} \cdot \sigma_y^{\dagger}\right)$, and σ_y is the standard Pauli matrix acting on each qubit basis separately ($\sigma_y = \sigma_{y,\mathrm{ph}} \otimes \sigma_{y,\mathrm{el}}$). While this can be solved exactly, the

resulting equation is complicated. Taking only the first-order terms, this can be simplified to put a lower bound on the concurrence:

$$\mathcal{C} \geq 2(|c_{e\downarrow,l\uparrow}| - \sqrt{p_{e\uparrow} p_{l\downarrow}}) \tag{5.19}$$

We measure p direcly in the Z basis, and estimate $|c_{e\downarrow,l\uparrow}|$ by performing measurements in the X basis. A $\pi/2$-rotation on both the photon and spin qubits rotates:

$$|e\rangle \rightarrow 1/\sqrt{2}(|e\rangle + |l\rangle), \quad |l\rangle \rightarrow 1/\sqrt{2}(|e\rangle - |l\rangle)$$

$$|\downarrow\rangle \rightarrow 1/\sqrt{2}(|\downarrow\rangle + |\uparrow\rangle), \quad |\uparrow\rangle \rightarrow 1/\sqrt{2}(|\downarrow\rangle - |\uparrow\rangle)$$

Afer this transformation, the signal contrast directly measures $c_{e\downarrow,l\uparrow}$:

$$2c_{e\downarrow,l\uparrow} = p_{-,\leftarrow} + p_{+,\rightarrow} - p_{-\rightarrow} - p_{+\leftarrow} \Rightarrow \mathcal{C} \geq 0.42(6) \tag{5.20}$$

Similarly, the fidelity of the entangled state (post-selected on the detection of a photon) can be computed by the overlap with the target Bell state[54]:

$$F = \langle \Psi^+ | \rho_{ZZ} | \Psi^+ \rangle = (p_{e\uparrow} + p_{l\downarrow} + 2c_{e\downarrow,l\uparrow})/2 \geq 0.70(3) \tag{5.21}$$

5.14.2 Correcting for readout infidelity

Errors arising from single-shot readout incorrectly assign the spin state, results in lower-contrast histograms for spin-photon correlations. We follow the analysis done in ref.[54], and correct for readout errors using a transfer matrix formalism. The measured spin-photon correlations p_{ij} are related to the 'true' populations P_{ij} via:

$$\begin{pmatrix} p_{e\downarrow} \\ p_{e\uparrow} \\ p_{l\downarrow} \\ p_{l\uparrow} \end{pmatrix} = \begin{pmatrix} F_\downarrow & 1-F_\uparrow & 0 & 0 \\ 1-F_\downarrow & F_\uparrow & 0 & 0 \\ 0 & 0 & F_\downarrow & 1-F_\uparrow \\ 0 & 0 & 1-F_\downarrow & F_\uparrow \end{pmatrix} \begin{pmatrix} P_{e\downarrow} \\ P_{e\uparrow} \\ P_{l\downarrow} \\ P_{l\uparrow} \end{pmatrix} \tag{5.22}$$

with $F_\downarrow$, $F_\uparrow$ defined above. After this correction, an identical analysis is performed to calculate the error-corrected histograms [Fig. 5.8(b,c,d) dark-shading]. We find an error-corrected concurrence $\mathcal{C} \geq 0.79(7)$ and fidelity $F \geq 0.89(3)$.

5.14.3 Electron-nuclear concurrence and fidelity calculations

For spin-spin Bell states, in contrast to the spin-photon analysis, we can no longer set any of the off-diagonal terms of the density matrix [eq. 5.17] to zero due to the limited ($\sim 90\%$) nuclear initialization fidelity. We note that neglecting these off-diagonal terms can only decrease the estimated entanglement in the system, thus the concurrence can still be written as:

$$\mathcal{C} \geq 2(|c_{\downarrow\uparrow}| - \sqrt{p_{\uparrow\uparrow}p_{\downarrow\downarrow}}) \tag{5.23}$$

where the first subscript is the electron spin state, and the second is the nuclear state. We estimate $c_{\downarrow\uparrow}$ again by using the measured populations in an orthogonal basis. In this case, off-diagonal terms add a correction:

$$2c_{\downarrow\uparrow} + 2c_{\uparrow\downarrow} = p_{\leftarrow\leftarrow} + p_{\rightarrow\rightarrow} - p_{\leftarrow\rightarrow} - p_{\rightarrow\leftarrow} \tag{5.24}$$

In order for the density matrix to be properly normalized, $c_{\uparrow\downarrow} \leq \sqrt{p_{\uparrow\uparrow}p_{\downarrow\downarrow}}$, giving us the final concurrence:

$$\mathcal{C} \geq p_{\leftarrow\leftarrow} + p_{\rightarrow\rightarrow} - p_{\leftarrow\rightarrow} - p_{\rightarrow\leftarrow} - 4\sqrt{p_{\uparrow\uparrow}p_{\downarrow\downarrow}} \tag{5.25}$$

Following this analysis, we report an error-corrected concurrence of $\mathcal{C} \geq 0.22(9)$.

5.14.4 Electron-nuclear CNOT gate

We further characterize the CNOT gate itself as a universal quantum gate. Due to the relatively poor readout fidelity (see above), we do not do this by performing quantum state tomography. Instead, we estimate entries in the CNOT matrix using measurements in only the Z-basis. As a control measurement, we first initialize the two qubits in all possible configurations and read out, averaged over many trials. Next, we initialize the qubits, perform a CNOT gate, and read out, again averaged over many

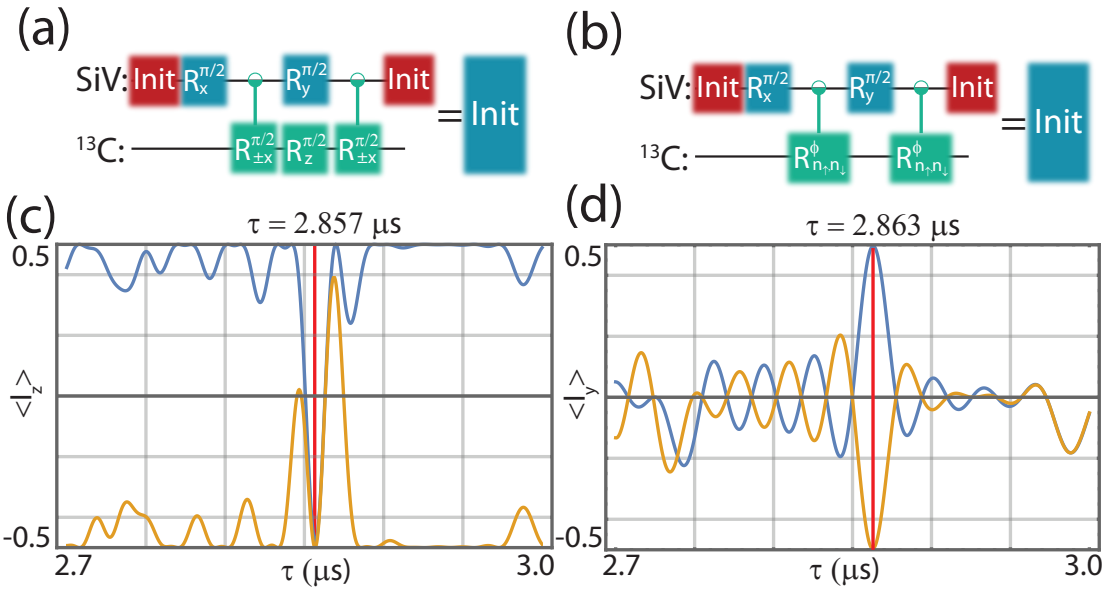


Figure 5.13: (a) Original initialization sequence from [108], note $\mathcal{R}_{z,\mathrm{C}}^{pi/2}$ rotation. (b) Simplified initialization sequence used in this work. (c) Simulated performance of the initialization gate from (b) using 8 $\pi-$pulses per each nuclear gate, the initial state is $|\uparrow\uparrow\rangle$ (blue) and $|\uparrow\downarrow\rangle$ (orange). The resonances are narrow compared to (d) due to applying effectively twice more $\pi-$pulses (d) Simulated performance of $\mathcal{R}_{\pm x,\mathrm{SiV}-\mathrm{C}}^{pi/2}$ gate for 8 $\pi-$pulses for SiV-^{13}C register initialized in $|\uparrow\uparrow\rangle$ (blue) and $|\downarrow\uparrow\rangle$ (orange)

trials, normalized by the control data. Any reduction in contrast after normalization is attributed to the opposite spin state, establishing a system of equations for determining the CNOT matrix. We solve this system of equations, marginalizing over free parameters to determine a MLE estimate for the CNOT transfer matrix, as seen in reference [22].

5.15 Nuclear initialization and readout

Initialization (and readout) of the ^{13}C spin can be done by mapping population between the SiV spin and the ^{13}C. Following reference [108], we note that Z and X gates are possible with dynamical-decoupling based nuclear gates, thus a natural choice for initialization are gates comprised of both

$\mathcal{R}^{pi/2}_{\pm x,\mathrm{SiV-C}}$ and $\mathcal{R}^{pi/2}_{z,\mathrm{SiV-C}}$, as shown in figure 5.13(a) and in reference[108]. We note here that it should be possible to combine the effects of $\mathcal{R}_x$ and $\mathcal{R}_z$ rotations in a single gate, which has the potential of shortening and simplifying the total initialzation gate. One proposed sequence uses the following entangling gate:

$$\mathcal{R}^{\phi}_{\vec{n_\uparrow},\vec{n_\downarrow}} = \begin{pmatrix} (1+i)/2 & i/\sqrt{2} & 0 & 0 \\ i/\sqrt{2} & (1-i)/\sqrt{2} & 0 & 0 \\ 0 & 0 & (1+i)/2 & -i/\sqrt{2} \\ 0 & 0 & -i/\sqrt{2} & (1-i)/2 \end{pmatrix} = \begin{pmatrix} R^{pi/2}_{\Theta=\pi/4} R^{pi/2}_z & 0 \\ 0 & R^{-pi/2}_{\Theta=\pi/4} R^{pi/2}_z \end{pmatrix} \quad (5.26)$$

which corresponds to a rotation on the angle $\phi = 2\pi/3$ around the axes $n_{\uparrow,\downarrow} = \{\pm\sqrt{2}, 0, 1\}/\sqrt{3}$. The matrix of entire initialization gate [Fig. 5.13(b)] built from this gate would then be:

$$\mathrm{Init} = \begin{pmatrix} 0 & 0 & -(1+i)/2 & -1/\sqrt{2} \\ i/\sqrt{2} & -(1+i)/2 & 0 & 0 \\ 0 & 0 & -(1-i)/2 & -i/\sqrt{2} \\ 1/\sqrt{2} & (1-i)/2 & 0 & 0 \end{pmatrix} \quad (5.27)$$

which results in an initialized ^{13}C spin.

To demonstrate this, we numerically simulate a MW pulse sequence using the exact coupling pa-

rameters of our ^{13}C[22] and 8 $\pi-$pulses for each $\mathcal{R}^{\phi}_{\vec{n_\uparrow},\vec{n_\downarrow}}$ gate. Figure 5.13(c) shows that regardless of the initial state, the ^{13}C always ends up in state $|\downarrow\rangle$ (given that the SiV was initialized in $|\uparrow\rangle$). As expected, the timing of this gate ($\tau_{\text{init}} = 2.857\,\mu$s) is noticeably different from the timing of the $\mathcal{R}^{\pi/2}_{\pm x,\text{SiV}-\text{C}}$ gate ($\tau_{\pi/2} = 2.851\,\mu$s), which occurs at spin-echo resonances [Fig. 5.13(d)].

The rotation matrix for this sequence at $\tau = \tau_{\text{init}}$ (with the SiV initialized in $|\uparrow\rangle$) is:

$$\mathcal{R}^{\phi}_{n_\uparrow} = \begin{pmatrix} 0.55 + 0.51i & 0 + 0.65i \\ 0.65i & 0.55 - 0.52i \end{pmatrix} \tag{5.28}$$

corresponding to a rotation angle $\phi = 0.63\pi$ around the axis $n_\uparrow = \{0.78, 0, 0.62\}$, very close to the theoretical result.

Since the experimental fidelities for both initialization gates [Fig. 5.13 (a,b)] are similar, we use sequence (b) to make the gate shorter and avoid unnecessary pulse-errors.

5.16 Conclusion

The SiV center in diamond has rapidly become a leading candidate to serve as the building block of a future quantum network. In this work, we describe the underlying technical procedures and optimal parameter regimes necessary for utilizing the SiV-nanocavity system as a quantum network node. In particular, we discuss the effect of static and dynamic strain on the properties of the SiV spin qubit and its optical interface, with direct application to quantum networking experiments. We demonstrate techniques for coherently controlling and interfacing SiV spin qubits inside of nanophotonic

structures at millikelvin temperatures to optical photons. Finally, we identify and coherently control auxiliary nuclear spins, forming a nanophotonic two-qubit register.

The work presented here and in the complementary section above illustrates the path towards the realization of a first-generation quantum repeater based on SiV centers inside diamond nanodevices. We note that a key ingredient enabling future, large-scale experiments involving several solid-state SiV-nanocavity nodes will be the incorporation of strain tuning onto each device[112]. Precise tuning of both the static and dynamic strain can overcome the limitations of inhomogeneous broadening and spectral diffusion, and enable scalable fabrication of quantum repeater nodes [Sec. 5.4].

6

Experimental Demonstration of Memory Enhanced Quantum Communication

The last decade has seen a great deal of progress in the development of quantum networking technology, including the demonstration of many of the components of the so called quantum repeater protocol. This protocol is the fundamental component of a long distance quantum network, enabling

the transmission of quantum information over networks that would otherwise be limited by photon loss. In brief, this protocol consists of mapping information transmitted via photons between network nodes onto a quantum memory, performing bell state measurements between two photons stored in this manner to entangle adjacent network nodes, and then repeating the process to purify the fidelity of the generated entangled state and extend the range of the network. By doing this, high fidelity entangled states can be generated between any two nodes of the quantum network with sub exponential scaling of the required resources.

Many systems have demonstrated the capacity to implement individual steps of this procedure. High fidelity spin photon entanglement and photon storage in particular has been realized with a large variety of systems, and entanglement between quantum memories located inside the same network node has also been repeatedly demonstrated. A smaller number of systems have been used to demonstrate entanglement purification, but among these some have managed to do so at a rate sufficiently fast to overcome the decoherence of the system. As such, the field of quantum networking no longer seeks to implement these individual components, but instead seeks combine them into a single system and, moreover, do so in a manner that is technologically beneficial.

This last element is perhaps the most challenging to realize. While the quantum repeater protocol in principle provides a route towards enhancement of quantum communication rates over long distances, doing so in practice is extremely challenging due to losses and infidelities introduced during experimental implementation of the technology. In other words, while many systems have been able to demonstrate components of the quantum repeater protocol, few have been able to do so with the levels of fidelity and efficiency that utilizing the proposed quantum network nodes offers any true

benefit for communicating parties.

The natural frame of reference for deciding whether or not the network node is beneficial to use is through comparison to "direct transmission" quantum communication. In this case two communicating parties attempt to communicate via photons sent by one communicating party and measured by the other. This process has the advantage that it, in principle, has no baseline communication infidelity, but is limited by the fact that photons lost from the system can not be recovered. As such, this method of communication experiences exponential fall of in communication rate as the distance (and thus loss) between the two parties increases. If a system can demonstrate that two parties would, over some distance, prefer to communicate by utilizing the quantum network node to attempting direct transmission then the quantum network node is able to offer useful technological advantage. The work presented here represents the first known demonstration of a system that offer such advantage for two theoretical parties communicating over a long distance, representing a key step towards the creation of a useful quantum network node.

6.1 Introduction

Efficient, long-lived quantum memory nodes are expected to play an essential role in extending the range of quantum communication[10], as they enable asynchronous quantum logic operations, such as Bell-state measurements (BSM), between optical photons. Such an asynchronous BSM is central to many quantum communication protocols, including the realization of scalable quantum repeaters[10] with multiple intermediate nodes. Its elementary operation can be understood by considering a spe-

cific implementation of quantum cryptography[146,147] illustrated in Fig. 6.1a. Here two remote communicating parties, Alice and Bob, try to agree on a key that is secure against potential eavesdroppers. They each send a randomly chosen photonic qubit $\{|\pm x\rangle, |\pm y\rangle\}$ encoded in one of two conjugate bases (X or Y) across a lossy channel to an untrusted central node (Charlie), who performs a BSM and reports the result over an authenticated public channel. After a number of iterations, Alice and Bob publicly reveal their choice of bases to obtain a correlated bit string (sifted key) from the cases when they used a compatible basis. A potentially secure key can subsequently be distilled provided the BSM error rate is low enough.

6.2 Fundamental limit of direct transmission

While a photonic BSM can be implemented with linear optics and single photon detectors, in this "direct-transmission" approach, the BSM is only successful when photons from Alice and Bob arrive simultaneously. Thus, when Alice and Bob are separated by a lossy fiber with a total transmission probability $p_{\mathrm{A}\to\mathrm{B}} \ll 1$, Charlie measures photon coincidences with probability also limited by $p_{\mathrm{A}\to\mathrm{B}}$, leading to a fundamental bound[148] on the maximum possible distilled key rate of $R_{\max} = p_{\mathrm{A}\to\mathrm{B}}/2$ bits per channel use for an unbiased basis choice[149]. While linear optical techniques to circumvent this bound are now being actively explored[150], they offer only limited improvement and cannot be scaled beyond a single intermediate node.

Alternatively, this bound can be surpassed using a quantum memory node at Charlie's location. In this approach, illustrated in Fig. 6.1b, the state of Alice's photon is stored in the heralded memory

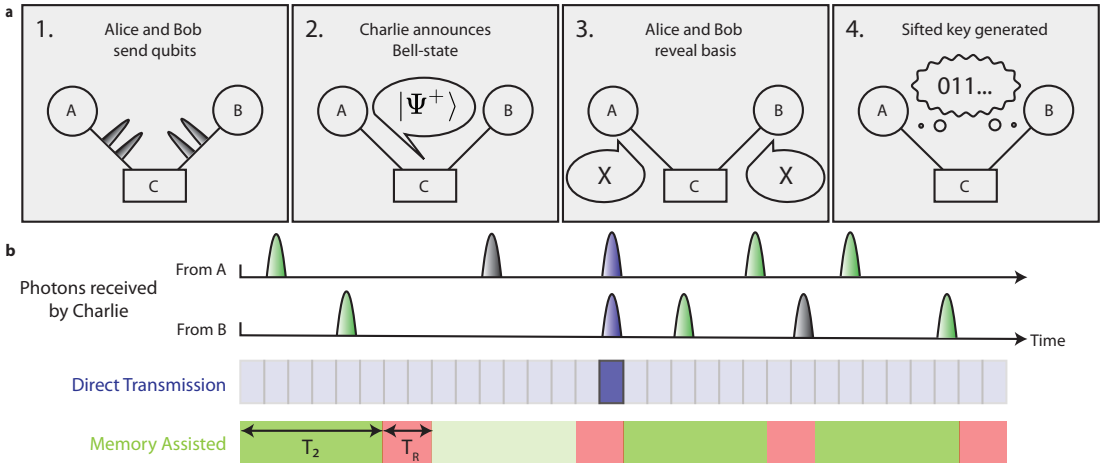


Figure 6.1: Concept of memory-enhanced quantum communication. a, Quantum communication protocol. Alice and Bob send qubits encoded in photons to a measurement device (Charlie) in between them. Charlie performs a BSM and announces the result. After verifying which rounds Alice and Bob sent qubits in compatible bases, a sifted key is generated. b, Illustration of memory-enhanced protocol. Photons arrive at Charlie from A and B at random times over a lossy channel, and are unlikely to arrive simultaneously (indicated in purple), leading to a low BSM success rate for direct transmission. Despite overhead time T_R associated with operating a quantum memory (red), a BSM can be performed between photons that arrive at Charlie within memory coherence time T_2, leading to higher success rates (green). BSM successes and failures are denoted by dark and light shaded windows respectively for both approaches.

while awaiting receipt of Bob's photon over the lossy channel. Once the second photon arrives, a BSM between Alice's and Bob's qubits yields a distilled key rate that for an ideal memory scales as[151] $R_s \propto \sqrt{p_{\mathrm{A}\to\mathrm{B}}}$, potentially leading to substantial improvement over direct transmission.

6.3 Efficient nanophotonic quantum node

In this work we realize and use a quantum node that enables BSM rates exceeding those of an ideal system based on linear optics. We focus on the demonstration and characterization of the BSM node, leaving the implementation of source-specific technical components of full-scale QKD systems, such as decoy states[152], basis biasing[153], a finite key error analysis[154], and a physical separation of Alice and Bob for future work. Our realization is based on a single silicon-vacancy (SiV) color-center integrated inside a diamond nanophotonic cavity[70,40,22] (Fig. 6.2a). Its key figure-of-merit, the cooperativity[11] C, describes the ratio of the interaction rate with individual cavity photons compared to all dissipation rates. A low mode volume ($0.5(\lambda/n)^3$), high quality factor (2×10^4), and nanoscale positioning of SiV centers enable an exceptional $C = 105 \pm 11$. Cavity photons at 737 nm are critically coupled to a waveguide and adiabatically transferred into a single-mode optical fiber[40] that is routed to superconducting nanowire single-photon detectors, yielding a full system detection efficiency of about 85% (Methods). The device is placed inside a dilution refrigerator, resulting in electronic spin quantum memory[22] time $T_2 > 0.2$ ms at temperatures below 300 mK.

The operating principle of the SiV-cavity based spin-photon interface is illustrated in Fig. 6.2. Spin dependent modulation of the cavity reflection at incident probe frequency f_0 (Fig. 6.2b) results in

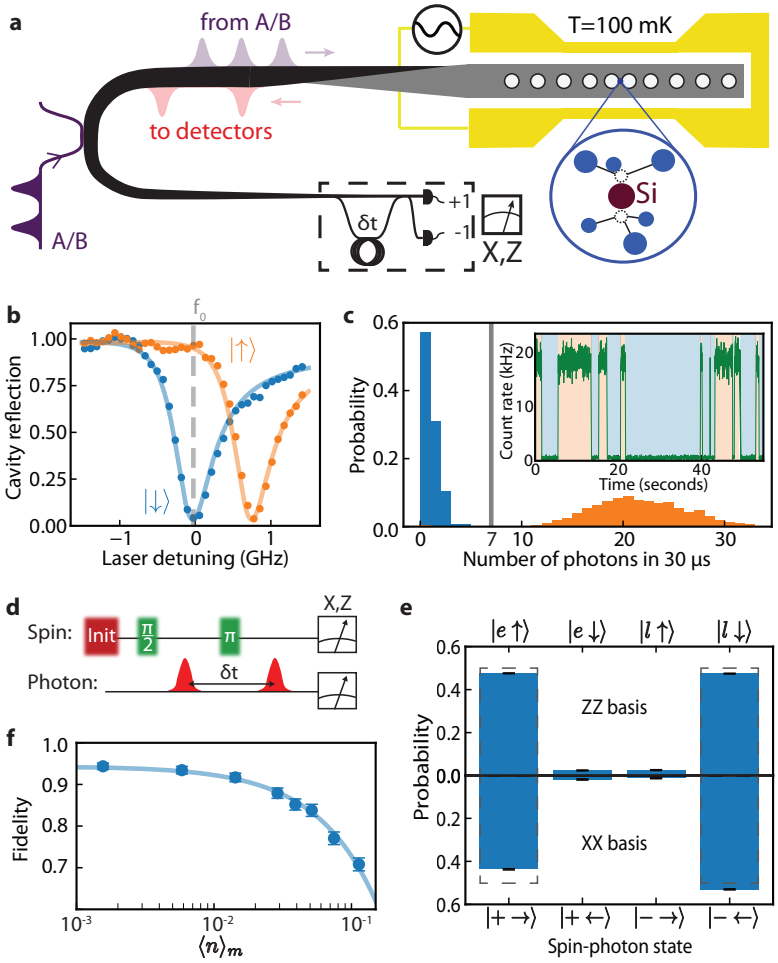


Figure 6.2: Realization of heralded spin-photon gate. a, Schematic of memory-assisted implementation of Charlie's measurement device. Weak pulses derived from a single laser simulate incoming photons from Alice and Bob (purple). Reflected photons (red) are detected in a heralding setup (dashed box). b, Reflection spectrum of memory node, showing spin-dependent device reflectivity. c, Histogram of detected photon numbers during a $30\,\mu s$ laser pulse, enabling single-shot readout based on a threshold of 7 photons. (Inset) Electron spin quantum jumps under weak illumination. d, Schematic of spin-photon quantum logic operation used to generate and verify spin-photon entangled state. e, Characterization of resulting spin-photon correlations in the ZZ and XX bases. Dashed bars show ideal values. f, Measured spin-photon entanglement fidelity as a function of $\langle n \rangle_m$, the average incident photon number during each initialization of the memory. All error bars represent 1 standard deviation.

the direct observation of electron spin quantum jumps (Fig. 6.2c, inset), enabling nondestructive single-shot readout of the spin state (Fig. 6.2c) in 30 μs with fidelity $F = 0.9998^{+0.0002}_{-0.0003}$. Coherent control of the SiV spin qubit ($f_Q \approx 12$ GHz) is accomplished using microwave fields delivered via an on-chip gold coplanar waveguide[22]. We utilize both optical readout and microwave control to perform projective feedback-based initialization of the SiV spin into the $|\downarrow\rangle$ state with a fidelity of $F = 0.998 \pm 0.001$. Spin-dependent cavity reflection also enables quantum logic operations between an incoming photonic time-bin qubit, defined by a phase-coherent pair of attenuated laser pulses, and the spin memory[22,138]. We characterize this by using the protocol illustrated in Fig. 6.2d to generate the spin-photon entangled state $(|e\uparrow\rangle + |l\downarrow\rangle)/\sqrt{2}$ conditioned on successful reflection of an incoming single photon with overall heralding efficiency $\eta = 0.423 \pm 0.004$ (Methods). Here, $|e\rangle$ and $|l\rangle$ denote the presence of a photon in an early or late time-bin separated by $\delta t = 142$ ns respectively. We characterize the entangled state by performing measurements in the joint spin-photon ZZ and XX bases (Fig. 6.2e), implementing local operations on the reflected photonic qubit with a time-delay interferometer (Fig. 6.2a, dashed box). By lowering the average number of photons $\langle n|n\rangle_m$ incident on the device during the SiV memory time, we reduce the possibility that an additional photon reaches the cavity without being subsequently detected, enabling high spin-photon gate fidelities for small $\langle n|n\rangle_m$ (Fig. 6.2f). For $\langle n\rangle_m = 0.002$ we measure a lower bound on the fidelity[22] of the spin-photon entangled state of $F \geq 0.944 \pm 0.008$, primarily limited by residual reflections from the $|\downarrow\rangle$ state.

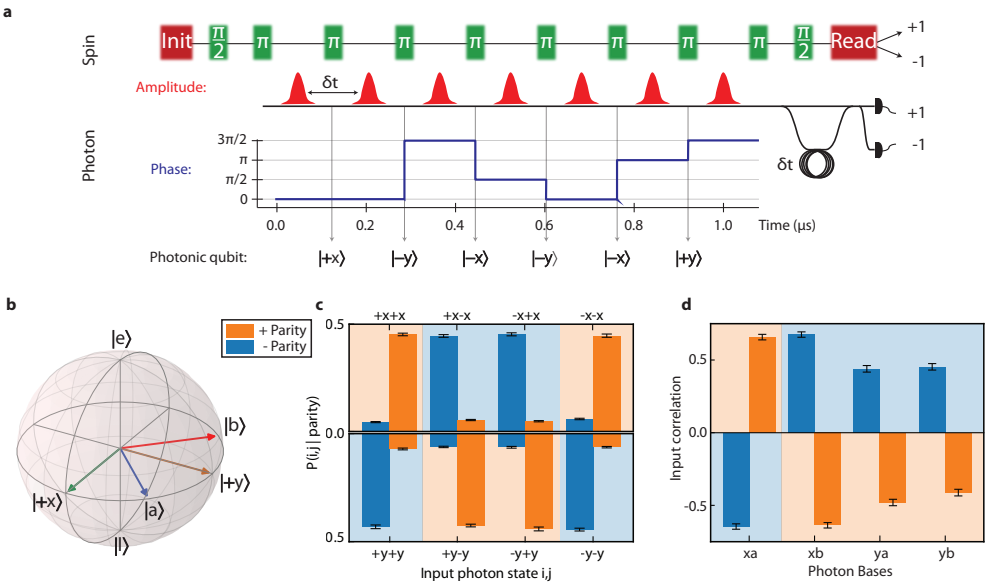


Figure 6.3: Asynchronous Bell-state measurements using quantum memory. a, Example sequence with $N = 6$ photonic qubits sent in a single memory time. Microwave π pulses (green) are interleaved with incoming optical pulses. Photons have fixed amplitude (red) and qubits are defined by the relative phases between subsequent pulses (blue). b, Bloch sphere representation of input photonic time-bin qubits used for characterization. c, Characterization of asynchronous BSM. Conditional probabilities for Alice and Bob to have sent input states (i, j) given a particular parity outcome for input states in the X (top) and Y (bottom) bases. d, Bell test using the CHSH inequality. Conditioned on the BSM outcome, the average correlation between input photons is plotted for each pair of bases used (Appendix A). Shaded backgrounds denote the expected parity. All error bars represent 1 standard deviation.

6.4 Asynchronous Bell-state measurements

This spin-photon logic gate can be directly used to herald the storage of an incoming photonic qubit by interferometrically measuring the reflected photon in the X basis[22]. To implement a memory-assisted BSM, we extend this protocol to accommodate a total of N photonic qubit time-bins within a single initialization of the memory (Fig. 6.3a). Each individual time-bin qubit is encoded in the relative amplitudes and phases of a pair of neighboring pulses separated by δt. Detection of a reflected photon heralds the arrival of the photonic qubit formed by the two interfering pulses without revealing its

state[22]. Two such heralding events, combined with subsequent spin-state readout in the X basis, constitute a successful BSM on the incident photons. This can be understood without loss of generality by restricting input photonic states to be encoded in the relative phase ϕ between neighboring pulses with equal amplitude: $(|e\rangle + e^{i\phi}|l\rangle)/\sqrt{2}$ (Fig. 6.3b). Detection of the first reflected photon in the X basis teleports its quantum state onto the spin, resulting in the state $(|\uparrow\rangle + m_1 e^{i\phi_1}|\downarrow\rangle)/\sqrt{2}$, where $m_1 = \pm 1$ depending on which detector registers the photon[22]. Detection of a second photon at a later time within the electron spin T_2 results in the spin state $(|\uparrow\rangle + m_1 m_2 e^{i(\phi_1+\phi_2)}|\downarrow\rangle)/\sqrt{2}$. The phase of this spin state depends only on the sum of the incoming phases and the product of their detection outcomes, but not the individual phases themselves. As a result, if the photons were sent with phases that meet the condition $\phi_1 + \phi_2 \in \{0, \pi\}$, a final measurement of the spin in the X basis ($m_3 = \pm 1$) completes an asynchronous BSM, distinguishing two of the four Bell-states based on the total parity $m_1 m_2 m_3 = \pm 1$ (Appendix A).

This approach can be directly applied to generate a correlated bit-string within the protocol illustrated in Fig. 6.1a. We analyze the system performance by characterizing the overall quantum-bit error rate (QBER)[149,146] for $N = 124$ photonic qubits per memory initialization. We use several random bit strings of incoming photons from $\{|\pm x\rangle, |\pm y\rangle\}$ and observe strong correlations between the resulting BSM outcome and the initial combination of input qubits for both bases (Fig. 6.3c). Using this method, we estimate the average QBER to be $E = 0.116 \pm 0.002$ for all combinations of random bit strings measured, significantly below the limit of $E_i = 0.146$, which could provide security against individual attacks[149] (note that the measured error rate is also well below the minimum average QBER[146] of $E_{lo} = 0.125$ achievable using a linear optics BSM with weak coherent pulse inputs,

see Appendix A). In our experiment, the QBER is affected by technical imperfections in the preparation of random strings of photonic qubits. We find specific periodic patterns of photonic qubits to be less prone to these effects, resulting in a QBER as low as $E = 0.097 \pm 0.006$, which falls within the threshold corresponding to unconditional security[12] of $E_u = 0.110$ with a confidence level of 0.986 (Appendix A). We further verify security by testing the Bell-CHSH inequality[35] using input states from four different bases, each separated by an angle of $45°$ (Appendix A). We find that the correlations between input photons (Fig. 6.3d) violate the Bell-CHSH inequality $S_\pm \leq 2$, observing $S_+ = 2.21 \pm 0.04$ and $S_- = 2.19 \pm 0.04$ for positive and negative BSM parity results respectively. This result demonstrates that this device can be used for quantum communication that is secured by Bell's theorem.

6.5 Benchmarking quantum memory advantage

In order to benchmark the performance of memory-assisted quantum communication, we model an effective channel loss by reducing the mean photon number $\langle n|n\rangle_p$ incident on the device per photonic qubit. Assuming that Alice and Bob emit roughly one photon per qubit, this yields an effective channel transmission probability $p_{A\to B} = \langle n|n\rangle_p^2$, resulting in the maximal distilled key rate R_{max} per channel use for the direct transmission approach[146], given by the red line in Fig. 6.4. We emphasize that this is a theoretical upper bound for a linear optics based BSM, assuming ideal single-photon sources and detectors and balanced basis choices. The measured sifted key rates of the memory-based device are plotted as open circles in Fig. 6.4. Due to the high overall heralding efficiency and the large

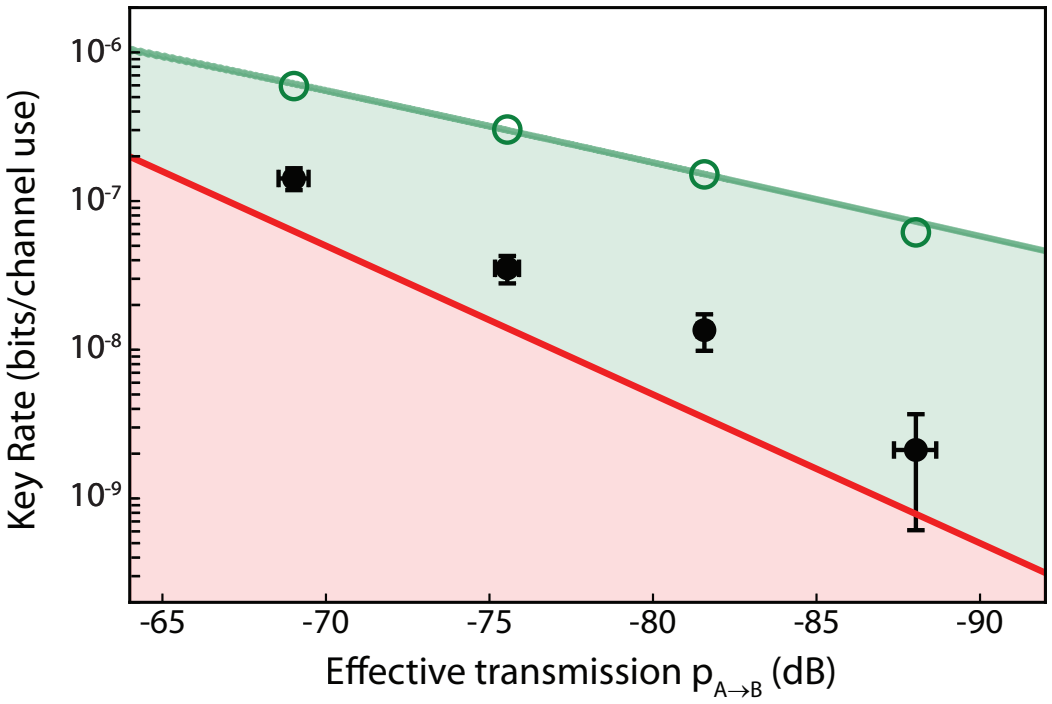


Figure 6.4: Performance of memory-assisted quantum communication. Log-log plot of key rate in bits per channel use versus effective channel transmission ($p_{\mathrm{A}\to\mathrm{B}} = \langle n|n\rangle_p^2$, where $\langle n|n\rangle_p$ is the average number of photons incident on the measurement device per photonic qubit). Red line: theoretical maximum for loss-equivalent direct transmission experiment. Green open circles: experimentally measured sifted key rate (green line is the expected rate). To ensure optimal operation of the memory, $\langle n|n\rangle_m = \langle n|n\rangle_p N \approx 0.02$ is kept constant (Methods). From left to right, points correspond to $N = \{60, 124, 248, 504\}$. Black filled circles: distilled key rates R_S using memory device. Vertical error bars are given by the 68% confidence interval and horizontal error bars represent the standard deviation of the systematic power fluctuations.

number of photonic qubits per memory time (up to $N = 504$), the memory-assisted sifted key rate exceeds the capability of a linear-optics based BSM device by a factor of 78.4 ± 0.7 at an effective channel loss of about 88 dB.

In practice, errors introduced by the quantum memory node could leak information to the environment, reducing the quality and potential security of the sifted key[12]. A shorter secure key can be recovered from a sifted key with finite QBER using classical error correction and privacy amplification techniques. The fraction of distilled bits r_s that can be secure against individual attacks rapidly diminishes[149] as the QBER approaches $E_i = 0.147$. For each value of the effective channel loss, we estimate the QBER and use it to compute r_s, enabling extraction of distilled key rates R_S, plotted in black in Fig. 6.4. Even after error-correction, we find that the memory-assisted distilled key rate outperforms the ideal limit for the corresponding direct-transmission implementation by a factor of up to $R_S/R_{\text{max}} = 4.1 \pm 0.5$ (± 0.1 systematic uncertainty, for $N = 124$). We further find that this rate also exceeds the fundamental bound on repeaterless communication[148] $R_S \leq 1.44 p_{A \to B}$ with a statistical confidence level of 99.2% ($^{+0.2\%}_{-0.3\%}$ systematic uncertainty, see Methods). Despite experimental overhead time associated with operating the device (T_R in Fig. 6.1b), the performance of the memory-assisted BSM node (for $N = 248$) is competitive with an ideal unassisted system running at a 4 MHz average clock rate (Methods).

6.6 Outlook

These experiments demonstrate a form of quantum advantage allowed by memory-based communication nodes and represent a crucial step towards realizing functional quantum repeaters. Several important technical improvements will be necessary to apply this advance for practical long-distance quantum communication. First, this protocol must be implemented using truly independent, distant communicating parties. Additionally, frequency conversion from telecommunications wavelengths to 737 nm, as well as low-loss optical elements used for routing photons to and from the memory node, will need to be incorporated. Finally, rapid generation of provably secure keys will require implementation of decoy-state protocols[152], biased bases[153], and finite-key error analyses[154], all compatible with the present approach. With these improvements, our approach is well-suited for deployment in real-world settings. It does not require phase stabilization of long-distance links and operates efficiently in the relevant regime of $p_{A\to B} \approx 70$ dB, corresponding to about 350 km of telecommunications fiber. Additionally, a single device can be used at the center of a star network topology[155], enabling quantum communication between several parties beyond the metropolitan scale.

Furthermore, the present approach can be extended along several directions. The use of long-lived ^{13}C nuclear spin qubits could eliminate the need to operate at low total $\langle n|n\rangle_m$ and would provide longer storage times, potentially enabling hundred-fold enhancement of BSM success rates[37,22]. Recently implemented strain-tuning capabilities[24] should allow for operation of many quantum nodes at a common network frequency. Unlike linear-optics based alternatives[150], the approach presented here can be extended to implement the full repeater protocol, enabling a polynomial scaling of the com-

munication rate with distance[10]. Finally, the demonstrated multi-photon gate operations can also be adapted to engineer large cluster-states of entangled photons[156], which can be utilized for rapid quantum communication[157]. Implementation of these techniques could enable the realization and applications of scalable quantum networks[5] beyond QKD, ranging from non-local quantum metrology[158] to modular quantum computing architectures[89].

7

Conclusion

The previous sections have documented the impressive progress of the SiV-photonics platform over the last 5 years, culminating in the benchmark demonstration of memory enhanced quantum communication. This demonstration represents the realization of a decades old goal of the quantum optics community and establishes the SiV as a leading platform for quantum networking. The obvious question is what steps this platform needs to take before it can be commercially deployed. Fortunately our

work over the last decade has positioned us well to answer this question.

Scientifically, the core remaining requirements for the SiV platform is implementation of the full quantum repeater protocol. This requires the ability to utilize ancillary quantum memories for entanglement purification, as well as the deployment of a scheme for entangling two spatially separated SiV centers. Work towards both of these goals is well underway, as unpublished results suggest that efficient interfaces between the SiV and the ^{29}Si nucleus can be easily realized and that application of frequency shifts from an EOM can be used to entangle two SiVs with slightly different optical frequencies. Upon finalization these results will in principle enable the full implementation of the quantum repeater protocol. Practically, this implementation is facilitated by the construction of a second dilution fridge setup in a laboratory neighboring the one utilized for the previous experimental results and the continued improvement of nanofabrication techniques. As such the implementation of this protocol should be on the horizon.

From an engineering standpoint the picture is slightly more complicated. Current techniques have been optimized to enable the use of only a single device inside each dilution fridge. Furthermore, fabrication and signal routing techniques are also optimized for these small systems. While the fabrication has long ago left the "hero device" regime in which many quantum systems operate, it is also not sufficiently deterministic to enable large scale creation of many nominally identical cavity devices. This problem is exacerbated by the fact that the fiber coupling technique used to extract photons, as well as the microwave photon delivery techniques currently in use, can not scale easily to larger systems. As such permanent optical and electronic packaging techniques will need to be borrowed from the classical photonics industry, or even developed independently. Finally, demonstrating gain from the

use of a quantum repeater protocol is dramatically simplified when an efficient, on demand entangled photon source is available at the appropriate wavelength for the SiV, something which is currently not commercially produced.

Solutions are already being explored for each of these problems, but will require substantial engineering efforts that are not well suited to academic environments. As such, investment into these technologies will require not only substantial funding, but also potentially a deviation from the largely academic priorities that have so far driven the field.

Reducing the costs of deploying this technology represents yet another important area for future research. Currently, devices are fabricated on large, purified diamond substrates that are difficult and expensive to produce. Experiments need to be conducted below 300 mK, and thus require the acquisition of dilution fridge units that are currently extremely costly. And, of course, nanofabrication of the diamond devices relies on the use of electron beam lithography tools with resolutions that can not be reached using conventional photolithography techniques. Resolving each of these problems will require a great deal of creativity and a scale of funding that is currently not available to academic researchers.

From this perspective, the short term introduction of industrial research and development efforts to the problem of quantum networking would be immensely beneficial for the field as a whole. Many of the problems discussed in the previous section are not unique to the SiV. As such, resolution of these problems for any one platform would improve the probability of success for all other quantum networking platforms.

A

Supporting Information for Chapter 6

The following section contains supporting information describing the experiments discussed in chapter 5 of the main text, hereafter refereed to as the ”main text” for this section of the document.

A.1 Characterization of the nanophotonic quantum memory.

A spectrum of the SiV-cavity system at large detuning (248 GHz) allows us to measure the cavity linewidth $\kappa = 21.6 \pm 1.3$ GHz, (Fig. A.2a, blue curve) and natural SiV linewidth $\gamma = 0.123 \pm 0.010$ GHz (Fig. A.2a, red curve). We find spectral diffusion of the SiV optical frequency to be much smaller than γ on minute timescales with an excitation photon flux of less than 1 MHz. Next, we estimate the single-photon Rabi frequency, g, using the cavity reflection spectrum for zero atom-cavity detuning, shown in red in Fig. A.2a. For a resonant atom-cavity system probed in reflection from a single port with cavity-waveguide coupling κ_{wg}, the cavity reflection coefficient[11] as a function of probe detuning Δ_c is given by

$$r(\Delta_c) = \frac{i\Delta_c + \frac{g^2}{i\Delta_c + \frac{\gamma}{2}} - \kappa_{wg} + \frac{\kappa}{2}}{i\Delta_c + \frac{g^2}{i\Delta_c + \frac{\gamma}{2}} + \frac{\kappa}{2}}. \tag{A.1}$$

By fitting $|r(\Delta_c)|^2$ using known values of κ and γ, we obtain the solid red curve in Fig. A.2a which corresponds to a single-photon Rabi frequency $g = 8.38 \pm 0.05$ GHz, yielding the estimated cooperativity $C = \frac{4g^2}{\kappa\gamma} = 105 \pm 11$.

A.2 Microwave control

We use resonant MW pulses delivered via an on-chip coplanar waveguide (CWG) to coherently control the quantum memory[22,23]. First, we measure the spectrum of the spin-qubit transition by applying a weak, 10 μs-long microwave pulse of variable frequency, observing the optically-detected magnetic

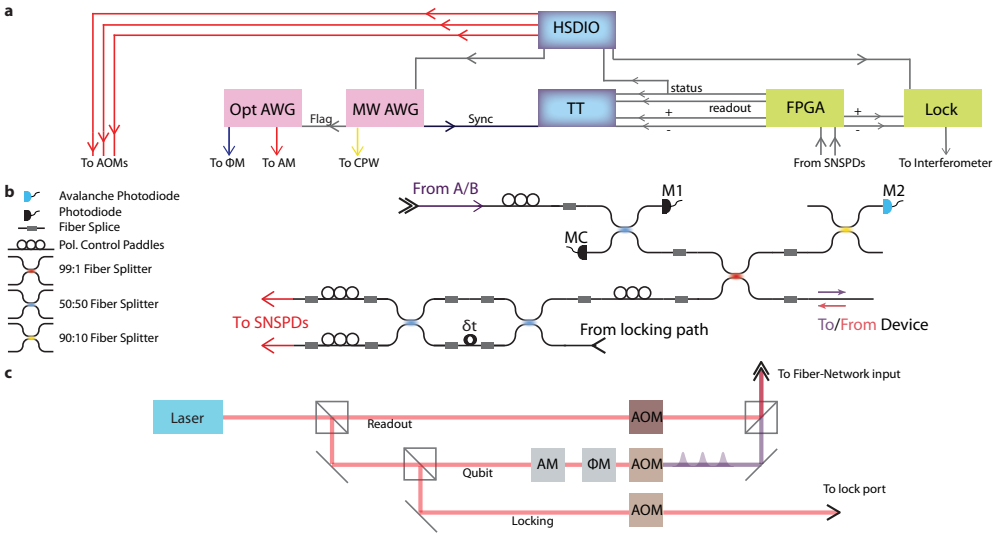


Figure A.1: Experimental schematic. a, Control flow of experiment. Opt (MW) AWG is a Tektronix AWG7122B $5\,\mathrm{GS/s}$ (Tektronix AWG70001a $50\,\mathrm{GS/s}$) arbitrary waveform generator used to generate photonic qubits (microwave control signals). All signals are recorded on a time-tagger (TT, PicoQuant HydraHarp 400). b, Fiber network used to deliver photons to and collect photons from the memory device, including elements for polarization control and diagnostic measurements of coupling efficiencies. c, Preparation of optical fields. The desired phase relation between lock and qubit paths is ensured by modulating AOMs using phase-locked RF sources with a precise $1.8\,\mathrm{MHz}$ frequency shift between them.

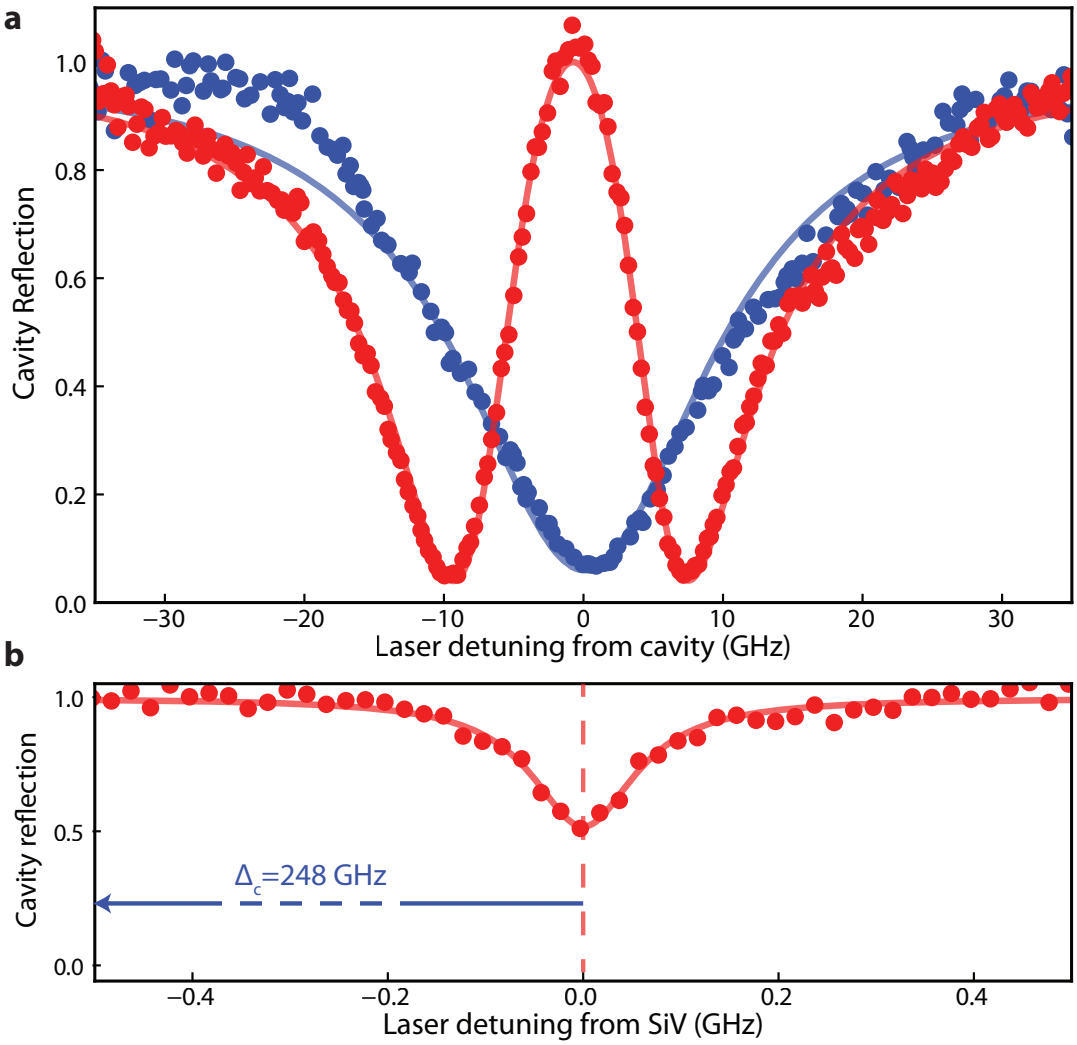


Figure A.2: Characterization of device cooperativity. a, Cavity reflection spectrum far-detuned (blue) and on resonance (red) with SiV center. Blue solid line is a fit to a Lorentzian, enabling extraction of linewidth $\kappa = 21.8\,\mathrm{GHz}$. Red solid line is a fit to a model used to determine the single-photon Rabi frequency $g = 8.38 \pm 0.05\,\mathrm{GHz}$ and shows the onset of a normal mode splitting. b, Measurement of SiV linewidth far detuned ($\Delta_c = 248\,\mathrm{GHz}$) from cavity resonance. Red solid line is a fit to a Lorentzian, enabling extraction of natural linewidth $\gamma = 0.123\,\mathrm{GHz}$.

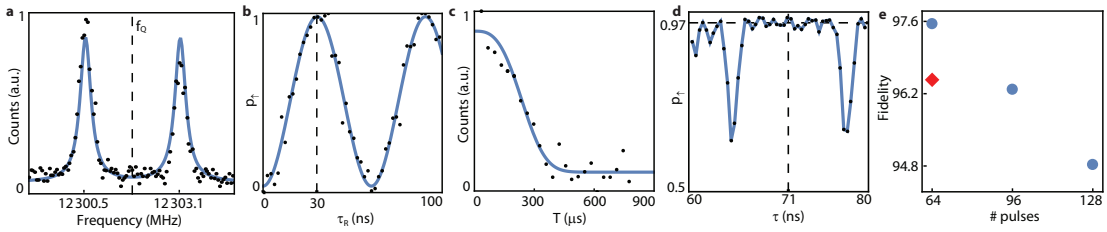


Figure A.3: Microwave characterization of spin-coherence properties. a, ODMR spectrum of the qubit transition at $\sim 12\,\mathrm{GHz}$ split by coupling to a nearby 13^C. b, Rabi oscillations showing π time of $30\,\mathrm{ns}$. A π time of $32\,\mathrm{ns}$ is used for experiments in the main text. c, XY8-1 dynamical decoupling signal (unnormalized) as a function of total time T, showing coherence lasting on the several hundred $\mu\mathrm{s}$ timescale. d, XY8-8 dynamical decoupling signal (normalized) revealing region of high fidelity at relevant value of $2\tau = 142\,\mathrm{ns}$. e, Fidelity of spin state after dynamical decoupling sequence with varying number of π pulses (N_π), blue points. Red point (diamond) is under illumination with $\langle n|n\rangle_m = 0.02$.

resonance (ODMR) spectrum presented in Fig. A.3a. We note that the spin-qubit transition is split by the presence of a nearby ^{13}C. While coherent control techniques can be employed to utilize the ^{13}C as an additional qubit [22,23], we do not control or initialize it in this experiment. Instead, we drive the electron spin with strong microwave pulses at a frequency f_Q such that both ^{13}C-state-specific transitions are addressed equally. This also mitigates slow spectral diffusion of the microwave transition [23] of $\sim$ 100 kHz.

After fixing the MW frequency at f_Q we vary the length of this drive pulse (τ_R in Fig. A.3b) and observe full-contrast Rabi oscillations. We choose a π time of $32\,\mathrm{ns}$ in the experiments in the main text, which is a compromise of two factors: (1) it is sufficiently fast such that we can temporally multiplex between 2 and 4 time-bin qubits around each microwave π pulse and (2) it is sufficiently weak to minimize heating related effects from high microwave currents in resistive gold CWG.

With known π time we measure the coherence time of the SiV spin qubit under an XY8-1 dynamical decoupling sequence to exceed $200\,\mu\mathrm{s}$ (Fig. A.3c). In the main experiment we use decoupling sequences with more π pulses. As an example, Fig. A.3d shows the population in the $|\uparrow\rangle$ state after

XY8-8 decoupling sequence (total $N_\pi = 64\ \pi$ pulses) as a function of τ, half of the inter-pulse spacing. For BSM experiments, this inter-pulse spacing, 2τ, is fixed and is matched to the time-bin interval δt. While at some times (e.g. $\tau = 64.5\,\mathrm{ns}$) there is a loss of coherence due to entanglement with the nearby $^{13}\mathrm{C}$, at $2\tau = 142\,\mathrm{ns}$ we are decoupled from this $^{13}\mathrm{C}$ and can maintain a high degree of spin coherence. Thus we chose the time-bin spacing to be $142\,\mathrm{ns}$. The spin coherence at $2\tau = 142\,\mathrm{ns}$ is plotted as a function N_π in Fig. A.3d, and decreases for large N_π, primarily due to heating related effects[22].

A.3 Fiber network.

The schematic of the fiber-network used to deliver optical pulses to and collect reflected photons from the nanophotonic memory device is shown in Fig. A.1b. Photons are routed through the lossy (1%) port of a 99:1 fiber beamsplitter (FBS) to the nanophotonic device. We note that for practical implementation of memory-assisted quantum communication, an efficient optical switch or circulator should be used instead. In this experiment, since we focus on benchmarking the performance of the memory device itself, the loss introduced by this beamsplitter is incorporated into the estimated channel loss. Reflected photons are collected and routed back through the efficient (99%) port of the FBS and are sent to the time-delay interferometer (TDI) in the heralding setup. The outputs of the TDI are sent back into the dilution refrigerator and directly coupled to superconducting nanowire single photon detectors (SNSPDs, PhotonSpot), which are mounted at the 1K stage and are coated with dielectrics to optimize detection efficiency exactly at $737\,\mathrm{nm}$.

The total heralding efficiency η of the memory node is an important parameter since it directly affects the performance of the BSM for quantum communication experiments. One of the contributing factors is the detection quantum efficiency (QE) of the fiber-coupled SNSPDs. To estimate it we compare the performance of the SNSPDs to the specifications of calibrated conventional avalanche photodiodes single-photon counters (Laser Components COUNT-10C-FC). The estimated QEs of the SNSPDs with this method are as close to unity as we can verify. Additionally, we measure $< 1\%$ reflection from the fiber-SNSPD interface, which typically is the dominant contribution to the reduction of QE in these devices. Thus we assume the lower bound of the QE of the SNSPDs to be $\eta_{\mathrm{QE}} = 0.99$ for the rest of this section. Of course, this estimation is subject to additional systematic errors. However, the actual QE of these detectors would be a common factor (and thus drop out) in a comparison between any two physical quantum communication systems.

Here we use 2 different approaches to estimate η. We first measure the most dominant loss, which arises from the average reflectivity of the critically coupled nanophotonic cavity (Fig. 2b). While the $|\uparrow\rangle$ state is highly reflecting (94.4%), the $|\downarrow\rangle$ state reflects only 4.1% of incident photons, leading to an average device reflectivity of $\eta_{sp} = 0.493$.

In method (1), we compare the input power photodiode M1 with that of photodiode MC. This estimates a lower-bound on the tapered-fiber diamond waveguide coupling efficiency of $\eta_c = 0.930 \pm 0.017$. This error bar arises from uncertainty due to photodiode noise and does not include systematic photodiode calibration uncertainty. However, we note that if the tapered fiber is replaced by a silver-coated fiber-based retroreflector, this calibration technique extracts a coupling efficiency of $\eta_c^{cal} \approx 0.98$, which is consistent with the expected reflectivity from such a retroreflector. We independently

Step	Process	Duration	Proceed to
1	Lock time-delay interferometer	200 ms	2
2	Readout SiV	30 µs	If status LOW: 4, else: 3
3	Apply microwave π pulse	32 ns	2
4	Run main experiment script	$\sim$ 200 ms	1

Table A.1: High-level experimental sequence. This sequence is programmed into the HSDIO and uses feedback from the status trigger sent from the FPGA (see Fig. A.1a). Main experimental sequence is described in Data Table A.2. External software with a response time of $100\,\mathrm{ms}$ is also used to monitor the status trigger. If it is HI for $\gtrsim 2\,\mathrm{s}$, the software activates an automatic re-lock procedure which compensates for spectral diffusion and ionization of the SiV center (Methods). Additionally, we keep track of the timing when the TDI piezo voltage rails. This guarantees that the SiV is always resonant with the photonic qubits and that the TDI performs high-fidelity measurements in X basis.

calibrate the efficiency through the 99:1 fiber beamsplitter and the TDI to be $\eta_f = 0.934$. This gives us our first estimate on the overall heralding efficiency $\eta = \eta_{sp}\eta_c\eta_f\eta_{\mathrm{QE}} = 0.425 \pm 0.008$.

In method (2), during the experiment we compare the reflected counts from the highly-reflecting ($|\uparrow\rangle$) spin-state measured on the SNSPDs with the counts on an avalanche photodiode single photon counting module (M2 in Fig. A.1b) which has a calibrated efficiency of ≈ 0.7 relative to the SNSPDs. From this measurement, we estimate an overall efficiency of fiber-diamond coupling, as well as transmission through all relevant splices and beamsplitters of $\eta_c\eta_f = 0.864 \pm 0.010$. This error bar arises from shot noise on the single photon detectors. Overall, this gives us a consistent estimate of $\eta = \eta_{sp}\eta_c\eta_f\eta_{\mathrm{QE}} = 0.422 \pm 0.005$. Methods (1) and (2), which each have independent systematic uncertainties associated with imperfect photodetector calibrations, are consistent to within a small residual systematic uncertainty, which is noted in the text where appropriate.

A.4 Experimental details of quantum communication experiment.

An asynchronous BSM (Fig. 3a) relies on (1) precise timing of the arrival of optical pulses (corresponding to photonic qubits[159,160] from Alice and Bob) with microwave control pulses on the quantum memory and (2) interferometrically stable rotations on reflected time-bin qubits for successful heralding. In order to accomplish (1), all equipment used for generation of microwave and optical fields is synchronized by a single device (National Instriuments HSDIO, Fig. A.1a) with programming described in Data Table A.1-2.

In order to accomplish (2), we use a single, narrow linewidth ($< 50\,\mathrm{kHz}$) Ti:Sapphire laser (M Squared SolsTiS-2000-PSX-XF, Fig. A.1b) both for generating photonic qubits and locking the TDI used to herald their arrival. In the experiment, photonic qubits are reflected from the device, sent into the TDI, and detected on the SNSPDs. All detected photons are processed digitally on a field-programmable gate array (FPGA, Fig. A.1a), and the arrival times of these heralding signals are recorded on a time-tagger (TT, Fig. A.1a), and constitute one bit of information of the BSM (m_1 or m_2). At the end of the experiment, a $30\,\mu\mathrm{s}$ pulse from the readout path is reflected off the device, and photons are counted in order to determine the spin state (m_3) depending on the threshold shown in Fig. 2c.

To minimize thermal drift of the TDI, it is mounted to a thermally weighted aluminum breadboard, placed in a polyurethane foam-lined and sand filled briefcase, and secured with glue to ensure passive stability on the minute timescale. We halt the experiment and actively lock the interferometer to the sensitive Y-quadrature every $\sim 200\,\mathrm{ms}$ by changing the length of the roughly $28\,\mathrm{m}$ long ($142\,\mathrm{ns}$) delay line with a cylindrical piezo. In order to use the TDI for X-measurements of the reflected qubits,

Step	Process	Duration	Proceed to
1	Run sequence in Fig. 3a for a given N	$10-20$ µs	2
2	Readout SiV + report readout to TT	30 µs	If status LOW: 1, else: 3
3	Apply microwave π pulse	32 ns	4
4	Readout SiV	30 µs	If status LOW: 3, else: 1

Table A.2: Main experimental sequence for memory-enhanced quantum communication. This script is followed until step 1 is run a total of 4000 times, and then terminates and returns to step 1 of Data Table A.1. The longest step is the readout step, which is limited by the fact that we operate at a photon detection rate of ~ 1 MHz to avoid saturation of the SNSPDs.

we apply a frequency shift of 1.8 MHz using the qubit AOM, which is $1/4$ of the free-spectral range of the TDI. Since the nanophotonic cavity, the TDI, and the SNSPDs are all polarization sensitive, we use various fiber-based polarization controllers (Fig. A.1b). All fibers in the network are covered with aluminum foil to prevent thermal polarization drifts. This results in an interference visibility of the TDI of $> 99\%$ that is stable for several days without any intervention with lab temperature and humidity variations of $\pm 1^\circ$ C and $\pm 5\%$ respectively. In order to achieve high-fidelity operations we have to ensure that the laser frequency (which is not locked) is resonant with the SiV frequency f_0 (which is subject to the spectral diffusion [23]). To do that we implement a so-called preselection procedure, described in Data Table A.1-2 and Fig. A.1a. First, the SiV spin state is initialized by performing a projective measurement and applying microwave feedback. During each projective readout, the reflected counts are compared with two thresholds: a "readout" threshold of 7 photons (used only to record m_3), and a "status" threshold of 3 photons. The status trigger is used to prevent the experiment from running in cases when the laser is no longer on resonance with f_0, or if the SiV has ionized to an optically inactive charge state. The duty cycle of the status trigger is externally monitored and is used to temporarily abort the experiment and run an automated re-lock procedure that locates and

sets the laser to the new frequency f_0, reinitailizing the SiV charge state with a 520 nm laser pulse if nececssary. This protocol enables fully automated operation at high fidelities (low QBER) for several days without human intervention.

A.5 Optimal parameters for asynchronous Bell state measurements.

We minimize the experimentally extracted QBER for the asynchronous BSM to optimize the performance of the memory node. The first major factor contributing to QBER is the scattering of a third photon that is not detected, due to the finite heralding efficiency $\eta = 0.423 \pm 0.04$. This is shown in Fig. 2f, where the fidelity of the spin-photon entangled state diminishes for $\langle n|n\rangle_m \gtrsim 0.02$. At the same time, we would like to work at the maximum possible $\langle n|n\rangle_m$ in order to maximize the data rate to get enough statistics to extract QBER (and in the quantum communication setting, efficiently generate a key).

To increase the key generation rate per channel use, one can also fit many photonic qubits within each initialization of the memory. In practice, there are 2 physical constraints: (1) the bandwidth of the SiV-photon interface and (2) the coherence time of the memory. We find that one can satisfy (1) at a bandwidth of roughly 50 MHz with no measurable infidelity. For shorter optical pulses (< 10 ns), the spin-photon gate fidelity is reduced. In principle, the SiV-photon bandwidth can be increased by reducing the atom-cavity detuning (here ~ 60 GHz) at the expense of having to operate at higher magnetic fields where microwave qubit manipulation is not as convenient[23].

Even with just an XY8-1 decoupling sequence (number of π pulses $N_\pi = 8$), the coherence time

of the SiV is longer than 200 μs (Fig. A.3c) and can be prolonged to the millisecond range with longer pulse sequences[22]. Unfortunately, to satisfy the bandwidth criteria (1) and to drive both hyperfine transitions (Fig. A.3a), we must use short (32 ns) long π pulses, which cause additional decoherence from ohmic heating[23] already at $N_\pi = 64$ (Fig. A.3e). Due to this we limit the pulse sequences to a maximum $N_\pi = 128$, and only use up to $\approx 20\,\mu$s of the memory time. One solution would be to switch to superconducting microwave delivery. Alternatively, one can use a larger value of τ to allow the device to cool down in between subsequent pulses[23] at the expense of having to stabilize a TDI of larger δt. Working at larger δt also enables temporal multiplexing by fitting multiple time-bin qubits per free-precession interval. In fact, with $2\tau = 142$ ns, even given constraint (1) and the finite π time, we can already fit up to 4 optical pulses per free-precession window, enabling a total number of photonic qubits of up to $N = 504$ for only $N_\pi = 128$.

In benchmarking the asynchronous BSM for quantum communication, we optimize the parameters $\langle n|n\rangle_m$ and N to maximize our enhancement over the direct transmission approach, which is a combination of both increasing N and reducing the QBER, since a large QBER results in a small distilled key fraction r_s. As described in the main text, the effective loss can be associated with $\langle n|n\rangle_p$, which is the average number of photons per photonic qubit arriving at the device, and is given straightforwardly by $\langle n|n\rangle_p = \langle n|n\rangle_m / N$. The most straightforward way to sweep the loss is to keep the experimental sequence the same (fixed N) and vary the overall power, which changes $\langle n|n\rangle_m$. The results of such a sweep are shown in Fig. A.5a, b. For larger $\langle n|n\rangle_m$ (corresponding to lower effective channel losses), the errors associated with scattering an additional photon reduce the performance of the memory device.

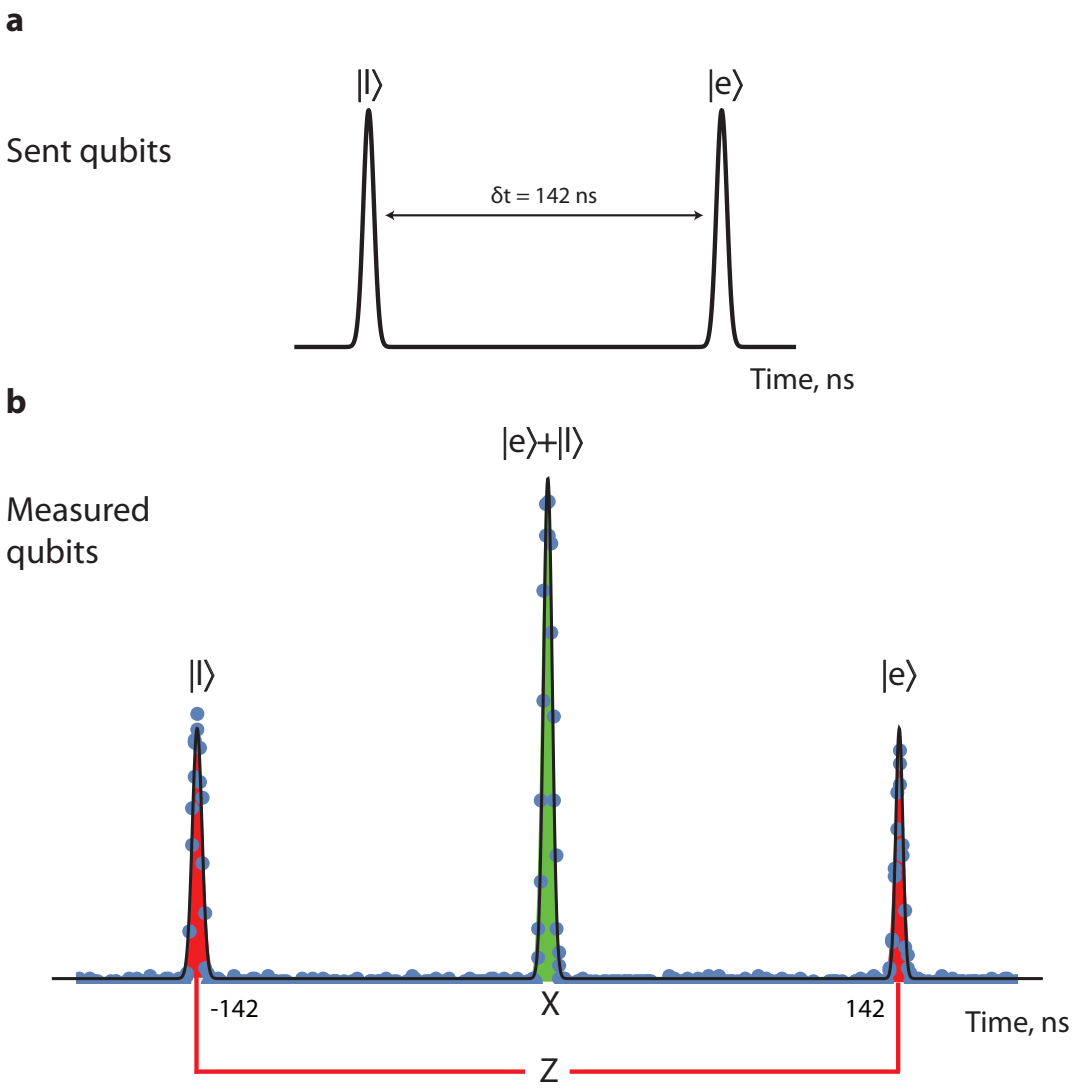


Figure A.4: Measurements on a single time-bin qubit in Z and X bases. a, Example of optical pulses sent for example in the experiment described in Fig. 2d. b, Time trace of detected photons on + detector when pulses shown in (a) are sent directly into the TDI. The first and last peaks correspond to late and early photons taking the long and short paths of the TDI, which enable measurements in the Z basis $\{|e\rangle, |l\rangle\}$. The central bin corresponds to the late and early components overlapping and interfering constructively to come out of the + port, equivalent to a measurement of the time bin qubit in the $|+x\rangle$ state. A detection event in this same timing window on the - detector (not shown) would constitute a $|-x\rangle$ measurement. In this measurement, the TDI was left unlocked, so we observe no interference in the central window.

Due to these considerations, we work at roughly $\langle n|n\rangle_m \lesssim 0.02$ for experiments in the main text shown in Fig. 3 and 4, below which the performance does not improve significantly. At this value, we obtain BSM successes at a rate of roughly 0.1 Hz. By fixing $\langle n|n\rangle_m$ and increasing N, we maintain a tolerable BSM success rate while increasing the effective channel loss. Eventually, as demonstrated in Fig. A.5c and in the high-loss data point in Fig. 4, effects associated with microwave heating result in errors that again diminish the performance of the memory node for large N. As such, we conclude that the optimal performance of our node occurs for $\langle n|n\rangle_m \sim 0.02$ and $N \approx 124$, corresponding to an effective channel loss of 69 dB between Alice and Bob, which is equivalent to roughly 350 km of telecommunications fiber.

We also find that the QBER and thus the performance of the communication link is limited by imperfect preparation of photonic qubits. Photonic qubits are defined by sending arbitrary phase patterns generated by the optical AWG to a phase modulator. For an example of such a pattern, see the blue curve in Fig. 3a. We use an imperfect pulse amplifier with finite bandwidth ($0.025 - 700$ MHz), and find that the DC component of these waveforms can result in error in photonic qubit preparation on the few $\%$ level. By using a tailored waveform of phases with smaller (or vanishing) DC component, we can reduce these errors. We run such an experiment during the test of the Bell-CHSH inequality. We find that by evaluating BSM correlations from $|\pm a\rangle$ and $|\pm b\rangle$ inputs during this measurement, we estimate a QBER of 0.097 ± 0.006.

Finally, we obtain the effective clock-rate of the communication link by measuring the total number of photonic qubits sent over the course of an entire experiment. In practice, we record the number of channel uses, determined by the number of sync triggers recorded (see Fig. A.1a) as well as the number

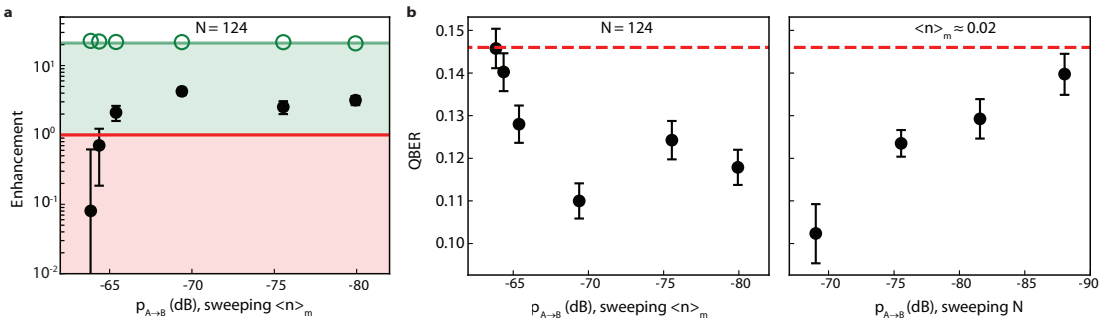


Figure A.5: Performance of memory-device versus of channel loss. a, Enhancement of memory-based approach compared to direct transmission approach, keeping $N = 124$ fixed and varying $\langle n|n\rangle_m$ in order to vary the effective channel transmission probability $p_{A\to B}$. At high $p_{A\to B}$ (larger $\langle n|n\rangle_m$), r_s approaches 0 due to increased QBER arising from undetected scattering of a third photon. b, (Left) Plot of QBER for same sweep of $\langle n|n\rangle_m$ shown in a. (Right) Plot of QBER while sweeping N in order to vary loss. These points correspond to the same data shown in Fig. 4. At lower $p_{A\to B}$ (larger N), microwave-induced heating-related dephasing leads to increased QBER. Vertical error bars are given by the 68% confidence interval and horizontal error bars represent the standard deviation of the systematic power fluctuations.

of qubits per sync trigger (N). We then divide this number by the total experimental time from start to finish ($\sim$ 1-2 days for most experimental runs), including all experimental downtime used to stabilize the interferometer, readout and initialize the SiV, and compensate for spectral diffusion and ionization. For $N = 248$, we extract a clock rate of 1.2 MHz. As the distilled key rate in this configuration exceeds the conventional limit of $p/2$ by a factor of 3.8 ± 1.1, it is competitive with a standard linear-optics based system operating at $4.5^{+1.3}_{-1.2}$ MHz clock rate.

A.6 Performance of memory-assisted quantum communication.

A single optical link can provide many channels, for example, by making use of different frequency, polarization, or temporal modes. To account for this, when comparing different systems, data rates can be defined on a per-channel-use basis. In a quantum communication setting, full usage of the

communication channel between Alice and Bob means that both links from Alice and Bob to Charlie are in use simultaneously. For an asynchronous sequential measurement, typically only half of the channel is used at a time, for example from Alice to Charlie or Bob to Charlie. The other half can in principle be used for a different task when not in use. For example, the unused part of the channel could be routed to a secondary asynchronous BSM device. In our experiment, we can additionally define as a second normalization the rate per channel "occupancy", which accounts for the fact that only half the channel is used at any given time. The rate per channel occupancy is therefore half the rate per full channel use. For comparison, we typically operate at 1.2% channel use and 2.4% channel occupancy.

To characterize the optimal performance of the asynchronous Bell state measurement device, we operate it in the optimal regime determined above ($N = 124$, $\langle n|n\rangle_m \lesssim 0.02$). We note that the enhancement in the sifted key rate over direct transmission is given by

$$\frac{R}{R_{\text{max}}} = \eta^2 \frac{(N_\pi - 1)(N_\pi - 2)N_{\text{sub}}}{2N_\pi} \tag{A.2}$$

and is independent of $\langle n|n\rangle_m$ for a fixed number of microwave pulses N_π and optical pulses per microwave pulse N_{sub} and thus fixed $N = N_\pi N_{\text{sub}}$. For low $\langle n|n\rangle_m$, three photon events become negligible and therefore QBER saturates, such that the enhancement in the distilled key rate saturates as well (Fig. A.5a). We can therefore combine all data sets with fixed $N = 124$ below $\langle n|n\rangle_m \lesssim 0.02$ to characterize the average QBER of 0.116 ± 0.002 (Fig. 3c). The key rates cited in the main text relate to a data set in this series ($\langle n|n\rangle_m \approx 0.02$), with a QBER of 0.110 ± 0.004. A summary of

Alice	Bob	Parity	Bell state
$\|+x\rangle$	$\|+x\rangle$	$+1$	$\|\Phi_+\rangle$
$\|+x\rangle$	$\|-x\rangle$	-1	$\|\Phi_-\rangle$
$\|-x\rangle$	$\|+x\rangle$	-1	$\|\Phi_-\rangle$
$\|-x\rangle$	$\|-x\rangle$	$+1$	$\|\Phi_+\rangle$
$\|+y\rangle$	$\|+y\rangle$	-1	$\|\Phi_-\rangle$
$\|+y\rangle$	$\|-y\rangle$	$+1$	$\|\Phi_+\rangle$
$\|-y\rangle$	$\|+y\rangle$	$+1$	$\|\Phi_+\rangle$
$\|-y\rangle$	$\|-y\rangle$	-1	$\|\Phi_-\rangle$

Table A.3: Truth table of asynchronous BSM protocol, showing the parity (and BSM outcome) for each set of valid input states from Alice and Bob. In the case of Y basis inputs, Alice and Bob adjust the sign of their input state depending on whether it was commensurate with an even or odd numbered free-precession interval, based on timing information provided by Charlie (Supplementary Information).

	per channel occupancy	per channel occupancy	per channel use	per channel use
X:Y basis bias	50 : 50	99 : 1	50 : 50	99 : 1
Distilled key rate R $[10^{-7}]$	$1.19^{+0.14}_{-0.14}$	$2.33^{+0.28}_{-0.28}$	$2.37^{+0.29}_{-0.28}$	$4.66^{+0.56}_{-0.55}$
$R/R_{\max}$(X:Y)	$2.06^{+0.25}_{-0.25}$	$2.06^{+0.25}_{-0.25}$	$4.13^{+0.50}_{-0.49}$	$4.13^{+0.50}_{-0.49}$
$R/(1.44p_{A\to B})$	$0.71^{+0.09}_{-0.08}$	$1.40^{+0.17}_{-0.17}$	$1.43^{+0.17}_{-0.17}$	$2.80^{+0.34}_{-0.33}$
$1-$confidence level		$1.1^{+0.4}_{-0.3}\times10^{-2}$	$8^{+3}_{-2}\times10^{-3}$	$1.3^{+0.5}_{-0.3}\times10^{-7}$

Table A.4: Quantum-memory-based advantage. Distilled key rates with the asynchronous BSM device and comparison to ideal direct communication implementations, based on the performance of our network node for $N = 124$ and $\langle n|n\rangle_m \sim 0.02$. Distillable key rates for $E = 0.110 \pm 0.004$ for unbiased and biased basis choice are expressed in a per-channel-occupancy and per-channel-use normalization (Methods). Enhancement is calculated versus the linear optics BSM limit ($R_{\max}(50:50) = p_{A\to B}/2$ for unbiased bases, $R_{\max}(99:1) = 0.98p_{A\to B}$ with biased bases) and versus the fundamental repeaterless channel capacity [148] ($1.44p_{A\to B}$). Confidence levels for surpassing the latter bound [148] are given in the final row.

key rates calculated on a per-channel use and per-channel occupancy basis, as well as comparisons of performance to an ideal linear-optics BSM and the repeaterless bound[148] are given in Data Table A.4. Furthermore, we extrapolate the performance of our memory node to include biased input bases from Alice and Bob. This technique enables a reduction of channel uses where Alice and Bob send photons in different bases, but is still compatible with secure key distribution[153], allowing for enhanced distilled key rates by at most a factor of 2. The extrapolated performance of our node for a bias of 99:1 is also displayed in Data Table A.4, as well as comparisons to the relevant bounds. We note that basis biasing does not affect the performance when comparing to the equivalent direct-transmission experiment, which is limited by $p_{A\to B}/2$ in the unbiased case and $p_{A\to B}$ in the biased case. However, using biased

input bases does make the performance of the memory-assisted approach more competitive with the fixed repeaterless bound[148] of $1.44p_{A\to B}$.

References

[1] S. Kolkowitz, Q. P. Unterreithmeier, S. D. Bennett, and M. D. Lukin, "Sensing distant nuclear spins with a single electron spin," *Phys. Rev. Lett.*, vol. 109, p. 137601, Sep 2012.

[2] F. Arute, K. Arya, R. Babbush, D. Bacon, J. C. Bardin, R. Barends, R. Biswas, S. Boixo, F. G. S. L. Brandao, D. A. Buell, and et al., "Quantum supremacy using a programmable superconducting processor," *Nature*, vol. 574, p. 505–510, Oct 2019.

[3] C. Degen, F. Reinhard, and P. Cappellaro, "Quantum sensing," *Reviews of Modern Physics*, vol. 89, Jul 2017.

[4] S. McArdle, S. Endo, A. Aspuru-Guzik, S. C. Benjamin, and X. Yuan, "Quantum computational chemistry," *Reviews of Modern Physics*, vol. 92, Mar 2020.

[5] H. J. Kimble, "The quantum internet," *Nature*, vol. 453, pp. 1023 EP –, Jun 2008.

[6] V. Scarani, H. Bechmann-Pasquinucci, N. J. Cerf, M. Dušek, N. Lütkenhaus, and M. Peev, "The security of practical quantum key distribution," *Reviews of Modern Physics*, vol. 81, no. 3, pp. 1301–1350, 2009.

[7] S. Wehner, D. Elkouss, and R. Hanson, "Quantum internet: A vision for the road ahead," *Science*, vol. 362, no. 6412, 2018.

[8] S. E. Economou, N. Lindner, and T. Rudolph, "Optically Generated 2-Dimensional Photonic Cluster State from Coupled Quantum Dots," *Physical Review Letters*, vol. 105, p. 93601, aug 2010.

[9] I. H. Deutsch, "Harnessing the power of the second quantum revolution," *PRX Quantum*, vol. 1, p. 020101, Nov 2020.

[10] H.-J. Briegel, W. Dür, J. I. Cirac, and P. Zoller, "Quantum repeaters: The role of imperfect local operations in quantum communication," *Phys. Rev. Lett.*, vol. 81, pp. 5932–5935, Dec 1998.

[11] A. Reiserer and G. Rempe, "Cavity-based quantum networks with single atoms and optical photons," *Reviews of Modern Physics*, vol. 87, pp. 1379–1418, dec 2015.

[12] P. W. Shor and J. Preskill, "Simple proof of security of the BB84 quantum key distribution protocol," *Physical Review Letters*, vol. 85, no. 2, pp. 441–444, 2000.

[13] M. Ruf, M. Weaver, S. van Dam, and R. Hanson, "Resonant excitation and purcell enhancement of coherent nitrogen-vacancy centers coupled to a fabry-perot microcavity," *Phys. Rev. Applied*, vol. 15, p. 024049, Feb 2021.

[14] D. Simin, H. Kraus, A. Sperlich, T. Ohshima, G. V. Astakhov, and V. Dyakonov, "Locking of electron spin coherence above 20 ms in natural silicon carbide," *Phys. Rev. B*, vol. 95, p. 161201, Apr 2017.

[15] T. Zhong, J. M. Kindem, J. G. Bartholomew, J. Rochman, I. Craiciu, V. Verma, S. W. Nam, F. Marsili, M. D. Shaw, A. D. Beyer, and A. Faraon, "Optically addressing single rare-earth ions in a nanophotonic cavity," *Phys. Rev. Lett.*, vol. 121, p. 183603, Oct 2018.

[16] P. Lodahl, S. Mahmoodian, and S. Stobbe, "Interfacing single photons and single quantum dots with photonic nanostructures," *Rev. Mod. Phys.*, vol. 87, no. 2, p. 347, 2015.

[17] S. Welte, B. Hacker, S. Daiss, S. Ritter, and G. Rempe, "Photon-mediated quantum gate between two neutral atoms in an optical cavity," *Phys. Rev. X*, vol. 8, no. 1, p. 011018, 2018.

[18] Z.-S. Yuan, Y.-A. Chen, B. Zhao, S. Chen, J. Schmiedmayer, and J.-W. Pan, "Experimental demonstration of a BDCZ quantum repeater node," *Nature*, vol. 454, p. 1098, aug 2008.

[19] A. Sipahigil, R. E. Evans, D. D. Sukachev, M. J. Burek, J. Borregaard, M. K. Bhaskar, C. T. Nguyen, J. L. Pacheco, H. A. Atikian, C. Meuwly, R. M. Camacho, F. Jelezko, E. Bielejec, H. Park, M. Lončar, and M. D. Lukin, "An integrated diamond nanophotonics platform for quantum-optical networks," *Science*, vol. 354, no. 6314, pp. 847–850, 2016.

[20] M. K. Bhaskar, R. Riedinger, B. Machielse, D. S. Levonian, C. T. Nguyen, E. N. Knall, H. Park, D. Englund, M. Lončar, D. D. Sukachev, and et al., "Experimental demonstration of memory-enhanced quantum communication," *Nature*, vol. 580, p. 60–64, Mar 2020.

[21] M. J. Burek, Y. Chu, M. S. Z. Liddy, P. Patel, J. Rochman, S. Meesala, W. Hong, Q. Quan, M. D. Lukin, and M. Loncar, "High quality-factor optical nanocavities in bulk single-crystal diamond," *Nature Communications*, vol. 5, pp. 5718 EP –, Dec 2014. Article.

[22] C. T. Nguyen, D. D. Sukachev, M. K. Bhaskar, B. Machielse, D. S. Levonian, E. N. Knall, P. Stroganov, R. Riedinger, H. Park, M. Loncar, and M. D. Lukin, "Quantum Network

Nodes Based on Diamond Qubits with an Efficient Nanophotonic Interface," *Phys. Rev. Lett.*, vol. 123, p. 183602, oct 2019.

[23] C. T. Nguyen, D. D. Sukachev, M. K. Bhaskar, B. Machielse, D. S. Levonian, E. N. Knall, P. Stroganov, C. Chia, M. J. Burek, R. Riedinger, H. Park, M. Loncar, and M. D. Lukin, "An integrated nanophotonic quantum register based on silicon-vacancy spins in diamond," *Phys. Rev. B*, vol. 100, p. 165428, oct 2019.

[24] B. Machielse, S. Bogdanovic, S. Meesala, S. Gauthier, M. J. Burek, G. Joe, M. Chalupnik, Y. I. Sohn, J. Holzgrafe, R. E. Evans, C. Chia, H. Atikian, M. K. Bhaskar, D. D. Sukachev, L. Shao, S. Maity, M. D. Lukin, and M. Lončar, "Quantum Interference of Electromechanically Stabilized Emitters in Nanophotonic Devices," *Physical Review X*, vol. 9, p. 31022, aug 2019.

[25] A. Zaitsev, *Optical Properties of Diamond*. Berlin: Springer-Verlag Berlin Heidelberg, 2001.

[26] C. Hepp, T. Müller, V. Waselowski, J. N. Becker, B. Pingault, H. Sternschulte, D. Steinmüller-Nethl, A. Gali, J. R. Maze, M. Atatüre, and C. Becher, "Electronic structure of the silicon vacancy color center in diamond," *Phys. Rev. Lett.*, vol. 112, p. 036405, Jan 2014.

[27] T. Teraji, T. Yamamoto, K. Watanabe, Y. Koide, J. Isoya, S. Onoda, T. Ohshima, L. J. Rogers, F. Jelezko, P. Neumann, J. Wrachtrup, and S. Koizumi, "Homoepitaxial diamond film growth: High purity, high crystalline quality, isotopic enrichment, and single color center formation," *physica status solidi (a)*, vol. 212, no. 11, pp. 2365–2384, 2015.

[28] W. Fei, K. Wei, A. Morishita, H. Wang, and H. Kawarada, "Local initial heteroepitaxial growth of diamond (111) on ru (0001)/c-sapphire by antenna-edge-type microwave plasma chemical vapor deposition," *Applied Physics Letters*, vol. 117, no. 11, p. 112102, 2020.

[29] B. Khanaliloo, M. Mitchell, A. C. Hryciw, and P. E. Barclay, "High-q/v monolithic diamond microdisks fabricated with quasi-isotropic etching," *Nano Letters*, vol. 15, no. 8, pp. 5131–5136, 2015. PMID: 26134379.

[30] T. Yamamoto, T. Umeda, K. Watanabe, S. Onoda, M. Markham, D. Twitchen, B. Naydenov, L. McGuinness, T. Teraji, S. Koizumi, *et al.*, "Extending spin coherence times of diamond qubits by high-temperature annealing," *Phys. Rev. B*, vol. 88, no. 7, p. 075206, 2013.

[31] D. Bluvstein, Z. Zhang, and A. C. B. Jayich, "Identifying and mitigating charge instabilities in shallow diamond nitrogen-vacancy centers," *Phys. Rev. Lett.*, vol. 122, p. 076101, Feb 2019.

[32] J. R. Maze, A. Gali, E. Togan, Y. Chu, A. Trifonov, E. Kaxiras, and M. D. Lukin, "Properties of nitrogen-vacancy centers in diamond: the group theoretic approach," *New J. Phys.*, vol. 13, no. 2, p. 025025, 2011.

[33] M. H. Abobeih, J. Cramer, M. A. Bakker, N. Kalb, M. Markham, D. J. Twitchen, and T. H. Taminiau, "One-second coherence for a single electron spin coupled to a multi-qubit nuclear-spin environment," *Nature Communications*, vol. 9, no. 1, p. 2552, 2018.

[34] C. E. Bradley, J. Randall, M. H. Abobeih, R. C. Berrevoets, M. J. Degen, M. A. Bakker, M. Markham, D. J. Twitchen, and T. H. Taminiau, "A 10-qubit solid-state spin register with quantum memory up to one minute," *arXiv preprint arXiv:1905.02094*, 2019.

[35] B. Hensen, H. Bernien, A. E. Dréau, A. Reiserer, N. Kalb, M. S. Blok, J. Ruitenberg, R. F. L. Vermeulen, R. N. Schouten, C. Abellán, W. Amaya, V. Pruneri, M. W. Mitchell, M. Markham, D. J. Twitchen, D. Elkouss, S. Wehner, T. H. Taminiau, and R. Hanson, "Loophole-free Bell inequality violation using electron spins separated by 1.3 kilometres," *Nature*, vol. 526, p. 682, oct 2015.

[36] P. C. Humphreys, N. Kalb, J. P. Morits, R. N. Schouten, R. F. Vermeulen, D. J. Twitchen, M. Markham, and R. Hanson, "Deterministic delivery of remote entanglement on a quantum network," *Nature*, vol. 558, no. 7709, p. 268, 2018.

[37] N. Kalb, A. A. Reiserer, P. C. Humphreys, J. J. W. Bakermans, S. J. Kamerling, N. H. Nickerson, S. C. Benjamin, D. J. Twitchen, M. Markham, and R. Hanson, "Entanglement distillation between solid-state quantum network nodes," *Science*, vol. 356, pp. 928 LP – 932, jun 2017.

[38] P. Tamarat, T. Gaebel, J. Rabeau, M. Khan, A. Greentree, H. Wilson, L. Hollenberg, S. Prawer, P. Hemmer, F. Jelezko, *et al.*, "Stark shift control of single optical centers in diamond," *Phys. Rev. Lett.*, vol. 97, no. 8, p. 083002, 2006.

[39] Y.-I. Sohn, S. Meesala, B. Pingault, H. A. Atikian, J. Holzgrafe, M. Gündogan, C. Stavrakas, M. J. Stanley, A. Sipahigil, J. Choi, M. Zhang, J. L. Pacheco, J. Abraham, E. Bielejec, M. D. Lukin, M. Atatüre, and M. Loncar, "Controlling the coherence of a diamond spin qubit through its strain environment," *Nature Communications*, vol. 9, no. 1, p. 2012, 2018.

[40] M. J. Burek, C. Meuwly, R. E. Evans, M. K. Bhaskar, A. Sipahigil, S. Meesala, B. Machielse, D. D. Sukachev, C. T. Nguyen, J. L. Pacheco, E. Bielejec, M. D. Lukin, and M. Lončar, "Fiber-

coupled diamond quantum nanophotonic interface," *Phys. Rev. Applied*, vol. 8, p. 024026, Aug 2017.

[41] D. D. Sukachev, A. Sipahigil, C. T. Nguyen, M. K. Bhaskar, R. E. Evans, F. Jelezko, and M. D. Lukin, "Silicon-vacancy spin qubit in diamond: A quantum memory exceeding 10 ms with single-shot state readout," *Phys. Rev. Lett.*, vol. 119, p. 223602, Nov 2017.

[42] M. K. Bhaskar, D. D. Sukachev, A. Sipahigil, R. E. Evans, M. J. Burek, C. T. Nguyen, L. J. Rogers, P. Siyushev, M. H. Metsch, H. Park, F. Jelezko, M. Lončar, and M. D. Lukin, "Quantum nonlinear optics with a germanium-vacancy color center in a nanoscale diamond waveguide," *Phys. Rev. Lett.*, vol. 118, p. 223603, May 2017.

[43] T. Iwasaki, Y. Miyamoto, T. Taniguchi, P. Siyushev, M. H. Metsch, F. Jelezko, and M. Hatano, "Tin-vacancy quantum emitters in diamond," *Phys. Rev. Lett.*, vol. 119, p. 253601, Dec 2017.

[44] A. E. Rugar, H. Lu, C. Dory, S. Sun, P. J. McQuade, Z.-X. Shen, N. A. Melosh, and J. Vučković, "Generation of tin-vacancy centers in diamond via shallow ion implantation and subsequent diamond overgrowth," *Nano Letters*, vol. 20, no. 3, pp. 1614–1619, 2020. PMID: 32031821.

[45] B. L. Green, S. Mottishaw, B. G. Breeze, A. M. Edmonds, U. F. S. D'Haenens-Johansson, M. W. Doherty, S. D. Williams, D. J. Twitchen, and M. E. Newton, "Neutral silicon-vacancy center in diamond: Spin polarization and lifetimes," *Phys. Rev. Lett.*, vol. 119, p. 096402, Aug 2017.

[46] M. O. Scully and M. S. Zubairy, *Quantum Optics*. Cambridge University Press, 1997.

[47] J. D. Joannopoulos, S. G. Johnson, J. N. Winn, and R. D. Meade, *Photonic Crystals: Molding the Flow of Light (Second Edition)*. Princeton University Press, 2 ed., 2008.

[48] N. Kalb, A. Reiserer, S. Ritter, and G. Rempe, "Heralded Storage of a Photonic Quantum Bit in a Single Atom," *Physical Review Letters*, vol. 114, p. 220501, jun 2015.

[49] J. Zhou, J. Zheng, Z. Fang, P. Xu, and A. Majumdar, "Ultra-low mode volume on-substrate silicon nanobeam cavity," *Opt. Express*, vol. 27, pp. 30692–30699, Oct 2019.

[50] Q. Quan and M. Loncar, "Deterministic design of wavelength scale, ultra-high q photonic crystal nanobeam cavities," *Opt. Express*, vol. 19, pp. 18529–18542, Sep 2011.

[51] P. N. Prasad, *Nanophotonics*. Hoboken: John Wiley and Sons, Inc, 2004.

[52] T. M. Babinec, J. T. Choy, K. J. M. Smith, M. Khan, and M. Lončar, "Design and focused ion beam fabrication of single crystal diamond nanobeam cavities," *Journal of Vacuum Science & Technology B*, vol. 29, no. 1, p. 010601, 2011.

[53] B. J. M. Hausmann, B. Shields, Q. Quan, P. Maletinsky, M. McCutcheon, J. T. Choy, T. M. Babinec, A. Kubanek, A. Yacoby, M. D. Lukin, and M. Lončar, "Integrated diamond networks for quantum nanophotonics," *Nano Letters*, vol. 12, no. 3, pp. 1578–1582, 2012. PMID: 22339606.

[54] H. Bernien, B. Hensen, W. Pfaff, G. Koolstra, M. S. Blok, L. Robledo, T. H. Taminiau, M. Markham, D. J. Twitchen, L. Childress, and R. Hanson, "Heralded entanglement between solid-state qubits separated by three metres," *Nature*, vol. 497, pp. 86–90, May 2013.

[55] T. Babinec, a. K. M. Hausmann, B., and et al., "A diamond nanowire single-photon source," *Nature Nanotech*, vol. 5, pp. 195–199, 2010.

[56] P. Maletinsky, S. Hong, and a. e. a. Grinolds, M, "A robust scanning diamond sensor for nanoscale imaging with single nitrogen-vacancy centres," *Nature Nanotech*, vol. 7, pp. 320–324, 2012.

[57] J. T. Choy, B. J. M. Hausmann, T. M. Babinec, I. Bulu, M. Khan, P. Maletinsky, A. Yacoby, and M. Lončar, "Enhanced single-photon emission from a diamond–silver aperture," *Nature Photonics*, vol. 5, p. 738–743, Oct 2011.

[58] L. Marseglia, J. P. Hadden, A. C. Stanley-Clarke, J. P. Harrison, B. Patton, Y.-L. D. Ho, B. Naydenov, F. Jelezko, J. Meijer, P. R. Dolan, J. M. Smith, J. G. Rarity, and J. L. O'Brien, "Nanofabricated solid immersion lenses registered to single emitters in diamond," *Applied Physics Letters*, vol. 98, no. 13, p. 133107, 2011.

[59] W. B. Gao, A. Imamoglu, H. Bernien, and R. Hanson, "Coherent manipulation, measurement and entanglement of individual solid-state spins using optical fields," *Nature Photonics*, vol. 9, pp. 363 EP –, May 2015. Review Article.

[60] T. Huang, R. Grote, S. Mann, and et al, "A monolithic immersion metalens for imaging solid-state quantum emitters," *Nat Commun.*, vol. 10, Feb 2019.

[61] C. e. a. Dory, "Inverse-designed diamond photonics," *Nat. Commun*, 2019.

[62] N. H. e. a. Wan, "Large-scale integration of near-indistinguishable artificial atoms in hybrid photonic circuits," *Nature*, 2020.

[63] J. C. Lee, I. Aharonovich, A. P. Magyar, F. Rol, and E. L. Hu, "Coupling of silicon-vacancy centers to a single crystal diamond cavity," *Opt. Express*, vol. 20, pp. 8891–8897, Apr 2012.

[64] N. H. Wan, S. Mouradian, and D. Englund, "Two-dimensional photonic crystal slab nanocavities on bulk single-crystal diamond," *Applied Physics Letters*, vol. 112, no. 14, p. 141102, 2018.

[65] H. A. Atikian, P. Latawiec, M. J. Burek, Y.-I. Sohn, S. Meesala, N. Gravel, A. B. Kouki, and M. Lončar, "Freestanding nanostructures via reactive ion beam angled etching," *APL Photonics*, vol. 2, no. 5, p. 051301, 2017.

[66] W.-J. Jeong, E. Shong, H. Hahm, K.-I. Min, H. Choi, and Y. K. Kim, "Mathematical modeling and measurement of etching profile for junction shape control in mr read heads," *Magnetics, IEEE Transactions on*, vol. 35, pp. 2601 – 2603, 10 1999.

[67] T. Lund-Hansen, S. Stobbe, B. Julsgaard, H. Thyrrestrup, T. Sünner, M. Kamp, A. Forchel, and P. Lodahl, "Experimental realization of highly efficient broadband coupling of single quantum dots to a photonic crystal waveguide," *Phys. Rev. Lett.*, vol. 101, p. 113903, Sep 2008.

[68] R. E. Evans, A. Sipahigil, D. D. Sukachev, A. S. Zibrov, and M. D. Lukin, "Narrow-linewidth homogeneous optical emitters in diamond nanostructures via silicon ion implantation," *Phys. Rev. Applied*, vol. 5, p. 044010, Apr 2016.

[69] J. F. Ziegler, M. Ziegler, and J. Biersack, "Srim – the stopping and range of ions in matter (2010)," *Nuclear Instruments and Methods in Physics Research Section B: Beam Interactions with Materials and Atoms*, vol. 268, no. 11, pp. 1818 – 1823, 2010. 19th International Conference on Ion Beam Analysis.

[70] R. E. Evans, M. K. Bhaskar, D. D. Sukachev, C. T. Nguyen, A. Sipahigil, M. J. Burek, B. Machielse, G. H. Zhang, A. S. Zibrov, E. Bielejec, H. Park, M. Lončar, and M. D. Lukin, "Photon-mediated interactions between quantum emitters in a diamond nanocavity," *Science*, vol. 362, no. 6415, pp. 662–665, 2018.

[71] P. Udvarhelyi, R. Nagy, F. Kaiser, S.-Y. Lee, J. Wrachtrup, and A. Gali, "Spectrally stable defect qubits with no inversion symmetry for robust spin-to-photon interface," *Phys. Rev. Applied*, vol. 11, p. 044022, Apr 2019.

[72] P. Lodahl, "Scaling up solid-state quantum photonics," *Science*, vol. 362, no. 6415, pp. 646–646, 2018.

[73] S. Sun, J. L. Zhang, K. A. Fischer, M. J. Burek, C. Dory, K. G. Lagoudakis, Y.-K. Tzeng, M. Radulaski, Y. Kelaita, A. Safavi-Naeini, Z.-X. Shen, N. A. Melosh, S. Chu, M. Lončar, and J. Vučković, "Cavity-enhanced raman emission from a single color center in a solid," *Phys. Rev. Lett.*, vol. 121, p. 083601, Aug 2018.

[74] S. Sun, H. Kim, G. S. Solomon, and E. Waks, "Strain tuning of a quantum dot strongly coupled to a photonic crystal cavity," *Applied Physics Letters*, vol. 103, no. 15, p. 151102, 2013.

[75] M. Zopf, T. Macha, R. Keil, E. Uruñuela, Y. Chen, W. Alt, L. Ratschbacher, F. Ding, D. Meschede, and O. G. Schmidt, "Frequency feedback for two-photon interference from separate quantum dots," *Phys. Rev. B*, vol. 98, p. 161302, Oct 2018.

[76] S. Meesala, Y.-I. Sohn, B. Pingault, L. Shao, H. A. Atikian, J. Holzgrafe, M. Gündoğan, C. Stavrakas, A. Sipahigil, C. Chia, R. Evans, M. J. Burek, M. Zhang, L. Wu, J. L. Pacheco, J. Abraham, E. Bielejec, M. D. Lukin, M. Atatüre, and M. Lončar, "Strain engineering of the silicon-vacancy center in diamond," *Phys. Rev. B*, vol. 97, p. 205444, May 2018.

[77] D. M. Toyli, C. D. Weis, G. D. Fuchs, T. Schenkel, and D. D. Awschalom, "Chip-scale nanofabrication of single spins and spin arrays in diamond," *Nano Letters*, vol. 10, pp. 3168–3172, Aug 2010.

[78] P. Ovartchaiyapong, K. W. Lee, B. A. Myers, and A. C. B. Jayich, "Dynamic strain-mediated coupling of a single diamond spin to a mechanical resonator," *Nature Communications*, vol. 5, pp. 4429 EP –, Jul 2014. Article.

[79] M. Gross and S. Haroche, "Superradiance: An essay on the theory of collective spontaneous emission," *Physics Reports*, vol. 93, no. 5, pp. 301 – 396, 1982.

[80] J. Johansson, P. Nation, and F. Nori, "Qutip 2: A python framework for the dynamics of open quantum systems," *Computer Physics Communications*, vol. 184, no. 4, pp. 1234 – 1240, 2013.

[81] S. Maity, L. Shao, Y.-I. Sohn, S. Meesala, B. Machielse, E. Bielejec, M. Markham, and M. Lončar, "Spectral alignment of single-photon emitters in diamond using strain gradient," *Phys. Rev. Applied*, vol. 10, p. 024050, Aug 2018.

[82] J. Majer, J. M. Chow, J. M. Gambetta, J. Koch, B. R. Johnson, J. A. Schreier, L. Frunzio, D. I. Schuster, A. A. Houck, A. Wallraff, A. Blais, M. H. Devoret, S. M. Girvin, and R. J. Schoelkopf, "Coupling superconducting qubits via a cavity bus," *Nature*, vol. 449, pp. 443 EP –, Sep 2007.

[83] M.-A. Lemonde, S. Meesala, A. Sipahigil, M. J. A. Schuetz, M. D. Lukin, M. Loncar, and P. Rabl, "Phonon networks with silicon-vacancy centers in diamond waveguides," *Phys. Rev. Lett.*, vol. 120, p. 213603, May 2018.

[84] M. J. Burek, N. P. de Leon, B. J. Shields, B. J. M. Hausmann, Y. Chu, Q. Quan, A. S. Zibrov, H. Park, M. D. Lukin, and M. Loncar, "Free-standing mechanical and photonic nanostructures in single-crystal diamond," *Nano Letters*, vol. 12, pp. 6084–6089, Dec 2012.

[85] J. N. Becker and C. Becher, "Coherence properties and quantum control of silicon vacancy color centers in diamond (phys. status solidi a 11/2017)," *physica status solidi (a)*, vol. 214, no. 11, p. 1770170, 2017.

[86] L. Childress, J. M. Taylor, A. S. Sørensen, and M. D. Lukin, "Fault-tolerant quantum repeaters with minimal physical resources and implementations based on single-photon emitters," *Phys. Rev. A*, vol. 72, no. 5, p. 052330, 2005.

[87] D. Gottesman, T. Jennewein, and S. Croke, "Longer-baseline telescopes using quantum repeaters," *Phys. Rev. Lett.*, vol. 109, p. 070503, Aug 2012.

[88] P. Kómár, E. M. Kessler, M. Bishof, L. Jiang, A. S. Sørensen, J. Ye, and M. D. Lukin, "A quantum network of clocks," *Nature Physics*, vol. 10, pp. 582 EP –, 06 2014.

[89] C. Monroe, R. Raussendorf, A. Ruthven, K. R. Brown, P. Maunz, L.-M. Duan, and J. Kim, "Large-scale modular quantum-computer architecture with atomic memory and photonic interconnects," *Physical Review A*, vol. 89, p. 22317, feb 2014.

[90] A. Stute, B. Casabone, P. Schindler, T. Monz, P. O. Schmidt, B. Brandstätter, T. E. Northup, and R. Blatt, "Tunable ion-photon entanglement in an optical cavity," *Nature*, vol. 485, pp. 482 EP –, May 2012.

[91] A. Reiserer, N. Kalb, G. Rempe, and S. Ritter, "A quantum gate between a flying optical photon and a single trapped atom," *Nature*, vol. 508, no. 7495, pp. 237–240, 2014.

[92] S. Welte, B. Hacker, S. Daiss, S. Ritter, and G. Rempe, "Cavity carving of atomic bell states," *Phys. Rev. Lett.*, vol. 118, p. 210503, May 2017.

[93] S. Molesky, Z. Lin, A. Y. Piggott, W. Jin, J. Vuckovic, and A. W. Rodriguez, "Inverse design in nanophotonics," *Nature Photonics*, vol. 12, no. 11, pp. 659–670, 2018.

[94] S. Sun, H. Kim, G. S. Solomon, and E. Waks, "A quantum phase switch between a single solid-state spin and a photon," *Nat. Nanotechnol.*, 2016.

[95] G. Waldherr, Y. Wang, S. Zaiser, M. Jamali, T. Schulte-Herbrüggen, H. Abe, T. Ohshima, J. Isoya, J. F. Du, P. Neumann, and J. Wrachtrup, "Quantum error correction in a solid-state hybrid spin register," *Nature*, vol. 506, pp. 204 EP –, Feb 2014.

[96] W. Pfaff, B. J. Hensen, H. Bernien, S. B. van Dam, M. S. Blok, T. H. Taminiau, M. J. Tiggelman, R. N. Schouten, M. Markham, D. J. Twitchen, and R. Hanson, "Unconditional quantum teleportation between distant solid-state quantum bits," *Science*, vol. 345, no. 6196, pp. 532–535, 2014.

[97] L. Huthmacher, R. Stockill, E. Clarke, M. Hugues, C. Le Gall, and M. Atatüre, "Coherence of a dynamically decoupled quantum-dot hole spin," *Phys. Rev. B*, vol. 97, p. 241413, Jun 2018.

[98] A. Faraon, C. Santori, Z. Huang, V. M. Acosta, and R. G. Beausoleil, "Coupling of nitrogen-vacancy centers to photonic crystal cavities in monocrystalline diamond," *Phys. Rev. Lett.*, vol. 109, p. 033604, Jul 2012.

[99] M. Ruf, M. IJspeert, S. van Dam, N. de Jong, H. van den Berg, G. Evers, and R. Hanson, "Optically coherent nitrogen-vacancy centers in μm-thin etched diamond membranes," *arXiv preprint arXiv:1904.00883*, 2019.

[100] T. Müller, C. Hepp, B. Pingault, E. Neu, S. Gsell, M. Schreck, H. Sternschulte, D. Steinmüller-Nethl, C. Becher, and M. Atatüre, "Optical signatures of silicon-vacancy spins in diamond," *Nat. Comm.*, vol. 5, p. 3328, 2014.

[101] A. Sipahigil, K. D. Jahnke, L. J. Rogers, T. Teraji, J. Isoya, A. S. Zibrov, F. Jelezko, and M. D. Lukin, "Indistinguishable photons from separated silicon-vacancy centers in diamond," *Phys. Rev. Lett.*, vol. 113, p. 113602, Sep 2014.

[102] K. D. Jahnke, A. Sipahigil, J. M. Binder, M. W. Doherty, M. Metsch, L. J. Rogers, N. B. Manson, M. D. Lukin, and F. Jelezko, "Electron–phonon processes of the silicon-vacancy centre in diamond," *New J. Phys.*, vol. 17, no. 4, p. 043011, 2015.

[103] B. Pingault, D.-D. Jarausch, C. Hepp, L. Klintberg, J. N. Becker, M. Markham, C. Becher, and M. Atatüre, "Coherent control of the silicon-vacancy spin in diamond," *Nat. Commun.*, vol. 8, 2017.

[104] C. A. Ryan, J. S. Hodges, and D. G. Cory, "Robust decoupling techniques to extend quantum coherence in diamond," *Phys. Rev. Lett.*, vol. 105, p. 200402, Nov 2010.

[105] G. de Lange, Z. H. Wang, D. Ristè, V. V. Dobrovitski, and R. Hanson, "Universal dynamical decoupling of a single solid-state spin from a spin bath," *Science*, vol. 330, no. 6000, pp. 60–63, 2010.

[106] B. A. Myers, A. Das, M. C. Dartiailh, K. Ohno, D. D. Awschalom, and A. C. Bleszynski Jayich, "Probing surface noise with depth-calibrated spins in diamond," *Phys. Rev. Lett.*, vol. 113, p. 027602, Jul 2014.

[107] M. G. Dutt, L. Childress, L. Jiang, E. Togan, J. Maze, F. Jelezko, A. Zibrov, P. Hemmer, and M. Lukin, "Quantum register based on individual electronic and nuclear spin qubits in diamond," *Science*, vol. 316, no. 5829, pp. 1312–1316, 2007.

[108] T. H. Taminiau, J. Cramer, T. van der Sar, V. V. Dobrovitski, and R. Hanson, "Universal control and error correction in multi-qubit spin registers in diamond," *Nature Nanotechnology*, vol. 9, pp. 171 EP –, 02 2014.

[109] L. G. Rowan, E. L. Hahn, and W. B. Mims, "Electron-spin-echo envelope modulation," *Phys. Rev.*, vol. 137, pp. A61–A71, Jan 1965.

[110] J. Casanova, Z.-Y. Wang, J. F. Haase, and M. B. Plenio, "Robust dynamical decoupling sequences for individual-nuclear-spin addressing," *Phys. Rev. A*, vol. 92, p. 042304, Oct 2015.

[111] I. Schwartz, J. Scheuer, B. Tratzmiller, S. Müller, Q. Chen, I. Dhand, Z.-Y. Wang, C. Müller, B. Naydenov, F. Jelezko, and M. B. Plenio, "Robust optical polarization of nuclear spin baths using hamiltonian engineering of nitrogen-vacancy center quantum dynamics," *Science Advances*, vol. 4, no. 8, 2018.

[112] B. Machielse, S. Bogdanovic, S. Meesala, S. Gauthier, M. J. Burek, G. Joe, M. Chalupnik, Y.-I. Sohn, J. Holzgrafe, R. E. Evans, *et al.*, "Electromechanical control of quantum emitters in nanophotonic devices," *arXiv preprint arXiv:1901.09103*, 2019.

[113] M. H. Metsch, K. Senkalla, B. Tratzmiller, J. Scheuer, M. Kern, J. Achard, A. Tallaire, M. B. Plenio, P. Siyushev, and F. Jelezko, "Initialization and readout of nuclear spins via negatively charged silicon-vacancy center in diamond," *arXiv preprint arXiv:1902.02965*, 2019.

[114] P. Siyushev, M. H. Metsch, A. Ijaz, J. M. Binder, M. K. Bhaskar, D. D. Sukachev, A. Sipahigil, R. E. Evans, C. T. Nguyen, M. D. Lukin, P. R. Hemmer, Y. N. Palyanov, I. N. Kupriyanov, Y. M. Borzdov, L. J. Rogers, and F. Jelezko, "Optical and microwave control of germanium-vacancy center spins in diamond," *Phys. Rev. B*, vol. 96, p. 081201, Aug 2017.

[115] M. E. Trusheim, N. H. Wan, K. C. Chen, C. J. Ciccarino, J. Flick, R. Sundararaman, G. Malladi, E. Bersin, M. Walsh, B. Lienhard, *et al.*, "Lead-related quantum emitters in diamond," *Physical Review B*, vol. 99, no. 7, p. 075430, 2019.

[116] M. E. Trusheim, B. Pingault, N. H. Wan, L. De Santis, K. C. Chen, M. Walsh, J. J. Rose, J. N. Becker, E. Bersin, G. Malladi, *et al.*, "Transform-limited photons from a tin-vacancy spin in diamond," *arXiv preprint arXiv:1811.07777*, 2018.

[117] D. Buterakos, E. Barnes, and S. E. Economou, "Deterministic generation of all-photonic quantum repeaters from solid-state emitters," *Physical Review X*, vol. 7, no. 4, p. 041023, 2017.

[118] A. Stute, B. Casabone, B. Brandstätter, K. Friebe, T. E. Northup, and R. Blatt, "Quantum-state transfer from an ion to a photon," *Nature Photonics*, vol. 7, pp. 219 EP –, 02 2013.

[119] H. Kim, D. Sridharan, T. C. Shen, G. S. Solomon, and E. Waks, "Strong coupling between two quantum dots and a photonic crystal cavity using magnetic field tuning," *Opt. Express*, vol. 19, no. 3, pp. 2589–2598, 2011.

[120] A. Javadi, I. Sollner, M. Arcari, S. L. Hansen, L. Midolo, S. Mahmoodian, G. Kirsanske, T. Pregnolato, E. H. Lee, J. D. Song, S. Stobbe, and P. Lodahl, "Single-photon non-linear optics with a quantum dot in a waveguide," *Nat. Commun.*, vol. 6, p. 8655, Oct 2015.

[121] J. N. Becker, J. Görlitz, C. Arend, M. Markham, and C. Becher, "Ultrafast all-optical coherent control of single silicon vacancy colour centres in diamond," *Nat. Commun.*, vol. 7, p. 13512, 2016.

[122] J. N. Becker, B. Pingault, D. Groß, M. Gündoğan, N. Kukharchyk, M. Markham, A. Edmonds, M. Atatüre, P. Bushev, and C. Becher, "All-optical control of the silicon-vacancy spin in diamond at millikelvin temperatures," *Phys. Rev. Lett.*, vol. 120, p. 053603, Jan 2018.

[123] E. G. Bauer, B. W. Dodson, D. J. Ehrlich, L. C. Feldman, C. P. Flynn, M. W. Geis, J. P. Harbison, R. J. Matyi, P. S. Peercy, P. M. Petroff, and et al., "Fundamental issues in heteroepitaxy—a department of energy, council on materials science panel report," *Journal of Materials Research*, vol. 5, no. 4, p. 852–894, 1990.

[124] S. Mouradian, N. H. Wan, T. Schröder, and D. Englund, "Rectangular photonic crystal nanobeam cavities in bulk diamond," *Applied Physics Letters*, vol. 111, no. 2, p. 021103, 2017.

[125] C. D. Clark, H. Kanda, I. Kiflawi, and G. Sittas, "Silicon defects in diamond," *Phys. Rev. B*, vol. 51, pp. 16681–16688, Jun 1995.

[126] T. Staudacher, F. Ziem, L. Häussler, R. Stöhr, S. Steinert, F. Reinhard, J. Scharpf, A. Denisenko, and J. Wrachtrup, "Enhancing the spin properties of shallow implanted nitrogen vacancy centers in diamond by epitaxial overgrowth," *Applied Physics Letters*, vol. 101, no. 21, p. 212401, 2012.

[127] M. W. Doherty, N. B. Manson, P. Delaney, and L. C. L. Hollenberg, "The negatively charged nitrogen-vacancy centre in diamond: the electronic solution," *New J. Phys.*, vol. 13, no. 2, p. 025019, 2011.

[128] J. M. Moison, F. Houzay, F. Barthe, L. Leprince, E. André, and O. Vatel, "Self-organized growth of regular nanometer-scale inas dots on gaas," *Applied Physics Letters*, vol. 64, no. 2, pp. 196–198, 1994.

[129] L. J. Rogers, K. D. Jahnke, M. H. Metsch, A. Sipahigil, J. M. Binder, T. Teraji, H. Sumiya, J. Isoya, M. D. Lukin, P. Hemmer, *et al.*, "All-optical initialization, readout, and coherent preparation of single silicon-vacancy spins in diamond," *Phys. Rev. Lett.*, vol. 113, no. 26, p. 263602, 2014.

[130] L. J. Rogers, K. D. Jahnke, T. Teraji, L. Marseglia, C. Müller, B. Naydenov, H. Schauffert, C. Kranz, J. Isoya, L. P. McGuinness, and F. Jelezko, "Multiple intrinsically identical single-photon emitters in the solid state," *Nat. Commun.*, vol. 5, p. 4739, Aug. 2014.

[131] D. Riedel, I. Söllner, B. J. Shields, S. Starosielec, P. Appel, E. Neu, P. Maletinsky, and R. J. Warburton, "Deterministic enhancement of coherent photon generation from a nitrogen-vacancy center in ultrapure diamond," *Phys. Rev. X*, vol. 7, p. 031040, Sep 2017.

[132] S. Meiboom and D. Gill, "Modified spin-echo method for measuring nuclear relaxation times," *Review of Scientific Instruments*, vol. 29, no. 8, pp. 688–691, 1958.

[133] T. Gullion, D. Baker, and M. Conradi, "New, compensated carr-purcell sequences," *Journal of Magnetic Resonance (1969)*, vol. 89, no. 3, pp. 479–484, 1990.

[134] A. D. Milov, A. B. Ponomarev, and Y. D. Tsvetkov, "Electron-electron double resonance in electron spin echo: Model biradical systems and the sensitized photolysis of decalin," *Chemical Physics Letters*, vol. 110, no. 1, pp. 67–72, 1984.

[135] G. de Lange, Z. H. Wang, D. Ristè, V. V. Dobrovitski, and R. Hanson, "Universal dynamical decoupling of a single solid-state spin from a spin bath," *Science*, vol. 330, no. 6000, pp. 60–63, 2010.

[136] R. Kalish and S. Prawer, "Graphitization of diamond by ion impact: Fundamentals and applications," *Nuclear Instruments and Methods in Physics Research Section B: Beam Interactions with Materials and Atoms*, vol. 106, no. 1, pp. 492 – 499, 1995. Ion Beam Modification of Materials.

[137] V. M. Acosta, E. Bauch, M. P. Ledbetter, C. Santori, K.-M. C. Fu, P. E. Barclay, R. G. Beausoleil, H. Linget, J. F. Roch, F. Treussart, S. Chemerisov, W. Gawlik, and D. Budker, "Diamonds with a high density of nitrogen-vacancy centers for magnetometry applications," *Phys. Rev. B*, vol. 80, p. 115202, Sep 2009.

[138] L.-M. Duan and H. J. Kimble, "Scalable Photonic Quantum Computation through Cavity-Assisted Interactions," *Physical Review Letters*, vol. 92, p. 127902, mar 2004.

[139] T. Tiecke, J. D. Thompson, N. P. de Leon, L. Liu, V. Vuletić, and M. D. Lukin, "Nanophotonic quantum phase switch with a single atom," *Nature*, vol. 508, no. 7495, pp. 241–244, 2014.

[140] X. Rong, J. Geng, F. Shi, Y. Liu, K. Xu, W. Ma, F. Kong, Z. Jiang, Y. Wu, and J. Du, "Experimental fault-tolerant universal quantum gates with solid-state spins under ambient conditions," *Nature Communications*, vol. 6, pp. 8748 EP –, Nov 2015. Article.

[141] C. P. Slichter, *Principles of Magnetic Resonance*. No. 1 in Solid State Sciences, Springer-Verlag Berlin Heidelberg, 1990.

[142] A. V. Kuhlmann, J. H. Prechtel, J. Houel, A. Ludwig, D. Reuter, A. D. Wieck, and R. J. Warburton, "Transform-limited single photons from a single quantum dot," *Nature Communications*, vol. 6, pp. 8204 EP –, Sep 2015. Article.

[143] C. Neill, A. Megrant, R. Barends, Y. Chen, B. Chiaro, J. Kelly, J. Y. Mutus, P. J. J. O'Malley, D. Sank, J. Wenner, T. C. White, Y. Yin, A. N. Cleland, and J. M. Martinis, "Fluctuations from edge defects in superconducting resonators," *Applied Physics Letters*, vol. 103, no. 7, p. 072601, 2013.

[144] C. W. Chou, H. de Riedmatten, D. Felinto, S. V. Polyakov, S. J. van Enk, and H. J. Kimble, "Measurement-induced entanglement for excitation stored in remote atomic ensembles," *Nature*, vol. 438, no. 7069, pp. 828–832, 2005.

[145] W. K. Wootters, "Entanglement of formation of an arbitrary state of two qubits," *Phys. Rev. Lett.*, vol. 80, pp. 2245–2248, Mar 1998.

[146] H.-K. Lo, M. Curty, and B. Qi, "Measurement-Device-Independent Quantum Key Distribution," *Physical Review Letters*, vol. 108, p. 130503, mar 2012.

[147] S. L. Braunstein and S. Pirandola, "Side-Channel-Free Quantum Key Distribution," *Physical Review Letters*, vol. 108, p. 130502, mar 2012.

[148] S. Pirandola, R. Laurenza, C. Ottaviani, and L. Banchi, "Fundamental limits of repeaterless quantum communications," *Nature Communications*, vol. 8, p. 15043, apr 2017.

[149] N. Gisin, G. Ribordy, W. Tittel, and H. Zbinden, "Quantum cryptography," *Reviews of Modern Physics*, vol. 74, pp. 145–195, mar 2002.

[150] M. Minder, M. Pittaluga, G. L. Roberts, M. Lucamarini, J. F. Dynes, Z. L. Yuan, and A. J. Shields, "Experimental quantum key distribution beyond the repeaterless secret key capacity," *Nature Photonics*, vol. 13, no. 5, pp. 334–338, 2019.

[151] C. Panayi, M. Razavi, X. Ma, and N. Lütkenhaus, "Memory-assisted measurement-device-independent quantum key distribution," *New Journal of Physics*, vol. 16, no. 4, p. 43005, 2014.

[152] H.-K. Lo, X. Ma, and K. Chen, "Decoy State Quantum Key Distribution," *Physical Review Letters*, vol. 94, p. 230504, jun 2005.

[153] H.-K. Lo, H. F. Chau, and M. Ardehali, "Efficient Quantum Key Distribution Scheme and a Proof of Its Unconditional Security," *Journal of Cryptology*, vol. 18, no. 2, pp. 133–165, 2005.

[154] M. Curty, F. Xu, W. Cui, C. C. W. Lim, K. Tamaki, and H.-K. Lo, "Finite-key analysis for measurement-device-independent quantum key distribution," *Nature Communications*, vol. 5, p. 3732, apr 2014.

[155] E. Biham, B. Huttner, and T. Mor, "Quantum cryptographic network based on quantum memories," *Physical Review A*, vol. 54, pp. 2651–2658, oct 1996.

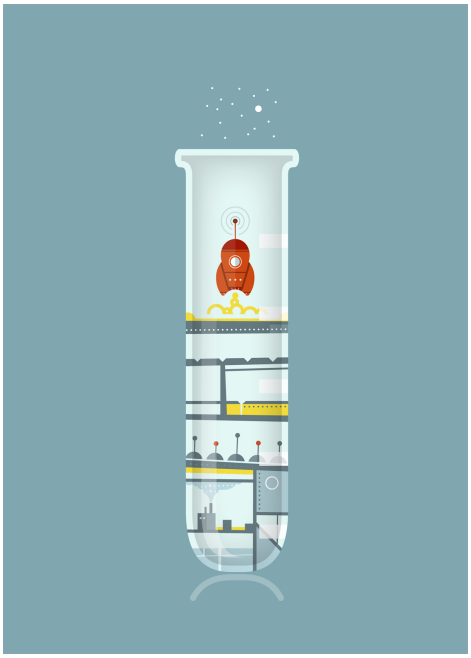
[156] R. Raussendorf and H. J. Briegel, "A One-Way Quantum Computer," *Physical Review Letters*, vol. 86, pp. 5188–5191, may 2001.

[157] J. Borregaard, H. Pichler, T. Schöder, M. D. Lukin, P. Lodahl, and A. S. Sørensen, "One-way quantum repeater based on near-deterministic photon-emitter interfaces," pp. 1–19, 2019.

[158] E. Khabiboulline, J. Borregaard, K. De Greve, and M. Lukin, "Optical Interferometry with Quantum Networks," *Physical Review Letters*, vol. 123, p. 70504, aug 2019.

[159] H. de Riedmatten, I. Marcikic, V. Scarani, W. Tittel, H. Zbinden, and N. Gisin, "Tailoring photonic entanglement in high-dimensional Hilbert spaces," *Physical Review A*, vol. 69, p. 50304, may 2004.

[160] T. Sasaki, Y. Yamamoto, and M. Koashi, "Practical quantum key distribution protocol without monitoring signal disturbance," *Nature*, vol. 509, p. 475, may 2014.



This thesis was typeset using LaTeX, originally developed by Leslie Lamport and based on Donald Knuth's TeX. The body text is set in 11 point Egenolff-Berner Garamond, a revival of Claude Garamont's humanist typeface. The above illustration, *Science Experiment 02*, was created by Ben Schlitter and released under CC BY-NC-ND 3.0. A template that can be used to format a PhD dissertation with this look & feel has been released under the permissive AGPL license, and can be found online at github.com/suchow/Dissertate or from its lead author, Jordan Suchow, at suchow@post.harvard.edu.